
ETD Archive

Summer 1-1-2021

Energy-oriented Modeling And Control of Robotic Systems

Amin Ghorbanpour
Cleveland State University

Follow this and additional works at: <https://engagedscholarship.csuohio.edu/etdarchive>

How does access to this work benefit you? Let us know!

Recommended Citation

Ghorbanpour, Amin, "Energy-oriented Modeling And Control of Robotic Systems" (2021). *ETD Archive*. 1293.

<https://engagedscholarship.csuohio.edu/etdarchive/1293>

This Dissertation is brought to you for free and open access by EngagedScholarship@CSU. It has been accepted for inclusion in ETD Archive by an authorized administrator of EngagedScholarship@CSU. For more information, please contact library.es@csuohio.edu.

ENERGY-ORIENTED MODELING AND CONTROL OF
ROBOTIC SYSTEMS

AMIN GHORBANPOUR

Master of Science in Aerospace Engineering

Tarbiat Modares University

August 2011

Bachelor of Science in Aerospace Engineering

Amirkabir University of Technology

August 2008

submitted in partial fulfillment of requirements for the degree
DOCTOR OF PHILOSOPHY IN MECHANICAL ENGINEERING

at the

CLEVELAND STATE UNIVERSITY

AUGUST 2021

We hereby approve this dissertation for

AMIN GHORBANPOUR

Candidate for the Doctor of Philosophy in Mechanical Engineering degree for the

Department of Mechanical Engineering and

CLEVELAND STATE UNIVERSITY'S

College of Graduate Studies by

Hanz Richter, Ph.D, Dissertation Committee Chairperson
Department of Mechanical Engineering

Eric Schearer, Ph.D, Dissertation Committee Member
Department of Mechanical Engineering

Dan Simon, Ph.D, Dissertation Committee Member
Department of Electrical Engineering and Computer Science

Zhiqiang Gao, Ph.D, Dissertation Committee Member
Department of Electrical Engineering and Computer Science

L. Felipe Martins, Ph.D, Dissertation Committee Member
Department of Mathematics and Statistics

Date of Defense: August 5, 2021

This student has fulfilled all requirements for the
Doctor of Philosophy in Engineering degree.

Chandra Kothapalli, Ph.D, Doctoral Program Director

ACKNOWLEDGMENTS

This dissertation is the result of four years of my academic life at Cleveland State University. There are countless failures behind the outcome of my dissertation. Nevertheless, I never stopped trying to discover what I was looking for! At CSU, I have gained enormous valuable insight into how a research effort is structured. I have met many people, great people, who taught me things for which I will be thankful for the rest of my life. My journey has not finished, and this is only the beginning. The journey will move on to another phase, same path, same goal! I would like to thank some who helped me become the person who I could be proud of:

First and foremost, I am deeply grateful to my advisor Prof. Hanz Richter for all his help and advice during the course of my Ph.D. degree. Dr. Richter! your valuable guidance throughout my studies, brought my work to a higher level. I learned how to conduct research from you. Thank you for supporting my study.

My gratitude extends to the National Science Foundation for supporting this project through grant No. 1536035. Additionally, I would like to thank my committee: Prof. Dan Simon, Dr. Eric M. Schearer, Dr. Zhiqiang Gao, and Dr. Luiz F. Martins. Thank you all for your insightful feedback. I would also like to acknowledge my colleagues and friends who made my studies a memorable experience of my life. Poya, Humberto, Eri, and Holly. Great people and fantastic researchers. Wish you all the best in your future endeavors.

I would like to offer my special thanks to my parents and brothers. It was hard not being with you for the last four years. Yet, you all supported me emotionally, and that means a lot to me.

In the end, I like to thank my wife Leila. Everything I achieved was because of you.

You are my love of life. Thank you for believing in me. The last not the least, a special thanks to the little man!

Imagination is more important than knowledge. For knowledge is limited to all we know and understand, while imagination embraces the entire world, and all there ever will be to know and understand.

Albert Einstein

AMIN GHORBANPOUR

ABSTRACT

This research focuses on the energy-oriented control of robotic systems using an ultra-capacitor as the energy source. The primary objective is to simultaneously achieve the motion task objective and to increase energy efficiency through energy regeneration. To achieve this objective, three aims have been introduced and studied: brushless DC motors (BLDC) control by achieving optimum current in the motor, such that the motion task is achieved, and the energy consumption is minimized. A proof-of-concept study to design a BLDC motor driver which has superiority compare to an off-the-shelf driver in terms of energy regeneration, and finally, the third aim is to develop a framework to study energy-oriented control in cooperative robots.

The first aim is achieved by introducing an analytical solution which finds the optimal currents based on the desired torque generated by a virtual. Furthermore, it is shown that the well-known choice of a zero direct current component in the direct-quadrature frame is sub-optimal relative to our energy optimization objective.

The second aim is achieved by introducing a novel BLDC motor driver, composed of three independent regenerative drives. To run the motor, the control law is obtained by specifying an outer-loop torque controller followed by minimization of power consumption via online constrained quadratic optimization. An experiment is conducted to assess the performance of the proposed concept against an off-the-shelf driver. It is shown that, in terms of energy regeneration and consumption, the developed driver has better performance, and a reduction of 15% energy consumption is achieved.

For the third aim, an impedance-based control scheme is introduced for cooperative manipulators grasping a rigid object. The position and orientation of the payload are to be maintained close to a desired trajectory, trading off tracking accuracy by low energy consumption and maintaining stability. To this end, an optimization problem is formulated using energy balance equations. The optimization finds the damping and stiffness gains of the impedance relation such that the energy consumption is minimized. Furthermore, \mathcal{L}_2 stability techniques are used to allow for time-varying damping and stiffness in the desired impedance. A numerical example is provided to demonstrate the results.

TABLE OF CONTENTS

	Page
ABSTRACT	v
LIST OF TABLES	x
LIST OF FIGURES	xi
CHAPTER	
I BACKGROUND AND MOTIVATION	1
1.1 Introduction	1
1.1.1 Robotics Systems Actuated by BLDC Motor	5
1.1.2 Cooperative Robot Manipulators	6
1.2 Review of Literature	7
1.2.1 A Review of The Literature Related to BLDC Motor Modeling and Control	7
1.2.2 A Review of The Literature Related to CRM Modeling and Control	8
1.3 Problem Statement	14
1.4 Specific Aims	15
1.5 Outline	16
II ENERGY-ORIENTED MODELING AND CONTROL OF ROBOTS WITH BRUSHLESS DC MOTORS	18
2.1 Introduction	18
2.2 Manipulator Dynamics Model	20
2.3 Control Strategy Based on Actuator Current Regulation	21
2.3.1 BLDC Motor Morphology	21
2.3.2 BLDC Motor Modeling	22

2.3.3	Augmented Dynamics Model of Robot and JMs	26
2.3.4	Control Scheme	26
2.3.5	Energy Balance	29
2.3.6	Energy Optimization	32
2.3.7	Preliminary Simulation Results	38
2.3.8	Concluding Remarks	41
2.4	Control Strategy Based on Actuator Voltage Regulation	42
2.4.1	BLDC Motor Modeling	43
2.4.2	Semi-active Virtual Control Strategy	46
2.4.3	Internal and External Energy Balance	48
2.4.4	Optimization Problem	49
2.4.5	Experimental Setup	51
2.4.6	Concluding remarks	66
III	ENERGY-ORIENTED MODELING AND CONTROL OF COOPERA-	
	TIVE ROBOT MANIPULATORS	70
3.1	Introduction	70
3.2	Notation and Mathematical Preliminaries	71
3.2.1	Passivity in Feedback Systems	73
3.3	Cooperative Robot Manipulators Modeling	76
3.3.1	Comprehensive Dynamics of Cooperative Robots	76
3.3.2	Dynamics of the Payload	81
3.3.3	Coupling in Cooperative Robots	82
3.4	Control Implementation and Energy Balances	84
3.4.1	Semi-active Virtual Control Strategy	84
3.4.2	Internal and External Energy Balance	85
3.5	Control Scheme	89
3.6	Impedance Control	91

3.6.1	Impedance Control as Virtual Controller	92
3.7	Optimization problem	99
3.8	Variable Impedance Control	100
3.9	Simulation	104
3.10	Concluding Remarks	110
IV	CONCLUSION	112
4.1	Statement of Contributions	112
4.2	Future Perspectives	117
	BIBLIOGRAPHY	121
	APPENDICES	139
A	OUTLINE OF SPACE VECTOR PULSE WIDTH MODULATION	
B	EXTERNAL ENERGY BALANCE IN ROBOT ACTUATED BY BRUSHLESS DC MOTORS	
C	EXTERNAL ENERGY BALANCE IN COOPERATIVE ROBOT MANIPULATORS	

LIST OF TABLES

Table		Page
I	Planar Two-link Robot and BLDC Motor Parameters	39
II	Optimal and Sub-optimal Energy Comparison (Joule)	40
III	Pendulum and BLDC motor parameters (Experimental setup I). . . .	53
IV	Pendulum and BLDC motor parameters (Experimental setup II). . . .	60
V	Tracking accuracy and energy consumption comparison.	63
VI	The parameters for two identical robots and the object (rod).	104
VII	Parameters of genetic algorithm.	105
VIII	Switching States	140

LIST OF FIGURES

Figure	Page
1	Ragone plot with three energy storage devices placed at relative locations [1].
	2
2	Maxwell ultracapacitor (165 farad-48 volt). Control, Robotics and Mechatronics Laboratory (CRML), Cleveland State University.
	3
3	SyRen regenerative drive (25 Amp). CRML, Cleveland State University.
	3
4	Illustration of four-quadrant motor operation. Image credit: Quantum Controls.
	4
5	Structure of BLDC motor. The picture is adopted from https://www.nidec.com/en/technology/capability/brushless
	23
6	(a) Cross section view of a three phase BLDC motor with PM rotor and three windings. (b) The $a-b-c$, $d-q$, and $\alpha - \beta$ reference frames.
	23
7	Power supply, inverter, and equivalent circuit model of the motor of the j th JM. The subscript j is dropped in the plot.
	24
8	Current regulation Control scheme of augmented model of robot considering BLDC motor dynamics.
	30
9	Graphic Demonstration of Solution for Eqn. (2.20a).
	35
10	Graphic Demonstration of Solution for Eqn. (2.20b).
	36
11	joints' angles tracking desired trajectory.
	40
12	joints' angular velocities tracking desired velocity.
	40
13	Desired currents on dq axis ($L_q > L_d$).
	40
14	Difference between desired and actual currents.
	40
15	Optimal solutions of currents.
	41

16	Ultracapacitor charge.	41
17	Illustration of semi-active joints connection to a single energy storage element.	43
18	Flux density configuration. (a) Sinusoidal pattern flux between stator and rotor. (b) Trapezoidal pattern flux between stator and rotor. . . .	44
19	Schematic of the connection setup of j th BLDC motor, the RCU, and the ESE.	45
20	The structure of online control algorithm. $X = [q^T, \dot{q}^T]^T$ and $X^d = [(q^d)^T, (\dot{q}^d)^T]^T$ are the vectors of the actual and desired states, respectively.	50
21	Dimension Engineering SyRen 25A 6V-24V Regenerative Motor Driver.	52
22	Maxwell Technologies, Ultracapacitor Module.	52
23	dSPACE MicroLabBox.	52
24	Laboratory experimental setup I. (1) Data monitoring, (2) MicroLabBox controller, (3) Ultracapacitor, (4) BLDC motor, (5) Optical encoder, (6) Pendulum, (7) Three motor drivers, (8) Three current sensors	54
25	Pendulum angle and angular velocity, tracking desired trajectory ($q_{des} = 3 \sin(2t)$).	57
26	Applied voltage to each phase of the motor.	57
27	Power flows for each phase of the motor.	58
28	(a) sum of powers in three phases. (b) voltage of ultracapacitor. (c) pendulum angle. The red lines in (a-b) show the fitted polynomial curve to the net power and the voltage. The black line in (a) shows the zero level.	58
29	Ultracapacitor voltage. The peaks indicate the times when regeneration happens.	59

30	Sankey diagram showing the energy balance for the pendulum when following the desired trajectory. (a) The energy balance during non-regenerative (NR) phase. (b) The energy balance during regenerative (R) phase.	59
31	Schematic of laboratory setup. (a) The developed motor driver, (b) The standard off-the-shelf driver. Wires that transfer charge are shown with solid line and wires which transfer data are shown with dotted line. 1: Mass at the tip, 2: The pendulum, 3: The Anaheim BLDC motor and gearbox, 4(a): Optical encoder, 4(b): The hall-effect sensor, 5(a): SyRen motor drives, 5(b): Brushless PWM servo amplifier 6: ACS712 current sensor, 7: The Maxwell ultracapacitor, 8: The MicroLabBox, 9: The computer	61
32	Laboratory experimental setup (1) Pendulum, (2) BLDC motor, gearbox, and optical/hall sensors, (3) MicroLabBox controller, (4) RCUa, (5) ultracapacitor, (6) Current sensor, (7) Data monitoring.	62
33	Pendulum angle time history, tracking desired trajectory of $q_{ref} = 3 \sin(2t)$. For clarity, the figure is depicted for a small-time period.	64
34	The generated virtual control (a) RCUa, (b) RCUb.	65
35	Time history of ultracapacitor voltage. (a) Voltage change for RCUa, (b) Voltage change for RCUb. In both plots, a linear curve is fitted to the data.	65
36	RCUa - (a) Net power in ultracapacitor terminal. (b) voltage of ultracapacitor. (c) pendulum angle. The red lines in (a-b) show the fitted polynomial curve.	66
37	RCUb - (a) Net power in ultracapacitor terminal. (b) voltage of ultracapacitor. (c) pendulum angle. The red lines in (a-b) show the fitted polynomial curve.	67

38	Sankey diagram showing the energy balance for the pendulum when following the desired trajectory. (a) The energy balance during non-regenerative phase. (b) The energy balance during regenerative phase. .	67
39	Feedback interconnection with two external inputs.	74
40	Illustration of N robots grasping an object. The coordinate frames attached to the end-effector, robots' base, load's center of mass, and arbitrary world frame are, respectively, Σ_{ei} , Σ_i , Σ_O , Σ_W	77
41	Illustration of semi-active joints connection to a single power source. . .	80
42	Semi-active joint setup and its connection to motor driver and ultracapacitor.	80
43	Control scheme to control CRM in joint space, using impedance relation and SVC.	89
44	(a) Feedback interconnection with one external input. (b) Transformation of interconnection to two external inputs.	97
45	Setup for two identical cooperative robots carrying a load. The world frame is attached to the base of the left robot. The distance between robots is $d_0 = 0.8 \text{ m}$ and robots are placed on the same level. $(\cdot)_{ij}$ represents any parameter for the j th joint of i th robot.	104
46	The actual and desired joint angles for Robot #1.	107
47	The actual and desired joint angles for Robot #2.	108
48	Movement in 2D. Frames are captured in each 0.05 s.	108
49	Virtual torques applied to the robots.	109
50	Power in each joint.	109
51	Sankey diagram showing the energy balance for the CRM when following the desired trajectory.	110
52	Voltage space vector locations corresponding to different switching states.	141

53	Diagram of switching pattern for SVPWM [2].	141
----	---	-----

CHAPTER I

BACKGROUND AND MOTIVATION

1.1 Introduction

Saving energy has become a major driving force in engineering, owing to the increasing demand for cost-efficient and long-life systems, and as a result, engineers sought to find solutions for optimal energy consumption. This is particularly important in robotics due to the increased reliance in industrial automation.

In robots with on-board, finite energy storage element, reducing the amount of energy needed to complete a task leads to smaller operating costs and longer operating times. These robotics systems are prevalent in electric vehicles, powered human assistive devices, aerospace vehicles, etc. [3, 4, 5, 6, 7, 8, 9, 10, 11, 12, 13]. Therefore, in such robotics systems, Energy Storage Element (ESE) plays an utmost important role in the energy consumption, which makes the energy storage technologies and their emerging applications as one of the main themes in the energy efficiency of the robotics systems.

Since energy comes in various forms including electrical, mechanical, thermal, etc., the ESE essentially stores that energy for use on demand. Major storage solutions, suitable for robotics application, include ultracapacitors, batteries, and fuel

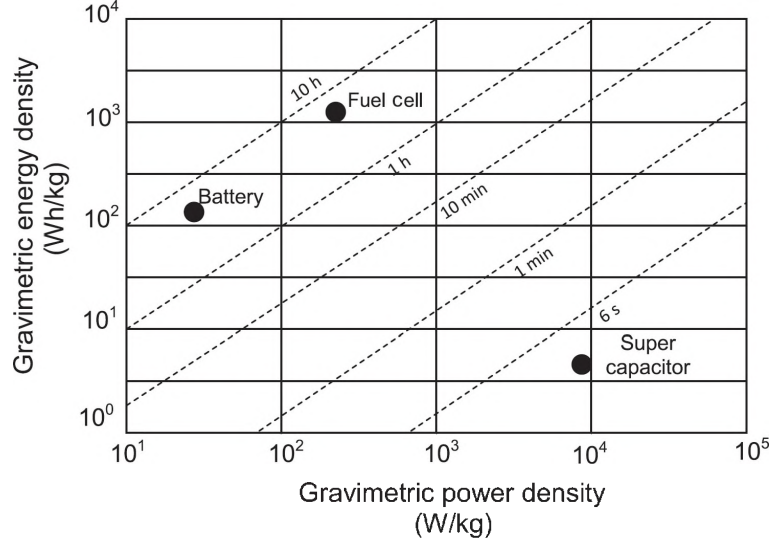


Figure 1: Ragone plot with three energy storage devices placed at relative locations [1].

cells. These energy devices can be compared together in a Ragone plot, with respect to the specific energy and the specific power, as shown in Fig. 1. In the Ragone plot, the vertical axis describes how much energy is available per unit mass (energy density), while the horizontal axis shows how quickly the energy can be delivered (power density). According to the Ragone plot, the highest energy density belongs to fuel cell, battery, and ultracapacitor, respectively. The highest power density belongs to ultracapacitors, fuel cells, and batteries, respectively. In most robotics applications, the power density is more important than energy density.

Because ultracapacitors have the highest power density, they have received widespread attention [3, 4, 14]. An example of an ultracapacitor is shown in Fig. 2. In addition to being lightweight and durable, an ultracapacitor can be both discharged and charged at high rates due to the high power density. The high discharge rate provides high power, and high charge rate leads to an essential feature for energy saving through energy regeneration. We define energy regeneration as the process of transferring energy back to a power source during normal operation [4]. Energy



Figure 2: Maxwell ultracapacitor (165 farad-48 volt). Control, Robotics and Mechatronics Laboratory (CRML), Cleveland State University.

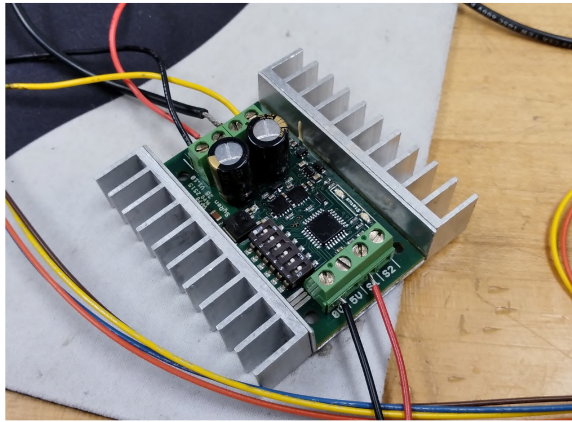


Figure 3: SyRen regenerative drive (25 Amp). CRML, Cleveland State University.

regeneration is a unique technique to harvest excessive energy in the robotics system which would have been wasted if the ESE could not admit it.

Furthermore, energy regeneration is possible when recovering energy and feeding it back into the ESE has been guaranteed in the dynamical system. Regenerative drives provide the opportunity of energy regeneration, and they facilitate transferring energy to the ESE. Generally, in a robotics system, the actuator converts electrical energy into mechanical energy. However, when the actuator acts like a generator and converts mechanical energy into electrical energy, the regenerative drive is capable of capturing the produced electric energy from the generator (actuator) and transfer it to the ESE. An example of a regenerative drive is shown in Fig. 3.

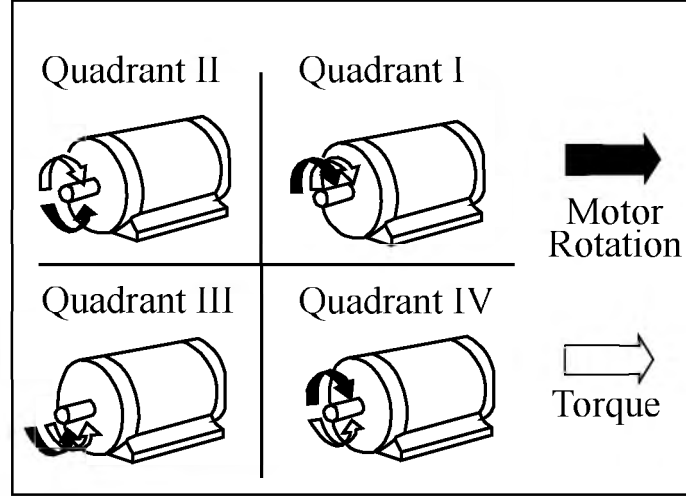


Figure 4: Illustration of four-quadrant motor operation. Image credit: Quantum Controls.

Using regenerative drive, the actuator can produce positive or negative torque, in either forward or reverse rotation. This is referred to as “four-quadrant” operation as shown in Fig. 4. Note that when the arrows have the same direction, the motor is pulling, and when the arrows have opposite direction, the motor is braking (holding). Regeneration occurs in quadrants II and IV, where the direction of the torque opposes the direction of motor rotation. When the actuator operates in these quadrants, regenerative drive allows the electrical energy to go from the actuator to the ESE.

Accordingly, the two key components for saving energy are the capability of ESE to be charged fast and the existence of regenerative drive in the system. In this regard, numerous studies have been conducted to assess the energy regeneration in dynamical systems. In robotics systems, most of the previous researches have studied energy regeneration of a sole robot actuated by DC motors [4, 13, 6, 5, 12, 15, 16, 17]. The promising results of those studies, opened new horizons towards exploring the potential of energy regeneration in two unique but not entirely independent problems; The energy-oriented control of various actuators and studying energy regeneration in

multiple cooperative robots.

This research is motivated by the application of regenerative technologies in robotics systems when a significant potential for energy recovery exists. To this end, the main focus of this dissertation is studying energy regeneration in i) robotics systems actuated by brushless DC (BLDC) motor, and, ii) cooperative robot manipulators. Note that designing the controller to execute a motion task and simultaneously aiming for maximum energy regeneration is the primary objective of this study.

1.1.1 Robotics Systems Actuated by BLDC Motor

Actuator efficiency is one of the main determinants of the overall energy consumption for a given motion task, since most of the losses are attributed to these elements. In the field of robotics, DC motor is one of the most common actuators. Previous studies have mostly focused on energy regeneration for electromechanical systems with DC motor actuators [18, 19, 20]. However, the general trend is moving toward using BLDC motors, which can be operated more efficiently than DC motors [2, 21]. BLDC motors are typically 85-90% efficient, whereas brushed DC motors are around 75-80% efficient. Here, efficiency means the ratio of mechanical power output to electric power input in the motor. Furthermore, BLDC motors are highly reliable due to the lack of brushes, and they have less friction in comparison to DC motors [21]. Nevertheless, for robotics applications, they had been studied less in terms of energy saving [5, 22]. The structure and application of BLDC in robotics and more general machinery have been well documented [21, 2, 23, 24].

A study of robotics systems with particular consideration of the dynamics of the BLDC actuators is required to adequately consider energy-optimal control problems. Therefore, the first part of this research is dedicated to investigate the energy regeneration and control of BLDC actuators in robotics manipulators. Due

to the aforementioned benefits of BLDC motor in comparison to DC motor, we set the first goal of our research as exploring the opportunities for energy regeneration in BLDC motors.

1.1.2 Cooperative Robot Manipulators

Studies related to energy-oriented control of robotics manipulators are mostly done for single robots [4, 13, 6, 5, 12, 15, 16, 17]. These works can be extended to investigate energy regeneration when multiple robots are working together, executing a motion task. Here, multiple robots performing a task together, in a cooperative manner, are called Cooperative Robot Manipulators (CRM). Cooperative manipulation of a common object offers significant advantages over a single manipulator when performing a task which is difficult or impossible for the single manipulator. CRM show versatility in many tasks, and they may reduce the task's cost. Several studies have been conducted toward addressing control issues in CRM, e.g., see [25, 26, 27, 28, 29]. Nevertheless, discussion over energy reduction in CRM has received less attention [30, 31].

The second part of this research is dedicated to investigate the energy regeneration and control of CRM. Because of the positive results obtained for energy regeneration in single robots, therefore, we set the second goal of our research, exploring energy regeneration in the CRM. Indeed, cooperative robots are dynamical systems with high inertia which move fast, and they are in contact with external forces/moments. All these elements are signs of significant potential for energy recovery. So, the main hypothesis of this part is the assumption that considerable potential for energy recovery exists in the CRM.

1.2 Review of Literature

The following literature survey provides a brief overview of information and research relevant to the primary objectives of our research. The literatures are divided into two parts. In the first part, researches that aim for energy-oriented control of BLDC are explored, and, in the second part, researches related to CRM dynamics modeling and control is explained. Note that the energy-oriented research on CRM is scant and, to the best knowledge of the author, our work is the first attempt to optimize energy regeneration in CRM.

1.2.1 A Review of The Literature Related to BLDC Motor Modeling and Control

Brushless DC electric motor (BLDC), also known as the electronically commutated motor, is designed to run on an alternating current (AC) voltage. It consists of a permanent magnet rotor and three stator windings, which in conjunction with a DC power supply and an inverter create a rotating motor. The inverter (motor drive) creates the AC voltage, such that the applied voltage to each winding of the motor is adjusted according to the desired value. For a detailed description of BLDC operation, refer to Section 2.3.1.

The most common actuators in the field of robotics are brushed DC and BLDC motors. It has been shown that both types of motors can be used for forward motoring and reverse regeneration mode [4, 3, 32, 33]. In terms of maintenance costs, efficiency, durability, and thermal characteristics, the BLDC motor has advantages over DC motor [2, 21]. Previous studies have mostly focused on energy regeneration of electromechanical systems with DC motor actuators [4, 19, 20, 34]. Energy-oriented studies of BLDC motors are mostly focused on energy regeneration in the braking systems, and they limit the energy efficiency due to the rectangular stator current

modeling for detecting the commutation moments in their driver [32, 33, 35, 36, 37, 38, 39]. Other research areas where energy regeneration is explored are including prostheses leg [40], and airplane propulsion [41, 42, 43].

Moreover, many researchers have studied the dynamics and control of BLDC motors without considering the coupled dynamics of the driven robot [21, 2, 23, 44, 45, 46, 24]. Simultaneous consideration of coupled manipulator-BLDC dynamics and energy regeneration has been considered in a few recent works [14, 5, 47]. Well-known control schemes for BLDC motors include the pulse-width modulation (PWM) technique to convert the power supply input DC voltage into a modulated driving voltage [5, 48]. As a consequence of using switching to create a voltage command, each phase of the motor receives a level of voltage selected from a finite set, based on the binary states of the switches. For instance, in a three-phase driver, only eight levels of power source voltage can be applied to each phase. This limits the ability to optimize energy consumption while simultaneously meeting motion control objectives. Moreover, control methods traditionally developed for BLDC motors consider the motor and the driver as a single subsystem, which eventually uses the PWM technique [38, 32, 35].

1.2.2 A Review of The Literature Related to CRM Modeling and Control

Robots offer superior capabilities than humans for carrying out motion tasks involving large loads, high speeds, and tight precision requirements. However, some tasks are difficult or impossible for a single robot. The limits in the structure of a robot prevent a sole robot to operate with large, unbalanced, or flexible loads. Cooperative robot manipulators (CRM) offer significant advantages over a single robot, and they show better performance in tasks such as grasping, gripping, lifting, transferring, lowering, and approaching an object. Regardless of the benefits obtained by employing CRM, it comes at the cost of complexity for mathematical modeling, control, and coordination.

Here, the term cooperative means the collaboration of multi robots in handling a payload.

The characteristic of successful cooperation is tracking the desired motion of an object while applying a desired force by means of the robots' end-effectors to the object. To devise a control solution for CRM, some difficulties need to be addressed, which of the most important problem is the build-up closed kinematic chain mechanism caused by grasping the object using the end-effectors of robots. Generally, to deal with the drawbacks, two different cooperation strategies can be defined: loose and tight cooperative control [26]. A loose cooperative task is performed when robots play complementary roles during task execution. One robot operates in standard mode and others operate in open mode. That is a way to achieve a programmable compliance via force and torques feedbacks. Tight cooperative behavior is achieved if the motion of the object is related to the motion of all robots.

Hence, the most important challenges in studying CRM are kinematics and dynamics modeling of CRM and implementing the right control scheme. Robot dynamics can be considered either elastic, e.g., see [49], or rigid. Our emphasis in this research is on rigid robots. Accordingly, the most important subjects in the problem of cooperation are, i) CRM dynamics and kinematics modeling, and, ii) Control strategy.

CRM Dynamics and Kinematics Modeling

Cooperative robots have complex dynamics and kinematics, and different methods have been suggested for modeling the system [50, 51, 52, 53, 31, 54, 55, 56, 29, 57, 58, 59, 60, 61, 62, 63, 64, 65, 66, 67, 68, 69]. To develop a controller which meets given motion task specifications, the dynamics of the CRM can be represented in either joint space, as in [29, 50, 51, 63, 64, 65, 66, 67, 68, 69], or task space

[27, 28, 30, 31, 51, 55, 70, 71, 72, 73, 74, 75, 76]. Based on the reference frames defined in the dynamical system, the task space modeling can take place at various points. Two common frames which have been used frequently in the literature are the frames attached to the manipulators' end-effector and the frame attached to the manipulated object.

Moreover, other factors which should be considered in the modeling are including, but not limited to, robot redundancy, contact with the environment, and type of connection between the robots and the object. A manipulator is termed kinematically redundant when it possesses more degrees of freedom than it is needed to execute a given task. Non-redundant robot is referred to the case where the dimension of control space is equal to the number of joints in each robot of the cooperation. The problem of redundancy in CRM is studied in [31, 54, 55, 52, 56]. Contact with the environment is discussed in [29, 59], and in [58] the problem of having pin joint between robots and the object is studied. The problem of robot-object connection and its mathematical modeling is studied in Sections 3.3.2 and 3.3.3.

Furthermore, due to the closed chain in CRM, the determination of payload distribution and contact force at the end-effectors, is of important concern. Here, load distribution is referred to the amount of object's load that each robot carries. It is particularly important because it has direct effect on the implementation of the desired action. Note that the contact force can be measured directly by force sensors attached to the end-effectors. However, there are some tasks, where a robot can not have a sensor. One way to solve this problem is using the generalized inverse of the grasp matrix which gives a non-unique solution. The grasp matrix defines the kinematics constraint between the robots and the load. The problem of load distribution has been discussed in [77, 78, 79, 80, 81, 82]. The difficulty in the problem of the

load distribution is finding the motion-inducing and internal forces/moments. The motion-inducing forces/moments balance the object's dynamics, and the internal part consists of compressive, tensile, and torsion forces/moments which do not contribute to the motion of the object. In the research by Erhart and Hirche, a load distribution matrix is introduced which is free of internal wrenches [77]. The suggested load distribution solution is based on the parameterized generalized inverse of the grasp matrix in CRM.

A relevant problem in load distribution is the internal force produced at the end-effectors. Nakamura et al. proposed a method to find the internal force in CRM which is based on finding the minimal forces for the specified resultant force (force applied to load) under the static frictional constraints [78]. Finding the internal force using an optimal solution based on minimizing the difference between desired and actual contact force has been discussed in [79]. Walker et al. in [80] found the internal force in CRM based on an arbitrary vector that appears when pseudoinverse of grasp matrix is used. The arbitrary vector is found based on a function of applied joint torques and the Jacobian matrix of robots.

The load distribution along with the other discussed problems are some challenges that exist in CRM modeling. The next section is dedicated to the control of CRM.

Control Strategy

CRM tasks involve interaction between the robots and a payload, and the force-position relationships between them are of fundamental concern. For trajectory tracking, various control approaches have been proposed, with the impedance control technique being prevalent. The concept of impedance relation for the robotics application was first introduced by Hogan [83]. Impedance control constitutes an effective, easy-

to-implement scheme for multiple interacting dynamical systems. Impedance control includes regulation and stabilization of robot motion by establishing a mathematical relationship between the interaction forces/moments and the robot trajectories. The relation is usually defined as a second-order linear non-homogeneous ordinary differential equation, often modeled after a forced spring-mass-damper system. However, other unconventional impedance relations other than the conventional mathematical equation are used in the literature [84, 85]. Impedance control has been used for CRM in many works, for instance [85, 86, 28, 27, 87, 71, 63, 30, 88, 89, 64, 90, 84].

One of the main differences among various approaches is the definition of terms and the structure of the impedance relationship. This includes different choices of the forces or moments in the impedance relation [86, 27], the use of nonlinear [84], or variable [30] inertial, stiffness and damping characteristics. Caccavale, et al. [86] and Bonitz and Hsia [27] frameworks established the basis of many impedance control schemes introduced for CRM. The proposed impedance control by Caccavale, et al. used an impedance relation in the payload frame by utilizing the feedback of applied force to the load, and another impedance relation in the robot's frame at the end-effector. Bonitz used the idea of internal force in impedance relation, where the difference between actual and desired internal force is used as the feedback to the impedance relation.

Furthermore, impedance control is useful when the payload handled by the CRM may also be in contact with the environment. The algorithm of [64] controls motion and internal forces of the payload, as well as the contact forces between the payload and environment. In that work, the reference trajectory for each robotic joint is calculated based on an impedance relationship such that the desired internal and contact forces are achieved. In [90] the problem of assembly operations using CRM was considered. Experiments showed the effectiveness of impedance controls

for typical tasks encountered in CRM systems.

Impedance relationships have also been used in conjunction with adaptive control, as an alternative to reduce the system's sensitivity due to modeling mismatch. In [71], an adaptive strategy is used to generate a desired motion trajectory in compliance with desired forces at the end effectors, even when the payload stiffness is unknown. Furthermore, adaptation is used in [63] to obtain variable damping and stiffness, exhibiting different impedance characteristics according to the forces exerted by the environment.

The flexibility in the definition of impedance relation terms allows for more convenient definition of the impedance relation, such that the motion task can be achieved with better versatility. An example of such versatility is variable impedance, where the inertia, stiffness, and damping gains in the impedance relation can be defined as variable values, e.g., a function of time. In [30], impedance controllers with variable stiffness for dual-arm cooperative robot grasping a common object interacting with the environment are proposed. A PD-based control algorithm for approximating the stiffness is introduced, which make the control system possess adaptive feature in both the external force and the internal force control. In [91, 92, 93] a concept called energy-storing tank is introduced which ensures passivity of variable impedance. The method is based on incorporating a new variable that creates a reservoir tank to store the dissipated energy by impedance relation. Based on this method, a passive variable impedance is created. Another method to create variable impedance is learning algorithms. In [94, 95] learning algorithms such as reinforcement learning have been used to create the variable gains. An advantage of variable impedance control is its adaptability, often referred as adaptive impedance control [71, 63, 96, 97]. In [63] an adaptive impedance relation, with variable stiffness and damping, is proposed which the adaptation obtained from Lyapunov stability theory. The research in [96]

introduced a variable impedance that compensates for uncertainties (in terms of unknown geometrical and mechanical properties) in the environment. The adaptability of impedance for human-robot interaction is also investigated in [98, 99, 100]. Finally, the stability of a variable impedance has been discussed in [101]. Other cooperative situations where impedance relation was used include: impedance control for mobile CRM [88] and redundant robots [55].

Beside the impedance relation, which is the most well-known approach for CRM control, other control approaches have been used to control the CRM, such as adaptive, fuzzy, etc. Different adaptive approaches have been used, mainly to confront various uncertainties [102, 65, 66, 74, 103, 75, 104, 76, 67, 105, 68], fuzzy based control has been used in [106, 69, 107], neural network (NN) technique is used in [54, 108], State-dependent Riccati equation is utilized in [109, 53], and cascade control scheme is proposed in [110].

Authors of [102] proposed an adaptive control scheme for trajectory tracking and internal force control. Kawasaki in [65] developed a controller for CRM which is robust against uncertainty in robot and object dynamics. The uncertainty for payload with unknown geometry, the center of mass, and inertia is studied in [74]. A robust adaptive control is developed in [105] which is less complex, computationally fast, and feasible for real-time applications.

1.3 Problem Statement

This dissertation focuses on two unique but not entirely independent problems. The first problem is related to energy-oriented modeling and control of robots with BLDC motors. The current state of the art for energy regeneration in BLDC motors is merely depending on using an inverter, which consists of switches. Also, the dynamics of the motor has not been considered for any proposed energy-oriented control. Based on

these observations, we set the hypothesis of the first problem as *the possibility of increasing energy regeneration by incorporating the dynamics of the motor and the robot*. To this end, we devised and introduced two control schemes, namely current regulation and voltage regulation.

The second problem is related to energy-oriented modeling and control of CRM. Based on the results published by the previous works, it is shown that, there is a great chance of energy regeneration in single robots. In those works, robots are either isolated without any contact with the environment, or have limited (in the sense of low and intermittent interaction forces) interactions with it. Accordingly, interactions were not modeled and regarded as external disturbances. The established framework arose the question of the possibility of energy regeneration in cooperative robots. Therefore, in the second problem, we provide *a bridge between energy-oriented control works and the subject of cooperative robots, considering the stability of interactions*.

1.4 Specific Aims

Objective 1: Design a controller based on BLDC motor current regulation.

The dynamics of BLDC motor will be considered and the augmented model of robot-joint mechanism-motor will be obtained. The energy extraction from the ESE will be obtained as a function of the robot's states and the applied current to the motor, and a constraint optimization problem will be formed. An analytical solution will be obtained which maximizes energy regeneration.

Objective 2: Design a controller based on BLDC motor voltage regulation.

We seek to introduce a novel motor driver which has superiority in terms of energy

regeneration in comparison to an off-the-shelf inverter. To this end, the dynamics of BLDC motor is considered and an augmented model for the robot-joint mechanisms-motors will be introduced and a voltage-based control scheme will be developed. The control law will be obtained by specifying an outer-loop torque controller followed by minimization of power consumption via online constrained quadratic optimization. Finally, an experiment will be conducted to assess the performance of the proposed concept against an off-the-shelf driver.

Objective 3: Develop a comprehensive model for CRM and design an impedance-based energy-oriented controller.

The problem of trajectory tracking of cooperative manipulators grasping a rigid load, will be considered. First, a comprehensive model of all robots, the joint mechanisms, and DC motors will be presented, and an impedance-based control scheme will be introduced. Using the energy balance between the ESE and robots, a function representing the energy consumption will be introduced and the gains of the impedance relation will be tuned such that the energy consumption is minimized. Furthermore, the stability of the system will be studied using the passivity theorem.

1.5 Outline

This dissertation is organized as follows:

- *Chapter 2* details the development of controller for BLDC motor based on actuator current and voltage regulation, respectively.
- *Chapter 3* details the theories developed in passivity by the author. Then the modeling of CRM is introduced. The challenges and limitations are explained, and an impedance-based controller is adopted for the problem. The optimiza-

tion is formulated and finally the simulation of two cooperative RRR planar robots is demonstrated.

- *Chapter 4* presents the final conclusion based on results obtained in chapters two and three. The future works are explained and recommendations to improve the work are listed.

CHAPTER II

ENERGY-ORIENTED MODELING AND CONTROL OF ROBOTS WITH BRUSHLESS DC MOTORS

2.1 Introduction

In this chapter, we study the trajectory tracking control problem of a robotic manipulator actuated by brushless DC (BLDC) motors. We set the main objective as developing an energy-optimal control scheme. In this regard, we consider an n -degree of freedom open-chain robot manipulator. All joints are revolute, and each joint is actuated by a BLDC motor, using a joint mechanism (JM). The robot has $n = n_1 + n_2$ degrees of freedom where n_1 joints are fully-active and n_2 joints are semi-active. A fully-active JM exchanges mechanical power with the robot and with an external power supply. A semi-active JM exchanges electric power with an energy storage element (ESE), e.g., an ultracapacitor, and mechanical power with the robot, without a connection to external power supplies. The model allows for any number of semi-active joints, ranging from zero to the number of joints. Each semi-active joint uses a self-contained regenerative control unit (RCU). Energy storage through regeneration is not possible with fully-active drive systems, which draw energy from an external source. The semi-active drives considered here are used to achieve simultaneous motion control and energy management tasks. There are two scenarios for powering

semi-active joints. They can be all connected to a common ESE (star configuration), or each semi-active joint can be individually connected to an ESE (distributed configuration). The problem of comparison between star and distributed configurations is studied in [18] which reveals no superiority of any method over the other one in terms of energy saving. In this chapter, the developed controller in Section 2.3 is based on the distributed configuration, and the developed controller in Section 2.4 is based on the star configuration. It should be noticed that the controllers can be easily modified for both power configurations.

The proposed controllers in this chapter are based on the framework of semi-active virtual control (SVC) strategy introduced first time in [4]. To develop the control signal, the first step is to model the dynamics of the system. That is the augmented dynamics model of the robot, JMs and the BLDC motors. The next step is to form an optimization, based on the motors' energy consumption, to obtain the control signal that minimizes the energy consumption. To this end, two control schemes are proposed for optimization and motor control:

- Actuator current regulation
- Actuator voltage regulation

In the former method, it is assumed that an off-the-shelf three-phase inverter applies voltage to the BLDC motor, and the space vector pulse width modulation (SVPWM) technique is used to generate voltage commands for the inverter [21]. A PI controller is used to generate voltage commands for the inverter based on reference currents. A method is developed to obtain actual torque based on the desired torque generated by a virtual controller. A novel optimization approach is used to generate reference currents that maximize the amount of regenerative energy stored in the ESE subject to the torque demanded by the virtual controller. Finally, an explicit solution is found

for the optimal current references [5]. In the latter method, a novel drive design is introduced, featuring three independent regenerative drives interconnected in a wye configuration. Energy regeneration is optimally managed with the aim of improving the energy efficiency of robot motion controls. A voltage-based control scheme is developed. The control law is obtained by specifying an outer-loop torque controller followed by minimization of power consumption via online constrained quadratic optimization.

The remainder of this chapter is organized as follows: In Section 2.2, the dynamics of the manipulator and JMs are introduced. In Section 2.3, the current regulation method is developed. The merits of the control algorithm are demonstrated in simulation. In Section 2.4, a new motor drive concept is developed, and the voltage regulation method is introduced and applied to the motor driver. Finally, two experiments are conducted to validate the developed control and assess the performance of the proposed driver concept against an off-the-shelf driver.

2.2 Manipulator Dynamics Model

We consider the standard robot dynamics, without the drive systems and JMs, modeled as:

$$M^o(q)\ddot{q} + C^o(q, \dot{q})\dot{q} + g(q) = \tau \quad (2.1)$$

where $q \in \mathbb{R}^n$ is the vector of the joint coordinates, $M^o(q)$ is the inertia matrix, $C^o(q, \dot{q})$ is the matrix representing centripetal and Coriolis effects, $g(q)$ is the gravity vector, and $\tau \in \mathbb{R}^n$ is the vector of torques applied at the joints [111]. To model the JM, the relationship between the vector of joint torques applied to the robot and the vector of induced torque of the motors is given by:

$$\tau = -\mathbf{m}\eta^T\eta\ddot{q} - \mathbf{b}\eta^T\eta\dot{q} + \eta^T\tau_{ind} \quad (2.2)$$

where $\mathbf{m} = \text{diag}(m_j) \in \mathbb{R}^{n \times n}$, $j \in \{1, \dots, n\}$, $\eta = [\eta_1, \dots, \eta_n]^T \in \mathbb{R}^n$, and $\mathbf{b} = \text{diag}(b_j) \in \mathbb{R}^{n \times n}$. Parameters m_j , η_j , and b_j are the j th JM moment of inertia, gear ratio, and friction coefficient, respectively. $\tau_{ind} = [\tau_{ind_1}, \dots, \tau_{ind_n}]^T \in \mathbb{R}^n$ is the vector of the induced torques generated by the BLDC motors [4, 34]. By substituting the dynamics of JMs in the dynamics of the robot, an augmented model of robot and JMs can be obtained. The substitution requires actuator electrical modeling, i.e., finding τ_{ind} in Eqn. (2.2), which is done in the following sections.

2.3 Control Strategy Based on Actuator Current Regulation

For the current regulation control method, it is assumed that the motor is connected to the output of an inverter to realize torque control. The inverter applies voltages with desired waveforms to the motor windings. Appropriate voltage waveforms are generated by an inner-loop controller (typically of the proportional-integral type) receiving reference currents. In turn, reference currents are calculated by a cascaded controller to produce the desired torque. In our control strategy, desired torques are generated by an outer virtual control loop, designed for robot motion tracking.

To develop the controller, first, it is convenient to introduce the construction and operating principle of a BLDC motor.

2.3.1 BLDC Motor Morphology

The structure of a BLDC motor consists of a stator and rotor. The main design principle of a BLDC motor is to eliminate the mechanical commutator. In DC motors, the brushes make the directions of the main magnetic field and the armature magnetic field perpendicular to each other (commutation). In a typical BLDC motor, the brushes are abandoned by placing the windings (phases) in the stator and the permanent magnet (PM) in the rotor as shown in Fig. 5. Here the focus is on such

PMBLDC motors, termed BLDC which have three windings. In a three phase motor, there are two connection modes; Wye connection and delta connection [2]. The Wye connection is most commonly used, in which the three phase windings are connected symmetrically as shown in Fig. 6 a. The motor driver energizes windings such that the PM rotates according to the desired motion task. The principle is that the north pole of the rotor is aligned with the south pole of the energized winding and the south pole of the rotor has a tendency to align with the north pole of the energized winding.

There are generally three reference frames used to analyze the motor states. The Stator reference frame $a-b-c$, which is attached to the stationary windings and the a , b , and c axes are co-planar, at 120 degrees to each other.

The rotor frame $d-q$, in which the d axis is along the North and South poles or along the flux vector of the rotor, and the q axis is at 90 degrees to the d axis. Thus, the reference frame is also an orthogonal reference frame. Finally, an orthogonal reference frame $\alpha-\beta$ in the same plane as the stator reference frame so that the angle between the two axes is 90 degrees instead of 120 degrees. The a axis is aligned with α axis in the second frame. The frames are shown in Fig. 6 b. In this study, all frames are used for motor modeling. The details are explained in Sections 2.3.2 and 2.4.1.

2.3.2 BLDC Motor Modeling

To develop the controller, first we study the connection between the BLDC motor and the motor driver, and the governing equations. The inverter input terminals (bus voltage) are connected to a constant voltage power source for the active joints and an ESE for the semi-active joints. We assume each semi-active joint is connected to an individual ESE. The setup of ESE, the inverter, and equivalent circuit model of the BLDC motor is shown in Fig. 7, where the equivalent circuit for each phase consists of a resistor, an inductor and a change in flux linkage due to the permanent

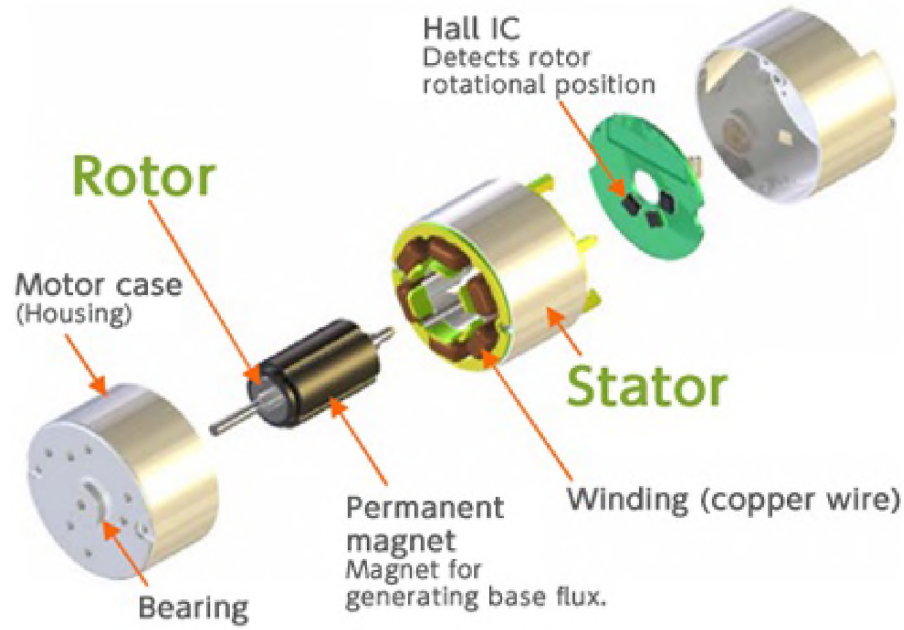


Figure 5: Structure of BLDC motor. The picture is adopted from <https://www.nidec.com/en/technology/capability/brushless>.

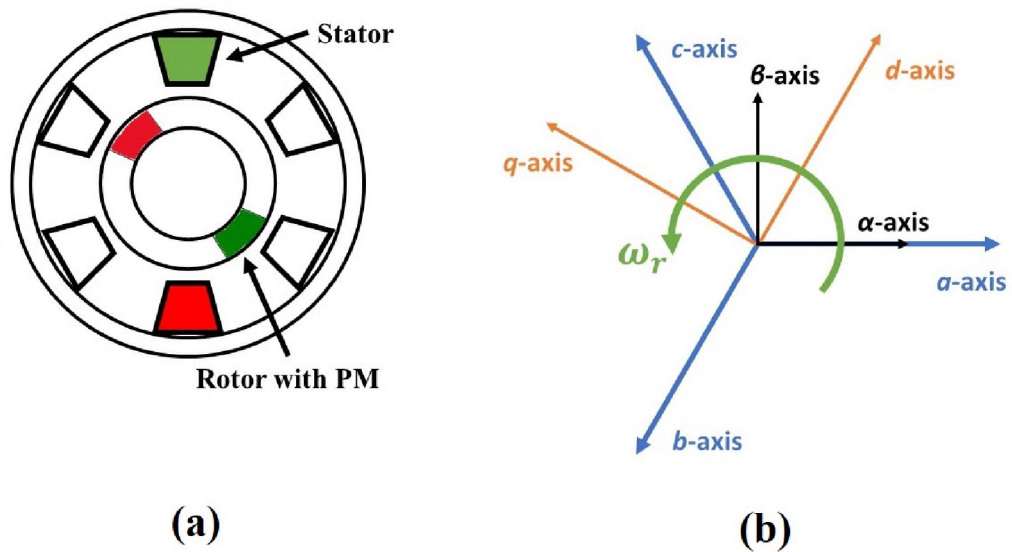


Figure 6: (a) Cross section view of a three phase BLDC motor with PM rotor and three windings. (b) The $a-b-c$, $d-q$, and $\alpha-\beta$ reference frames.

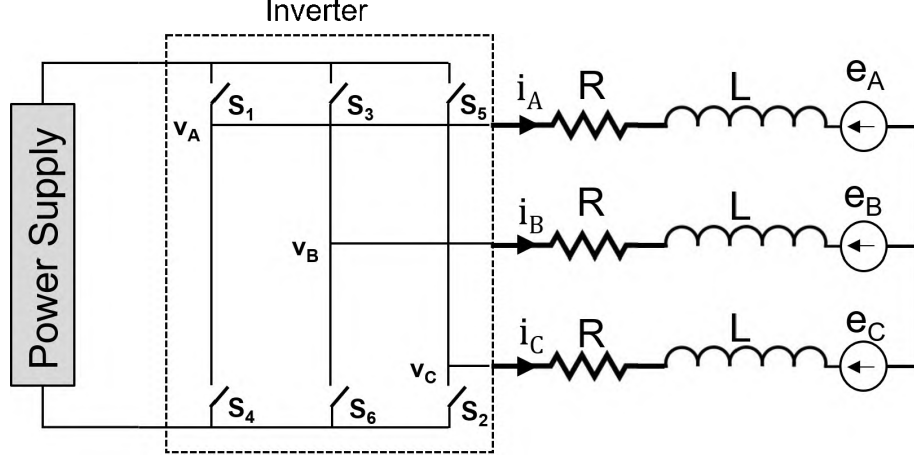


Figure 7: Power supply, inverter, and equivalent circuit model of the motor of the j th JM. The subscript j is dropped in the plot.

magnets. Three windings have 120° (electrical) phase displacement among them. For control purposes, the motor dynamics is presented in a two-phase frame which is the rotor reference frame. This approach is called d - q modeling due to the definition of a direct-quadrature coordinate frame for the phase currents. For the BLDC motor that is connected to the j th joint of the robot, the current dynamics in the d - q frame can be expressed as [2]:

$$\frac{d}{dt}(i_{q_j}) = \frac{1}{L_{q_j}} \{-R_{s_j} i_{q_j} - \omega_{r_j} (L_{d_j} i_{d_j} + \lambda_{f_j}) + v_{q_j}\} \quad (2.3a)$$

$$\frac{d}{dt}(i_{d_j}) = \frac{1}{L_{d_j}} \{-R_{s_j} i_{d_j} + \omega_{r_j} L_{q_j} i_{q_j} + v_{d_j}\} \quad (2.3b)$$

where i_{d_j} and i_{q_j} are the stator currents, v_{d_j} and v_{q_j} are the voltages, and L_{d_j} and L_{q_j} are the inductances. Subscript d indicates the parameter for the d axis and Subscript q indicates the parameter for the q axis. λ_{f_j} is the amplitude of the permanent magnets' flux linkage, R_{s_j} is the stator phase resistance, and ω_{r_j} is the rotor angular velocity. The induced electromagnetic torque (τ_{ind_j}) is directly obtained

from the currents using:

$$\tau_{ind_j} = \frac{3P_j}{4}(\lambda_{f_j}i_{q_j} + (L_{d_j} - L_{q_j})i_{d_j}i_{q_j}) \quad (2.4)$$

where P_j is the number of poles in the motor. It follows from Eqn. (2.3) and (2.4) that v_{d_j} and v_{q_j} are the inputs to the first-order differential equations in Eqn. (2.3) which the solution gives the torque. Hence, to find the torque, we need to find the voltages. The inverter is used to apply voltage on each phase of the stator. Several methods are available to sequence the inverter switches, such as different variations of pulse width modulation (PWM). Among all PWM techniques, space vector PWM (SVPWM) is regarded as the most efficient, and chosen for this part [2].

The schematic of an inverter is shown in Fig. 7, where $S_{i_j}, i \in \{1, \dots, 6\}$ are the transistors used as switches. The objective is to follow desired voltages by turning switches on/off at the right times. There are three pairs of switches: $\{S_{1_j}, S_{4_j}\}$, $\{S_{3_j}, S_{6_j}\}$ and $\{S_{5_j}, S_{2_j}\}$. In each pair, only one switch can be on at a time, otherwise; a short circuit happens. It can be shown that the output voltage for each winding, i.e. $v_{A_j}, v_{B_j}, v_{C_j}$, can be obtained from [21]:

$$\begin{bmatrix} v_{A_j} \\ v_{B_j} \\ v_{C_j} \end{bmatrix} = \frac{V_s}{3} \begin{bmatrix} 2 & -1 & -1 \\ -1 & 2 & -1 \\ -1 & -1 & 2 \end{bmatrix} \begin{bmatrix} A_j \\ B_j \\ C_j \end{bmatrix} \quad (2.5)$$

where V_s is the voltage of the power supply and A_j, B_j, C_j are the binary states (1:on, 0:off) of switches S_{1_j}, S_{3_j} , and S_{5_j} , respectively.

The SVPWM method is chosen to control the switches so that the desired voltages are produced at the inverter's output. Due to its detailed nature, the method is outlined briefly in Appendix A. Note that the voltage supplied to the inverter is

constant (DC bus) for the active joints but variable for the semi-active joints due to the use of an ESE. Note also that the voltages obtained from Eqn. (2.5) are given in the a - b - c frame, where each axis is along one of the phases. In order to be able to use these values, they should be transformed and presented in d - q frame.

2.3.3 Augmented Dynamics Model of Robot and JMs

Combining Eqns. (2.1) and (2.2) results in the following augmented model:

$$M(q)\ddot{q} + C(q, \dot{q})\dot{q} + g(q) = \mathcal{T}_{ind} \quad (2.6)$$

In the coupled dynamics, M^o and M are same in all elements except in diagonal elements such that $M_{jj} = M_{jj}^o + m_j\eta_j^2$, also C and C^o are only different in diagonal terms such that $C_{jj} = C_{jj}^o + b_j\eta_j^2$ and $\mathcal{T}_{ind} = [\eta_1\tau_{ind_1}, \dots, \eta_n\tau_{ind_n}]^T$. The right-hand side of Eqn. (2.6) in the augmented model is the control input available to the designer. It is a function of the induced torques produced by the BLDC motor connected to a JM, as in Eqn. (2.4).

2.3.4 Control Scheme

The control scheme is summarized by the block diagram of Fig. 8. In this figure, all parameters with superscript $(.)^*$ are desired values. The H_1 and H_2 functions give the optimal currents and function F is given by Eqn. (2.4). Any robot control algorithm compatible with the motion objectives (here tracking) can be used as an outermost loop, considering the right-hand side of augmented model in Eqn. (2.6) as a virtual control. Suitable virtual controllers include inverse dynamics, passivity-based robust control, adaptive control, sliding mode control and so forth. Here, we assume the inverse dynamics technique is used as the virtual controller. The controller generates a desired acceleration \mathbf{a} to calculate the vector of desired induced torques,

\mathcal{T}_{ind}^* . If the motors exactly produce the desired torques, then the robot will follow the reference trajectory and will inherit any stability, robustness and performance guarantees associated with the virtual design. In [4] this is termed *exact virtual matching*.

In each joint, using the desired torque, the corresponding desired currents are related through Eqn. (2.4). In field-oriented control, the choice of $i_{d_j}^* = 0$ is commonly made to maintain orthogonality between rotor and stator fields. Setting $i_{d_j}^* = 0$ results in $i_{q_j}^* = 4\tau_{ind_j}^*/(3P_j\lambda_{f_j})$ and torque is proportional to $i_{q_j}^*$, making the inherently AC motor behaves like a DC motor [44, 2]. We make the key observation that $i_{d_j}^* = 0$ is not necessary to achieve the virtual torque demand nor to accomplish of the motion tracking objective. Moreover, such selection will be shown to be sub-optimal relative to energy efficiency.

Henceforth, for simplicity, the subscript j , indicating joint number, is dropped; hence the result in this section is valid for any joint of the robot assuming all joints are using identical motors. If the desired current references have been determined, i.e., i_d^* and i_q^* , the desired inverter output voltages can be determined with a current-control loop. Current-control of inductance-resistance coil dynamics is usually accomplished with proportional-integral (PI) control using current as the control input [44, 112]. With this choice, the control voltages are found from:

$$v_d^* = P_d e_d + I_d \frac{d}{dt}(e_d) - \bar{P}_q \omega_r e_q \quad (2.7a)$$

$$v_q^* = P_q e_q + I_q \frac{d}{dt}(e_q) + \bar{P}_d \omega_r e_d \quad (2.7b)$$

where $e_d = i_d^* - i_d$, $e_q = i_q^* - i_q$ and $P_d, P_q, I_d, I_q, \bar{P}_d, \bar{P}_q$ are controller gains. Having the desired voltages in the d - q frame, the voltage in a - b - c frame can be found using Park's transformation. The transformation can be used to transform any variable, e.g.

voltage, current, or flux linkage, from a - b - c frame to d - q frame. The transformation is defined as:

$$\begin{bmatrix} f_q \\ f_d \\ 0 \end{bmatrix} = \frac{2}{3} \begin{bmatrix} \cos(\theta_r) & \cos(\theta_r - \frac{2\pi}{3}) & \cos(\theta_r + \frac{2\pi}{3}) \\ \sin(\theta_r) & \sin(\theta_r - \frac{2\pi}{3}) & \sin(\theta_r + \frac{2\pi}{3}) \\ 0.5 & 0.5 & 0.5 \end{bmatrix} \begin{bmatrix} f_A \\ f_B \\ f_C \end{bmatrix} \quad (2.8)$$

where θ_r is the rotor's angle measured relative to the d -axis and f can be any parameter like voltage and current, with q and d axis components labeled f_q and f_d , respectively. Here the inverse of the transformation is useful in transferring the outer-loop commands into inner-loop commands [2, 21]. This transformation is shown in Fig. 8 as the P_{dq}^{ABC} block. The outputs of this block are three desired voltages which should be produced by the inverter using SVPWM. The space vector method is done in an orthogonal reference frame, $\alpha - \beta$, the same plane as the stator reference frame [44]. The voltages in this frame can be obtained from Eqn. (2.9) (Clark transformation) [2, 44]. Note that the details of SVPWM is outlined in appendix A.

$$\begin{bmatrix} v_\alpha^* \\ v_\beta^* \end{bmatrix} = \frac{2}{3} \begin{bmatrix} 1 & -0.5 & -0.5 \\ 0 & \sqrt{3}/2 & -\sqrt{3}/2 \end{bmatrix} \begin{bmatrix} v_A^* \\ v_B^* \\ v_C^* \end{bmatrix} \quad (2.9)$$

The output of the inverter is transformed to the d - q frame using Park's transformation. These voltages are applied to the BLDC motor dynamics, and the induced torque is calculated using Eqn. (2.4). It should be noted that the active joints are connected to a constant voltage bus, V_{dc} , appearing in Eqn. (2.5). The semi-active joints use ESE, e.g., an ultracapacitor, as a power source. The ESE voltage, v_s , is used in Eqn. (2.5) for the semi-active joints. It is worth mentioning that in online implementation, after finding the desired voltages, i.e., $[v_A^*, v_B^*, v_C^*]$, they should be

applied directly to the inverter.

2.3.5 Energy Balance

In the control scheme, explained in the previous section, the desired currents are calculated from the desired torque created by the virtual control. The energy balance between BLDC motor and ESE can be utilized to form an optimization and find H_1 and H_2 functions in Fig. 8. We assume each semi-active joint is connected to an individual ESE. Then each semi-active joint introduces a state variable, namely the charge of the ESE, y_j . This variable is not controlled, but rather monitored or used as part of optimization problems. The dynamics of this variable is the function of ESE model. Usually, it is hard to model ESE, due to the internal complexity of energy storage media. Therefore, it is hard to determine the change of the charge in the ESE. In this study, we use the real-time voltage feedback of the ESE and virtual control, as explained in Section 2.3.4, to eliminate the need for a model of the ESE. The energy balance can be used to represent the charge change as a function of systems states and ESE voltage. Note that states and voltage are easily accessible for online implementation.

All results obtained in this section and next section are valid for each semi-active joint. For ease of notation, the subscript j , indicating joint number, is dropped from equations. To model the energy change in the ESE, we make the key assumption that the energy exchange media, i.e., inverter, is perfect. That is, no energy is lost during energy transfer. Therefore, the input power is equal to the output power. The input/output energy balance for the inverter can be written according to:

$$v_s i_s = v_A i_A + v_B i_B + v_C i_C \quad (2.10)$$

where v_s is the voltage of the ESE and i_s is the current flowing between the ESE and

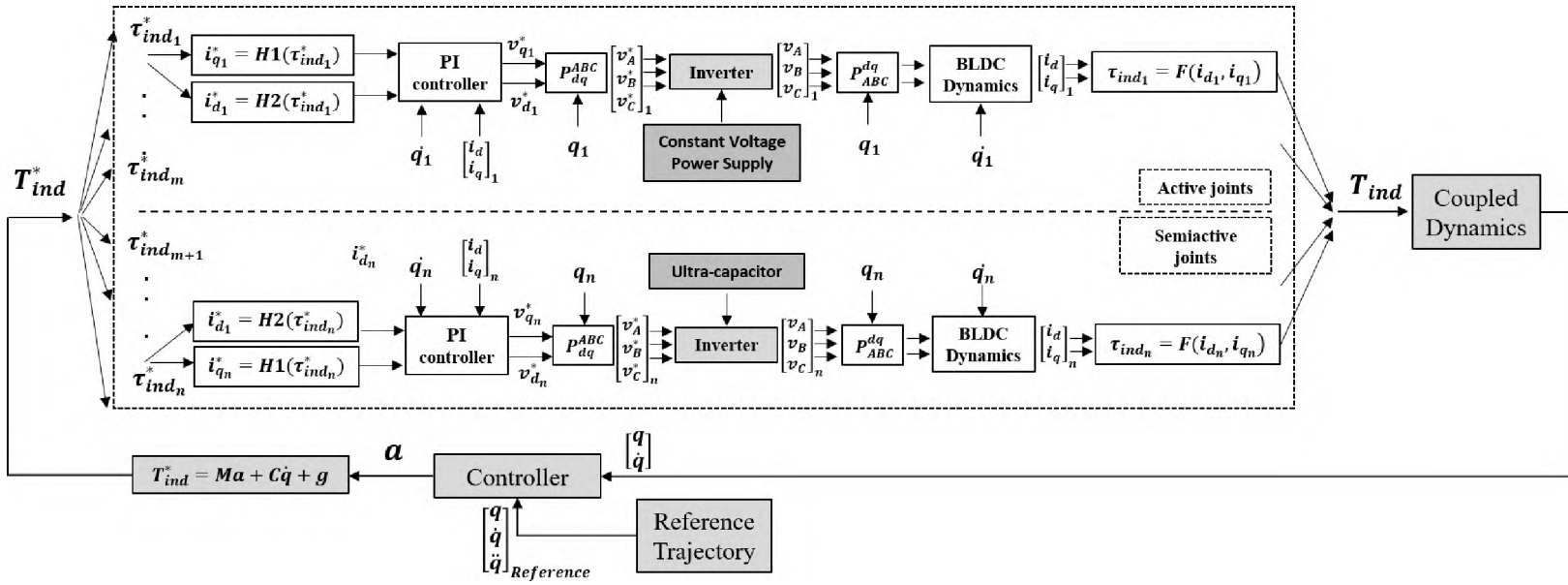


Figure 8: Current regulation Control scheme of augmented model of robot considering BLDC motor dynamics.

the inverter. Assume that the inverter has no energy losses and that the PI current loop achieves perfect tracking of currents, i.e. all desired currents are effective, using the Park transformation, substituting Eqn. (2.3) into Eqn. (2.10) and taking the integral in an arbitrary time interval $[t_1, t_2]$, the internal energy balance equation can be obtained after some algebra as:

$$\Delta E_s = -\frac{3}{2} \int_{t_1}^{t_2} \{I^{*T} \mathcal{G}_1 I^* + \mathcal{G}_2 I^* + I^{*T} \mathcal{G}_3 \frac{dI^*}{dt}\} dt \quad (2.11)$$

where ΔE_s is the change of electric energy in the ESE, $I^* = [i_q^*, i_d^*]^T$, and:

$$\mathcal{G}_1 = \begin{bmatrix} R_s & (L_d - L_q)\omega_r \\ 0 & R_s \end{bmatrix}, \quad \mathcal{G}_2 = \begin{bmatrix} \omega_r \lambda_f & 0 \end{bmatrix}, \quad \mathcal{G}_3 = \begin{bmatrix} L_q & 0 \\ 0 & L_d \end{bmatrix}$$

A value of $\Delta E_s > 0$ indicates $E_s(t_2) > E_s(t_1)$, hence energy regeneration and $\Delta E_s < 0$ indicates energy consumption [18]. If the ESE is an ultracapacitor, and we use a simple model for the dynamics of the ultracapacitor, then the charge change may be obtained from:

$$\Delta E_s = \frac{y^2(t_2) - y^2(t_1)}{2C} \quad (2.12)$$

where C is the capacitance of the ultracapacitor. The last term in Eqn. (2.11) contain derivatives of currents and represent inductive energy storage (ΔE_I). This term can be integrated and written as:

$$\Delta E_I = \frac{3}{2} \frac{L_q}{2} (i_q^{*2}(t_2) - i_q^{*2}(t_1)) + \frac{3}{2} \frac{L_d}{2} (i_d^{*2}(t_2) - i_d^{*2}(t_1)) \quad (2.13)$$

We note that the energy is stored in and released from the inductance, not lost. Also, inductive energy storage is expected to be very small in comparison with the energy stored in the ESE.

2.3.6 Energy Optimization

Equation. (2.11) can be used to predict the changes in stored energy in the ESE and can be used as a basis for optimization problems, as done with DC motors without considering inductance in [6, 113, 3]. Eqn. (2.11) indicates that the amount of energy stored in the ESE depends on how d - q axis currents are selected under the constraint of Eqn. (2.4). This leads to the question of how to select i_d^* and i_q^* to maximize regenerative energy storage in the ESE. Mathematically, the objective is to find i_q^* and i_d^* to maximize the right-hand side of Eqn. (2.11), while the admissible trajectories of currents lie on a specific surface considered as the constraint. Therefore, the optimization problem can be defined as:

$$\max_{i_q^*, i_d^*} \Delta E_s \quad (2.14a)$$

$$\text{Subject to: } \frac{3P}{4}(\lambda_f i_q^* + (L_d - L_q)i_d^* i_q^*) - \tau_{ind}^* = 0 \quad (2.14b)$$

This problem falls in the category of constrained optimization of a functional, and it can be solved using the following Theorem:

Theorem 1 *Constrained Optimization of Functional:*

Consider the following constraint optimization problem:

$$\min_{\mathbf{X}} J(\mathbf{X}) = \int_{t_1}^{t_2} g(\mathbf{X}(t), \dot{\mathbf{X}}(t), t) dt \quad (2.15a)$$

$$\text{Subject to : } \mathbf{h}_i(\mathbf{X}, t) = 0, \quad i = 1, \dots, n \quad (2.15b)$$

where $\mathbf{X} \in \mathbb{R}^{n+m}$, J is a scalar-valued objective function, and \mathbf{h}_i is an equality constraint. Note that $n, m \geq 1$. The solution to the optimization can be found by taking the following steps:

1- First, the augmented integrand function is defined as:

$$F_a(\mathbf{X}(t), \dot{\mathbf{X}}(t), \mathbf{L}(t), t) \triangleq g(\mathbf{X}(t), \dot{\mathbf{X}}(t), t) + \mathbf{L}^T(t)\mathbf{h} \quad (2.16)$$

where $\mathbf{L}(t) = [\mathbf{L}_1(t), \dots, \mathbf{L}_n(t)]^T \in \mathbb{R}^n$ is the vector of Lagrange multipliers and $\mathbf{h} = [\mathbf{h}_1, \dots, \mathbf{h}_n]$.

2- The optimal values, i.e., $\mathbf{X}^s(t), \mathbf{L}^s(t)$, can be obtained by solving the following equalities:

$$\frac{\partial F_a}{\partial \mathbf{X}}(\mathbf{X}^s(t), \dot{\mathbf{X}}^s(t), \mathbf{L}^s(t), t) - \frac{d}{dt} \left\{ \frac{\partial F_a}{\partial \dot{\mathbf{X}}}(\mathbf{X}^s(t), \dot{\mathbf{X}}^s(t), \mathbf{L}^s(t), t) \right\} = \mathbf{0} \quad (2.17)$$

which are a set of $n + m$ second-order differential equations, and also the equality constraints in Eqns. (2.15b) which are a set of n algebraic equations. So, there are $2n + m$ equations which form the set of necessary conditions for $\mathbf{X}^s(t)$ to be an optimum [114]. \square

To solve the optimization in Eqn. (2.14), the first step is to form an augmented integrand function, F_a , as:

$$F_a = \frac{3}{2} \{ -R_s(i_q^{*2} + i_d^{*2}) - \omega_r \lambda_f i_q^* - (L_d - L_q) \omega_r i_q^* i_d^* - L_q i_q^* \dot{i}_q^* - L_d i_d^* \dot{i}_d^* \} + \mathbf{L}_1(t) \left\{ \frac{3P}{4} (\lambda_f i_q^* + (L_d - L_q) i_d^* i_q^*) - \tau_{ind}^* \right\} \quad (2.18)$$

where $\mathbf{L}_1(t)$ is the Lagrange multiplier and $\dot{i}_j^* = di_j^*/dt$, $j = \{q, d\}$. The necessary conditions for an extremum can be found using Eqn. (2.17) according to:

$$\frac{\partial F_a}{\partial i_q^*} - \frac{d}{dt} \left\{ \frac{\partial F_a}{\partial \dot{i}_q^*} \right\} = 0 \quad (2.19a)$$

$$\frac{\partial F_a}{\partial i_d^*} - \frac{d}{dt} \left\{ \frac{\partial F_a}{\partial \dot{i}_d^*} \right\} = 0 \quad (2.19b)$$

Using Eqn. (2.19) and with some manipulation and simplification, to eliminate the

Lagrange multiplier, yields:

$$\frac{3P}{4}(L_d - L_q)^2 i_q^{*4} + \lambda_f \tau_{ind}^* i_q^* - \frac{4\tau_{ind}^{*2}}{3P} = 0 \quad (2.20a)$$

$$C_4 i_d^{*4} + C_3 i_d^{*3} + C_2 i_d^{*2} + C_1 i_d^* + C_0 = 0 \quad (2.20b)$$

where:

$$C_0 = -16(L_d - L_q)\tau_{ind}^{*2}$$

$$C_1 = 9P^2\lambda_f^3$$

$$C_2 = 27P^2\lambda_f^2(L_d - L_q)$$

$$C_3 = 27P^2\lambda_f(L_d - L_q)^2$$

$$C_4 = 9P^2(L_d - L_q)^3$$

The above equations are quartic polynomials. Solution to the above equations is the optimal desired current. The quartic polynomials may have zero to four roots, therefore, we investigate the solutions, and we find the optimal values according to the following result.

Main Result:

For a given desired torque, τ_{ind}^* , in Eqn. (2.20), there are two real solutions for each current. In order to maximize energy storage, for i_q^* , the solution which has the same sign as τ_{ind}^* , and for i_d^* , the solution with smaller absolute value, should be chosen.

Justification: A graphical method is used to characterize the solutions to Eqns. (2.20). The graphical argument shows the existence of two real solutions and also identifies the solutions which maximize energy in Eqn. (2.11). For the graphical proof, we assume $L_q > L_d$, however, the same argument can be made for the case $L_q < L_d$.

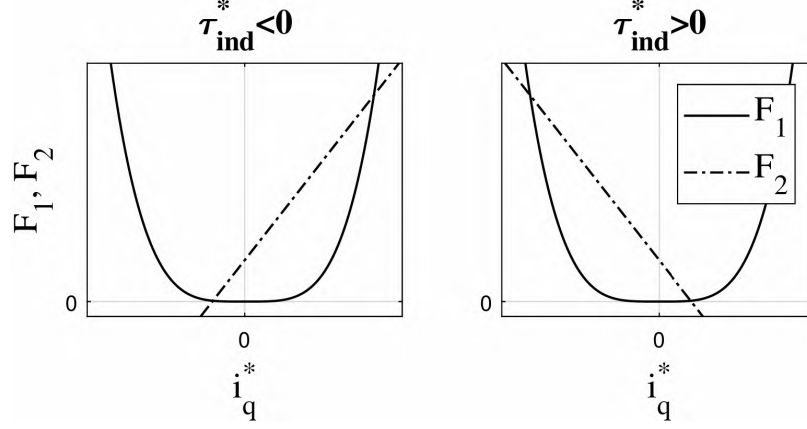


Figure 9: Graphic Demonstration of Solution for Eqn. (2.20a).

Eqn. (2.20 a) can be written as:

$$\frac{3P}{4}(L_d - L_q)^2 i_q^{*4} = -\lambda_f \tau_{ind}^* i_q^* + \frac{4\tau_{ind}^{*2}}{3P} \quad (2.21)$$

Designate the left- and right-hand sides of Eqn. (2.21) as F_1 and F_2 , respectively. The graphs of F_1 and F_2 against i_q^* for positive and negative values of τ_{ind}^* is shown in Fig. 9. F_1 is a quartic even function of i_q^* and F_2 is a linear function of i_q^* with a positive slope for negative τ_{ind}^* and vice-versa. The intersections of F_1 and F_2 shown in the figure are the solutions of Eqn. (2.20a). There are two real solutions, and it is clear that the solution which has the same sign as τ_{ind}^* has a smaller magnitude. To choose between the two solutions, the energy equation should be investigated. In Eqn. (2.11), the right-hand side can be rewritten by using the constraint in Eqn. (2.14 b), factoring ω_r , and moving ΔE_I to the left side as follows:

$$\Delta E_s + \Delta E_I \triangleq \Delta E = \frac{3}{2} \int_{t_1}^{t_2} \{-R_s(i_q^{*2} + i_d^{*2}) - \omega_r \frac{4\tau_{ind}^*}{3P}\} dt \quad (2.22)$$

Under the assumption that inductive energy is much smaller than capacitive energy, that is, $\Delta E \approx \Delta E_s$, we focus on maximizing ΔE . The integrand of Eqn. (2.22) contains quadratic terms in i_q^* and i_d^* and a term in the desired torque, which has

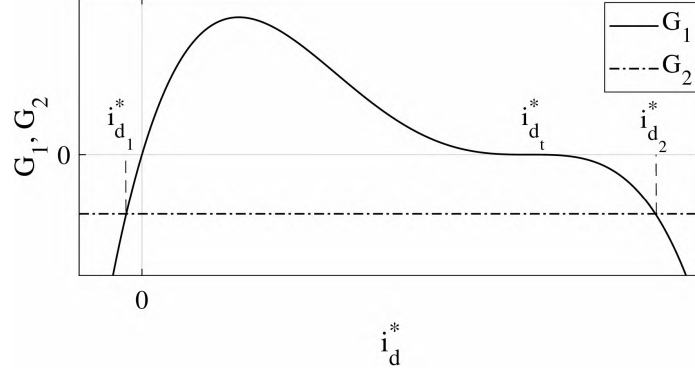


Figure 10: Graphic Demonstration of Solution for Eqn. (2.20b).

been already selected in the outer-loop control and is independent of the currents. Moreover, the selections for i_q^* and i_d^* are independent. Therefore, since $R_s > 0$, to maximize energy and considering the negative sign, the solution for i_q^* with a smaller magnitude should be selected. Note that the plots in Fig. 9 were generated with arbitrary parameters unrelated to those used in the simulation section. In a simulation with realistic parameters, the difference between the two solutions is much larger than shown in the plots.

A similar argument can be followed for the solutions for i_d^* . Indeed, Eqn. (2.20b) can be written as:

$$C_4 i_d^{*4} + C_3 i_d^{*3} + C_2 i_d^{*2} + C_1 i_d^* = 16(L_d - L_q)\tau_{ind}^{*2} \quad (2.23)$$

Designate the left- and right-hand sides of Eqn. (2.23) as G_1 and G_2 , respectively. The graphs of G_1 and G_2 against i_d^* are shown in Fig. 10. Considering the coefficients in the left-hand side, it can be shown that G_1 always has a triple root and one simple root at zero[115]. The triple root is $i_{d_t}^* = \lambda_f / (L_q - L_d)$ and the graph of G_1 is tangent to the i_d^* axis at the location of the root. As seen in the graph, G_2 is a negative constant, represented by a horizontal line which intersects G_1 at two locations, i.e. $i_{d_1}^*$ and $i_{d_2}^*$, which are the solutions to Eqn. (2.23). One solution, $i_{d_1}^*$, is

negative and the other, $i_{d_2}^*$, is larger than $i_{d_1}^*$. Often, $|L_q - L_d|$ is in the range of a few mH, while λ_f is in the order of magnitude of the 1 V/rad/s [46], which results in the negative root having a much smaller absolute value than the triple root. Since the term inside the integral in Eqn. (2.22) is quadratic in i_d^* and negative, the solution with smaller absolute value should be selected. Note that the desired solution has the same sign as $L_d - L_q$. This can also be verified using the results obtained for Eqn. (2.20a). Note that Eqn. (2.14b) can be written as:

$$\tau_{ind}^* = \frac{3P}{4} i_q^* (\lambda_f + (L_d - L_q) i_d^*) \quad (2.24)$$

According to results for Eqn. (2.20a), if τ_{ind}^* is positive or negative, then i_q^* should be positive or negative, respectively. This leads to the necessary condition that the term multiplied by i_q^* , i.e., $\lambda_f + (L_d - L_q) i_d^*$, should be always positive for $L_q > L_d$. Solving the inequality leads to:

$$i_d^* < \frac{\lambda_f}{L_q - L_d} \quad (2.25)$$

which confirms the results obtained from Fig 10. Summarizing, it has been shown that Eqn. (2.20) have two solutions for each current. For i_q^* the solution which has the same sign of τ_{ind}^* should be chosen. Furthermore, for i_d^* , the solution with the same sign as $L_d - L_q$ should be selected. \square

Suboptimal Solutions

If the approximation $L_q \cong L_d$ can be taken as equality, the quartic term in Eqn. (2.20a) can be ignored, which recovers the well-known solutions $i_d^* = 0$ and $i_q^* = 4\tau_{ind}^*/(3P\lambda_f)$. Here, the results clearly identify these solutions as sub-optimal relative to maximization of regenerative energy storage.

The above solutions to Eqn. (2.20) must be implemented online for use by the control system. Many polynomial root-finding algorithms are available for fast real-time implementation.

2.3.7 Preliminary Simulation Results

To illustrate the superiority of the optimal analytical solution over the sub-optimal solution, a rigid planar two-link manipulator is considered with parameters according to Table I. The objective is to follow sinusoidal reference trajectories in both joints. The first joint is active and second joint is semi-active, connected to an ultracapacitor with $C = 500$ F, rated at 12V. The ultracapacitor is fully charged initially. For simplicity, the virtual controller is designed using the inverse dynamics approach [111]. The inverse dynamics control input has the form:

$$\mathcal{T}_{ind}^* = M(q)\mathbf{a} + C(q, \dot{q})\dot{q} + g(q) \quad (2.26)$$

where \mathbf{a} is a new control termed virtual acceleration. With this input, the system is transformed into a set of decoupled double integrators, which are then controlled by specifying \mathbf{a} . Defining the vector of reference trajectories by $q_r = [q_{r1}, q_{r2}]^T$, a simple choice for \mathbf{a} is the proportional-derivative law $\mathbf{a} = \ddot{q}_r - K_1\dot{\tilde{q}} - K_0\tilde{q}$, where $\tilde{q} = q - q_r$ and K_1, K_0 are diagonal matrices consisting of velocity and position gains, respectively. The inverse dynamic approach results in asymptotic tracking of reference trajectories if model information is accurate. In Figs. 11 and 12 the actual and reference angles and the joint angular velocities of both joints are depicted, showing achievement of the tracking objective. The optimal currents were calculated online and chosen using Eqn. (2.20), as shown in Fig. 13. Figure 14 shows the difference between desired and actual currents that are applied to BLDC motor. Furthermore, two optimal solutions obtained from solving Eqn. (2.20) are shown in Fig. 15. One solution for i_d^* has a

magnitude in the order of fifty, while the selected solution is much smaller. Also, one solution for i_q^* is much larger in magnitude than the selected solution, as shown in the plot. Figure 16 shows the time history of the ultracapacitor charge. Overall, the capacitor has a slow discharging trend, but there are periods of time where the capacitor is being charged through regeneration.

The sub-optimal solutions can be obtained for comparison purposes as $i_d^* = 0$ and $i_q^* = 4\tau_{ind}^*/(3P\lambda_f)$. The internal energy balance is used for comparison. Eqn. (2.22) can be written as:

$$\Delta E_c = \Delta E_r + \Delta E_d - \Delta E_I \quad (2.27)$$

where ΔE_r is the term relative to energy dissipation in the resistors (Joule power loss) and ΔE_d is the term on the desired torque. In Table II, the internal energy balance for optimal and sub-optimal solutions are compared. The time period for measurement includes ten complete cycles. The inductive energy storage (ΔE_I) is negligible and ΔE_d is same for both cases, which is expected since this term is not a function of currents. Note that most of the energy dissipation appears in ΔE_r .

Table I: Planar Two-link Robot and BLDC Motor Parameters

Parameter	Symbol	Value	Unit
Length of link $i = \{1, 2\}$	l_i	0.50	m
Mass of link i	m_i	1.00	kg
Moment of inertia of each link	I_{z_i}	0.10	kg-m ²
d-axis inductance	L_d	8.0	mH
q-axis inductance	L_q	20.0	mH
Stator resistance	R_s	0.1	Ω
Flux linkage amplitude	λ_f	0.3	Vs
Sampling time	T_s	0.0001	s

Table II: Optimal and Sub-optimal Energy Comparison (Joule)

Solution	ΔE_c	ΔE_r	ΔE_d	ΔE_I
Optimal	-52.6328	-52.5218	-0.1085	-0.0024
Sub-optimal	-56.4288	-56.3172	-0.1085	-0.0031

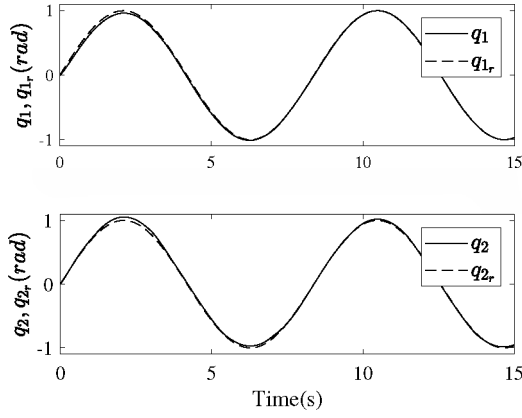


Figure 11: joints' angles tracking desired trajectory.

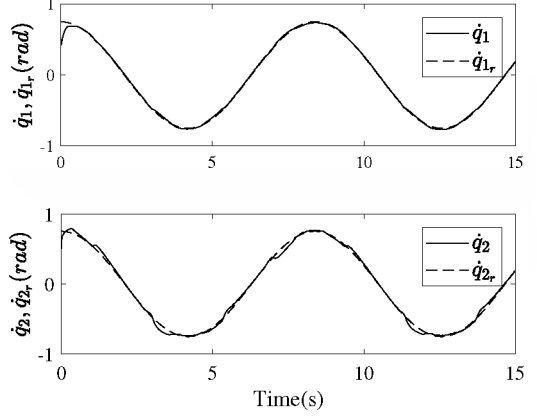


Figure 12: joints' angular velocities tracking desired velocity.

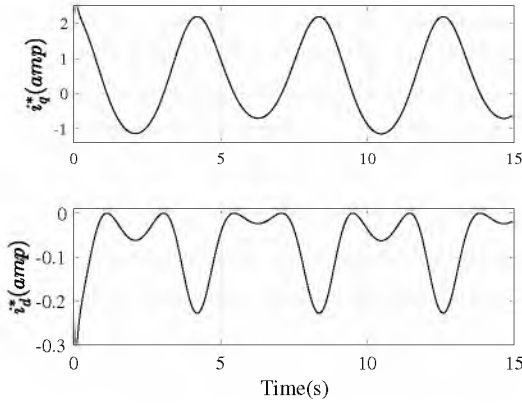


Figure 13: Desired currents on dq axis ($L_q > L_d$).

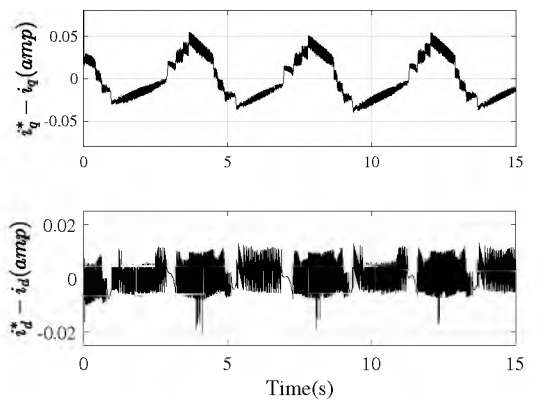


Figure 14: Difference between desired and actual currents.

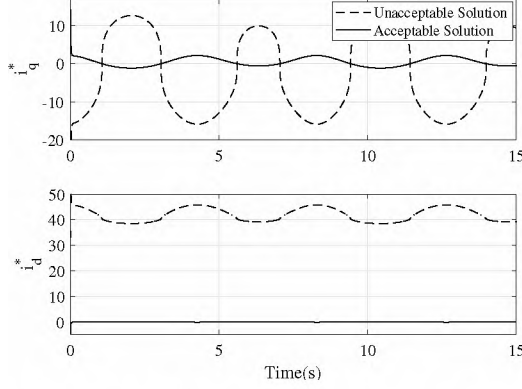


Figure 15: Optimal solutions of currents.

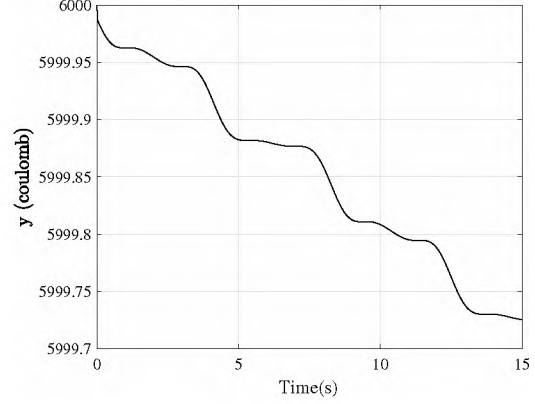


Figure 16: Ultracapacitor charge.

2.3.8 Concluding Remarks

The proposed control scheme was tested using MATLAB SIMULINK environment. The inverter was modeled using logical operators. The preliminary results proved the effectiveness of the method for tracking control of robot manipulator. This method can be applied to most of the off-the-shelf drivers. It should be noticed that the inverter is a regenerative device, therefore, energy regeneration is possible. Despite the advantages, an inverter has its own drawbacks. Inverter has complexity in the circuitry logic with PWM output. The selection of PWM frequency is an issue. The inverter PWM frequency is a trade-off between the switching losses and the ripple currents that occur at high- and low-frequencies, respectively. So to design a controller using an inverter, PWM frequency is an important factor. In terms of energy regeneration, an inverter only allows applying a certain (discontinuous) level of voltage to each phase based on the binary states of its switches. Therefore, despite the desired input voltage of the inverter, fixed number of applied voltage to each phase are available (e.g., in a three-phase inverter, only 8 levels of power source voltage can be applied to each phase). Because of this limitation, the opportunity of energy regeneration based on the motion task is limited.

Despite all the aforementioned disadvantages, using an inverter is the most

common way to control a BLDC motor. So having an energy-oriented method which is capable of being applied to any inverter, opens the doors for further developments and investigations. The suggestions to improve the work are presented in chapter 4.

2.4 Control Strategy Based on Actuator Voltage Regulation

The well-known control schemes for BLDC motors include an inverter that uses the pulse-width modulation (PWM) technique to convert the input DC voltage into a modulated driving voltage [5, 48]. In Section 2.3, we presented a current regulation control scheme which optimizes the energy regeneration, and uses an inverter as the motor drive. The drawback of standard commutation approaches is that they limit the possibilities of optimizing energy consumption by direct control of the individual phases of the BLDC motor.

In this section, we introduce a novel driver for replacing the inverter. The new controller, henceforth called regenerative control unit (RCU), consists of three power conversion elements (PCE) as shown in Fig. 3. The method directly controls each phase of the motor by connecting it to one regenerative PCE which are typically used to command DC motors. To proceed constructing the RCU, we make two main assumptions: i. there are no external forces or moments applied to the robot manipulator; and ii. all JMs of the robot are of the *semi-active* kind. Here we assume that all semi-active joints are connected to a common ESE as illustrated in Fig. 17 (star configuration). Control inputs are applied to the RCU of each joint. This arrangement allows operation in the driving mode or the regenerative mode, according to the direction of power flow between the ESE and the robot link. In order to introduce the RCU, we first need to find the augmented model of the robot, JMs and BLDC motors. The models of the robot and JMs are introduced in Section 2.2. Forming the augmented model requires finding τ_{ind} in Eqn. (3.13), which is done in

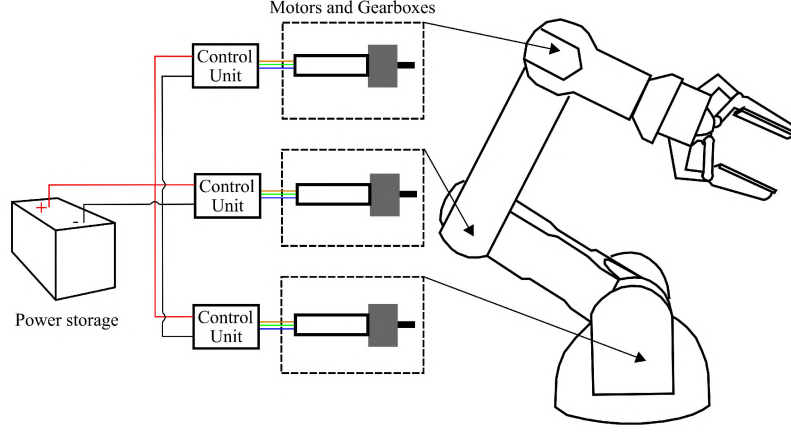


Figure 17: Illustration of semi-active joints connection to a single energy storage element.

the following section.

2.4.1 BLDC Motor Modeling

The BLDC motor has three phases, namely a, b, c , and thus three terminals. For the BLDC motor that is connected to the j th joint of the robot, we assume the three stator windings for the three phases are identical, with 120° (electrical) phase displacement among them. The voltage equations at the three motor terminals can be obtained from:

$$\mathbf{V}_j = \bar{\mathbf{R}}_j \mathbf{I}_j + \bar{\mathbf{L}}_j \frac{d}{dt}(\mathbf{I}_j) + \mathbf{e}_j \quad (2.28)$$

where:

$\mathbf{V}_j = [V_{a_j}, V_{b_j}, V_{c_j}]^T$ and V_{i_j} , $i \in \{a, b, c\}$ is the voltage of each motor's terminal.

$\bar{\mathbf{R}}_j = \text{diag}(R_j) \in \mathbb{R}^{3 \times 3}$ and R_j is the resistance of each phase winding.

$\mathbf{I}_j = [I_{a_j}, I_{b_j}, I_{c_j}]^T$ and I_{i_j} is the current in each phase.

$\bar{\mathbf{L}}_j = \text{diag}(L_j) \in \mathbb{R}^{3 \times 3}$ and L_j is the difference between the stator phase self-inductance and stator mutual inductance.

$\mathbf{e}_j = [e_{a_j}, e_{b_j}, e_{c_j}]^T$ and e_{i_j} is the back electromotive force (emf) in each phase [116, 2].

Note that the three phase windings are assumed identical, hence a single set of pa-

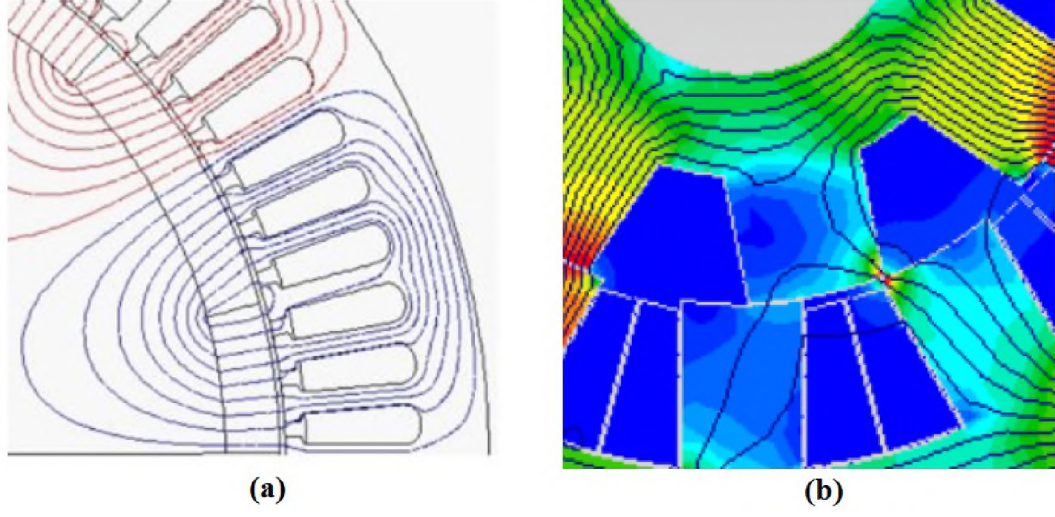


Figure 18: Flux density configuration. (a) Sinusoidal pattern flux between stator and rotor. (b) Trapezoidal pattern flux between stator and rotor.

rameters is used. Assuming small L_j (typical for BLDC motors used in robot drives), the voltage vector can be approximated as:

$$\mathbf{V}_j \approx \bar{\mathbf{R}}_j \mathbf{I}_j + \mathbf{e}_j \quad (2.29)$$

The back-emf voltage in each phase is generated as a result of rotation, and it is described by:

$$e_{ij} = \lambda_j f_{ij} \left(P\theta_{r_j}/2 \right) \omega_{r_j} \quad (2.30)$$

where λ_j is the back-emf constant, P is the number of poles in the motor, ω_{r_j} is the rotor's speed, and θ_{r_j} is the rotor's angle. $f_{ij}(\frac{P}{2}\theta_{r_j})$ defines the shape of the back-emf and the shape of the back-emf is determined by the flux density of the motor. Depending on how the motor is designed, the shape could be either trapezoidal or sinusoidal functions, as shown in Fig. 18 [116, 117, 118]. Henceforth, for simplicity, we drop the argument and use the notation f_{ij} for $f_{ij}(\frac{P}{2}\theta_{r_j})$.

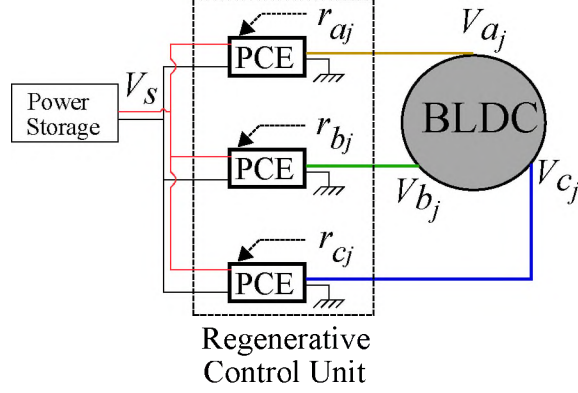


Figure 19: Schematic of the connection setup of j th BLDC motor, the RCU, and the ESE.

Finally, the induced torque of BLDC motor is [2, 21]:

$$\tau_{ind_j} = \lambda_j \mathbf{f}_j^T \mathbf{I}_j \quad (2.31)$$

where $\mathbf{f}_j = [f_{a_j}, f_{b_j}, f_{c_j}]^T$. By substituting the current from Eqn. (2.29) and the back-emf from Eqn. (2.30) into the Eqn. (2.31), the induced torque components become:

$$\tau_{ind_j} = \frac{\lambda_j}{R_j} \{ \mathbf{f}_j^T \mathbf{V}_j - \lambda_j \omega_{r_j} \mathbf{f}_j^T \mathbf{f}_j \} \quad (2.32)$$

All three terminals of the motor are connected to the RCU as shown in Fig. 19. The RCU as the motor driver, accepts command to control the motor according to the motion control objectives set forth for the robot, e.g. following a desired trajectory. Each phase of the BLDC motor is connected to a PCE that controls each phase independently. The PCE can control the amount and direction of the applied voltage to the phase by adjusting the ratio of the applied voltage over the voltage of the ESE. Therefore, for each phase, the voltage ratio $r_{i_j} = V_{i_j}/V_s$ is the command applied to the PCE. These ratios constitute the control inputs available for design.

Replacing the voltage vector with voltage ratio vector and $\omega_{r_j} = \eta_j \dot{q}_j$ into Eqn. (2.32), the induced torque can be rewritten as:

$$\tau_{ind_j} = \frac{\lambda_j V_s}{R_j} (\mathbf{f}_j^T \mathbf{r}_j) - \frac{\lambda_j^2 \eta_j \dot{q}_j}{R_j} (\mathbf{f}_j^T \mathbf{f}_j) \quad (2.33)$$

where $\mathbf{r}_j = [r_{a_j}, r_{b_j}, r_{c_j}]^T$ is the vector of voltage ratios. Replacing τ_{ind_j} from Eqn. (2.33) into Eqn. (2.2), combining the result with Eqn. (2.1), and absorbing the terms containing \ddot{q}_j and \dot{q}_j into the left-hand side, yields the following augmented robot-JM model:

$$M(q)\ddot{q} + C(q, \dot{q})\dot{q} + g(q) = \mathcal{T} \quad (2.34)$$

Comparing Eqn. (2.1) and Eqn. (2.34), the elements of M^o and M are the same except along the diagonal, where $M_{jj} = M_{jj}^o + m_j \eta_j^2$. Also C and C^o are only different in the diagonal terms such that:

$$C_{jj} = C_{jj}^o + b_j \eta_j^2 + \frac{\lambda_j^2 \eta_j^2}{R_j} (\mathbf{f}_j^T \mathbf{f}_j) \quad (2.35)$$

The components of $\mathcal{T} = [\mathcal{T}_1, \dots, \mathcal{T}_n]^T$ are:

$$\mathcal{T}_j = \frac{\lambda_j \eta_j V_s}{R_j} (\mathbf{f}_j^T \mathbf{r}_j) \quad (2.36)$$

2.4.2 Semi-active Virtual Control Strategy

According to Fig. 19, the only adjustable variable in the j th semi-active joint is \mathbf{r}_j . If a feedback law for the torques \mathcal{T}_j of the augmented model is given, the voltage ratios can be determined from Eqn. (2.36). To this end, we modify a method called semi-active virtual control (SVC) introduced in [4] to control semi-active JM connected to DC motors. The SVC concept is based on using any suitable feedback law for the torques of the augmented model presented in Eqn. (2.34). The desired torques are

then matched to the applied voltage ratios, using ESE voltage as feedback. The SVC methodology is extended for use with BLDC motors as follows:

1. A virtual control law, $\mathcal{T}^v = [\mathcal{T}_1^v, \dots, \mathcal{T}_n^v]^T \in \mathbb{R}^n$, is designed for \mathcal{T} in the augmented model of the system in Eqn. (2.34) based on the applicable specifications, such as tracking, stability, robustness, disturbance rejection and so forth.
2. To enforce the torques prescribed by \mathcal{T}^v and meet the control objectives, a solution for \mathbf{r}_j is sought that satisfies:

$$\mathcal{T}_j^v = \frac{\lambda_j \eta_j V_s}{R_j} (\mathbf{f}_j^T \mathbf{r}_j) \quad (2.37)$$

Note that this virtual control matching is possible as long as there is enough charge left in the ESE. Exact matching in Eqn. (2.37) will hold whenever the JM parameters are known precisely and $|r_{i_j}| \leq 1$. The latter condition comes from the fact that the PCE is non-boosting, i.e., it can apply voltage magnitudes not exceeding V_s . The modulation law for exact virtual matching is obtained by solving for the vector of \mathbf{r}_j from Eqn. (2.37). However, Eqn. (2.37) is underdetermined. Accordingly, two additional equations are needed. The second equality constraint is given by Kirchhoff's current law, which states that the sum of currents in the three phases is zero, i.e. $I_{a_j} + I_{b_j} + I_{c_j} = 0$ [21]. Using the currents from Eqn. (2.29) and with some manipulation, Eqn. (2.38) is obtained:

$$r_{a_j} + r_{b_j} + r_{c_j} = \frac{\lambda_j \eta_j \dot{q}_j}{V_s} (f_{a_j} + f_{b_j} + f_{c_j}) \quad (2.38)$$

Together, Eqns. (2.37) and (2.38) form the following equality constraints for j th semi-active joint:

$$A_{eqj} \mathbf{r}_j = B_{eqj} \quad (2.39)$$

where:

$$A_{eq_j} = \begin{bmatrix} f_{a_j} & f_{b_j} & f_{c_j} \\ 1 & 1 & 1 \end{bmatrix}, B_{eq_j} = \begin{bmatrix} \mathcal{T}_j^v R_j / (\lambda_j \eta_j V_s) \\ \lambda_j \eta_j \dot{q}_j (f_{a_j} + f_{b_j} + f_{c_j}) / V_s \end{bmatrix}$$

The equality constraints involve angular position, angular velocity, ESE voltage, and the virtual control torque, which are assumed to be available for feedback. However, the equality constraints are still underdetermined and can not be solved explicitly. Optimization based on the power exchange between the ESE and the BLDC motors will be used in the next sections to resolve control redundancy, with Eqn. (2.39) as an equality constraint. Specifically, an internal energy balance equation between the ESE and BLDC motors is obtained to define a cost function for optimization and final determination of $\mathbf{r} = [\mathbf{r}_1, \dots, \mathbf{r}_n]^T \in \mathbb{R}^{3n}$.

2.4.3 Internal and External Energy Balance

The internal energy balance describes the power exchange between the BLDC motors and the ESE, and it can be written as:

$$V_s I_s = \sum_{j=1}^n \mathbf{V}_j^T \mathbf{I}_j \quad (2.40)$$

where I_s is the current of the ESE. It is important to note that, even though Eqn. (2.40) describes an ideal power transmission, power losses exist in the PCEs. To capture the inefficiency, we can consider an internal resistance, δr , for each PCE. This resistance can be fit to input/output measurements of the PCE and then added to the series resistance R_j of the motor. In the other words, despite the inefficiency in the PCEs, Eqn. (2.40) can still be utilized, with δr added to the BLDC motor's phase resistance.

Dividing both sides of Eqn. (2.40) by V_s , substituting \mathbf{I}_j from Eqn. (2.29) into Eqn. (2.40), and using the voltage ratio variable, $\mathbf{V}_j = V_s \mathbf{r}_j$, and finally taking

the integral in an arbitrary interval $[t_1, t_2]$, the internal energy balance can be obtained after some algebra as:

$$\Delta E_s = \int_{t_1}^{t_2} \sum_{j=1}^n \frac{V_s}{R_j} (\mathbf{e}_j^T \mathbf{r}_j - V_s \mathbf{r}_j^T \mathbf{r}_j) dt \quad (2.41)$$

where ΔE_s is the electric energy change in the ESE. The internal energy balance in Eqn. (2.41) focuses on the electric energy variations of the ESE and does not reveal any information about the electrical-mechanical energy exchange in the system. An external energy balance for the whole system provides this information and can be derived as:

$$\Delta E_m^T + \Sigma_m^T + \Sigma_e + \Delta E_s = 0 \quad (2.42)$$

where ΔE_m^T and Σ_m^T are the total mechanical energy change and mechanical losses of the robot and the semi-active joints, respectively, Σ_e represents the Joule (resistance heating) losses of the semi-active joints and ΔE_s is the term related to the energy stored in the ESE defined in Eqn. (2.41). The derivation and definition of terms in Eqn. (2.42) are outlined in the appendix B.

The external energy balance is useful to map energy flows and conversions in the whole system, characterizing efficiency and losses. The internal energy balance equation is useful for optimization and finding \mathbf{r}_j , as explained in the following section.

2.4.4 Optimization Problem

In this research, we consider a primary motion control objective for the robot, such as following a desired trajectory. Optimization is used to meet this objective while minimizing energy consumption. We formulate this as an online maximization of instantaneous regenerative power under the equality constraints, given by Eqn. (2.39). This is equivalent to the maximum power transfer tracking (MPTT) approach used

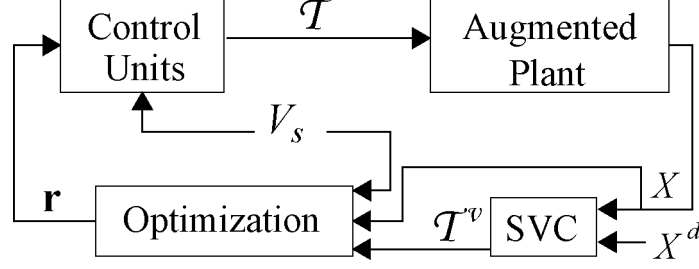


Figure 20: The structure of online control algorithm. $X = [q^T, \dot{q}^T]^T$ and $X^d = [(q^d)^T, (\dot{q}^d)^T]^T$ are the vectors of the actual and desired states, respectively.

in photovoltaic systems [119]. Here, we focus on tracking of a pre-designed trajectory in joint space given by some function $q^d(t)$. Considering the internal energy balance in Eqn. (2.41) together with the equality constraints in Eqn. (2.39) and the inequality constraints $|r_{ij}| \leq 1$, the following nonlinear optimization problem is formulated:

$$\max_{\mathbf{r}} \delta E_s = \bar{\mathbf{e}}^T \mathbf{r} - \mathbf{r}^T \bar{V}_R \mathbf{r} \quad (2.43a)$$

$$\text{such that: } \begin{cases} A_{eq} \mathbf{r} = B_{eq} \\ |\mathbf{r}| \leq \mathbf{1} \end{cases} \quad (2.43b)$$

where $\bar{\mathbf{e}} = V_s [\frac{e_1^T}{R_1}, \dots, \frac{e_n^T}{R_n}]^T \in \mathbb{R}^{3n}$, $\bar{V}_R = \text{diag}(\bar{V}_{R_j}) \in \mathbb{R}^{3n \times 3n}$, $\bar{V}_{R_j} = (V_s^2 / R_j) I_{3 \times 3}$, $A_{eq} = \text{diag}(A_{eq_j}) \in \mathbb{R}^{2n \times 3n}$, and $B_{eq} = [B_{eq_1}^T, \dots, B_{eq_n}^T]^T \in \mathbb{R}^{2n}$. A_{eq_j} and B_{eq_j} are defined in Eqn. (2.39) and $\mathbf{1} \in \mathbb{R}^{3n}$ denotes a vector of ones. The optimization aims to maximize, δE_s which means reducing the amount of energy draw from ESE, or even recharging it through regeneration when possible. A value of $\delta E_s > 0$ indicates energy regeneration and $\delta E_s < 0$ indicates energy consumption. The optimization problem is quadratic in \mathbf{r} and the constraints are linear, therefore it can be efficiently solved online. The structure of online control algorithm is shown in Fig. 20. Note that δE_s is the time derivate of ΔE_s in Eqn. (2.42). Maximizing the gradient of the $\Delta E_s(t)$ is equivalent to increase energy regeneration. Moreover, by maximizing δE_s , we do not need to define any time horizon for the optimization.

To design the virtual control (\mathcal{T}^v), any feedback control law compatible with the desired motion control objectives can be selected. Any properties that apply to the virtual design such as stability, tracking performance, robustness, etc. will be propagated to the actual system as long as virtual matching holds precisely, i.e. $\mathcal{T} = \mathcal{T}^v$ [4]. Exact virtual matching in this case will be obtained provided there is accurate knowledge of λ_j, η_j and R_j , since r_j is maintained in $[-1, 1]$ by the optimization algorithm and PCE saturation is prevented.

The saturation problem also may occur by the motion task objective. That is, the trajectory tracking demands an amount of torque which can not be provided by the maximum available voltage. In this case, the saturation can be avoided simply by increasing the voltage of ESE.

2.4.5 Experimental Setup

Two experiments were conducted to assess the optimization problem and the performance of proposed RCU shown in Fig. 19. To this end, we tested the developed driver using two different BLDC motors. Each motor drives a pendulum which is compatible with the motor's characteristics and power. It should be noted that the reason to use two motors is to ensure that the developed RCU can run various BLDC motors. In both experiments, each phase of the motor is driven by a four-quadrant, 25 A SyRen motor driver (Dimension Engineering, Hudson, Ohio) (Fig. 21). The input of all three motor drivers are connected to a common 24 V ultracapacitor (Maxwell Technologies, San Diego, California) (Fig. 22) with a capacitance of 165 F. The MicroLabBox (dSPACE GmbH, Paderborn, Germany) (Fig. 23) is used for all real-time calculations such as: determining the SVC, solving the optimization problem, applying voltage (control) to motor drives, and data acquisition, monitoring and logging. The MicroLabBox is supported by the dSPACE RTI 1202 real-time interface for Simulink.

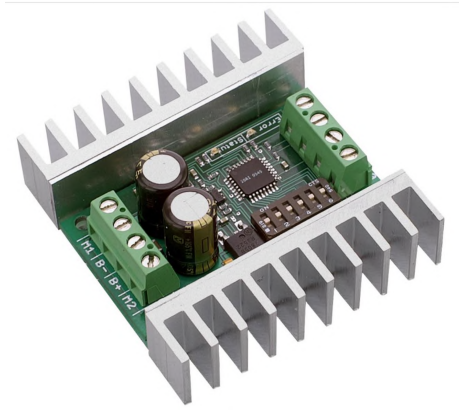


Figure 21: Dimension Engineering SyRen 25A 6V-24V Regenerative Motor Driver.



Figure 22: Maxwell Technologies, Ultracapacitor Module.



Figure 23: dSPACE MicroLabBox.

Table III: Pendulum and BLDC motor parameters (Experimental setup I).

Parameter	Value	Unit
<u>Pendulum:</u>		
Length	0.337	m
Mass	0.35	kg
<u>BLDC motor:</u>		
Gear ratio	33	-
Resistance of each phase	0.695	Ω
Back emf const. of each phase	0.0205	volt/rad/s

In the first experiment, the possibility of practical implementation of the RCU is validated. In the second experiment, we are seeking for two objectives; validation of RCU with another BLDC motor, and comparing the energy consumption against an off-the-shelf motor driver. In the following sections, both experiments and their results are explained.

Experimental Setup I

In the first experiment, the setup of the test is according to Fig 24. An 80-Watt Maxon (Maxon motor, Switzerland) BLDC gearmotor is used to drive the pendulum. To calculate the current in each phase, an ACS723 current sensor (Allegro Microsystems, Worcester, Massachussetts) is used. An optical encoder, connected to the shaft of the motor, measures the rotation angle and the angular velocity is calculated by a differentiator filter transfer function. In this experiment, the objective is for the rotation angle to follow a sinusoidal desired trajectory. The PD controller is chosen for the virtual torque, τ^v , to track the desired trajectory. It should be noticed that the PD controller is chosen for the sake of simplicity. However, any suitable controller which is compatible with the motion task can be used, no matter how advanced or complex. The parameters of the motor and the pendulum are shown in Table III.

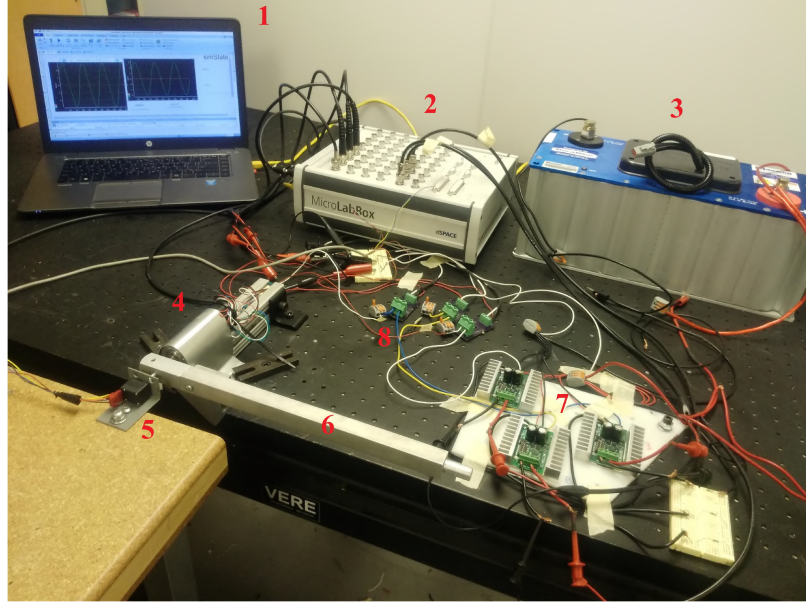


Figure 24: Laboratory experimental setup I. (1) Data monitoring, (2) MicroLabBox controller, (3) Ultracapacitor, (4) BLDC motor, (5) Optical encoder, (6) Pendulum, (7) Three motor drivers, (8) Three current sensors

Results for Experiment I

The quadratic objective function in Eqn. (2.43) can be readily minimized, using any online-implementable solver. Here we utilized *Matlab*'s `mpcqp solver`¹ which is an online quadratic programming solver. The schematic of online control process is depicted in Fig. 20. The voltage of the ultracapacitor is measured and fed back to update the bounds on \mathbf{r} during optimization in Eqn. (2.43). The virtual control output, τ^v , is used in the equality constraint in Eqn. (2.43 b), which also needs real-time capacitor voltage feedback. The data, plots and analysis presented in this section correspond to the steady oscillation regime achieved by the control system.

In Fig. 25, the actual and desired angles and the joint angular velocities of the pendulum are depicted, showing achievement of the tracking objective. The small tracking error is attributed to the use of PID as virtual control for the sake of

¹Description of the function can be found in <https://www.mathworks.com/help/mpc/ref/mpcqp solver.html>

demonstration. More advanced, model-based control methods should achieve smaller tracking errors.

The applied phase voltages are shown in Fig. 26. For clarity, the applied voltages to three phases are only shown during a small time period. The shift of applied voltage is obvious in this figure. It is worth mentioning that the magnitude of applied voltage in each phase depends on the applied torque by the motor, hence it depends on the desired trajectory. For various trajectories, the magnitude of voltage may be different in each phase.

Figure 27 shows the power flow for three phases of the motor. Note that the positive power indicates an energy flow from the ultracapacitor to the motor drive (energy consumption) and negative power indicates energy flowing from a phase to the ultracapacitor (energy regeneration). To study the effect of power flow direction, i.e. consumption or regeneration, we compare the net power sign and the ultracapacitor voltage change as shown in Fig. 28. The net power of the three phases is shown in Fig. 28(a), the ultracapacitor voltage is shown in Fig. 28(b), and the pendulum angle is shown in Fig. 28(c). For ease of comparison, polynomials are fitted to both the power and the voltage. Whenever the total net power is negative (under zero level line), the voltage is increasing and vice versa. For instance, when $3.0 \leq t \leq 3.8$, the voltage is increasing which shows energy regeneration during this period. We can also relate the system joint coordinate to energy regeneration. The non-regenerative (NR) and regenerative (R) phases of pendulum trajectory are marked by red and green color, respectively in Fig. 28(c). During the NR phase ($2.3 \leq t \leq 3.0$), there is no energy regeneration. This phase starts from minimum potential energy level of the system ($q = 0$) and continues until the potential energy of the system reaches its maximum level ($|q| = 3$ [rad]). The R phase ($3 \leq t \leq 3.8$) starts from maximum potential energy level and ends when the pendulum reaches its minimum potential.

Figure 29 shows the time history of the ultracapacitor charge. Overall, the capacitor has a slow discharging trend, but there are periods of time where the capacitor is being charged through regeneration as discussed before.

Figure 30 shows Sankey diagrams for the overall energy balance based on Eqn. (2.42). Energy can be stored in the ultracapacitor only due to changes in mechanical energy. In Fig. 30(a), the Sankey diagram is depicted for NR phase of Fig. 28(c). In this phase, the pendulum gains potential energy and its total mechanical energy (ΔE_m^T) increases. The energy needed for this phase comes from the ultracapacitor. In Fig. 30(b), the Sankey diagram is depicted for R phase of Fig. 28(c). The total mechanical energy decreases and the lost energy is converted to electric form and either dissipated (Σ_e and Σ_m^T) or stored in ultracapacitor (ΔE_c).

To conclude the study of first experiment, we define the effectiveness of energy regeneration as:

$$\epsilon = 1 - \frac{\Delta E_R}{\Delta E_{NR}} \quad (2.44)$$

where ΔE_R and ΔE_{NR} are the system energy consumption with and without energy regeneration, respectively [34]. ΔE_{NR} is computed by integrating the power flows in three phases of the motor, assuming all negative power is dissipated (i.e. $P_i (P_i \leq 0) = 0$, $i \in \{a, b, c\}$). We have $0 \leq \epsilon \leq 1$ where $\epsilon = 0$ means energy regeneration has zero effect in reducing the energy consumption and $\epsilon = 1$ indicates that energy regeneration achieves the maximum possible reduction in energy consumption. In an experiment of 78.5 sec. (20 complete cycles), $\Delta E_R = 18.47 \text{ J}$ and $\Delta E_{NR} = 32.12 \text{ J}$ which results in $\epsilon = 0.42$. This shows approximately 40% reduction in energy consumption due to energy regeneration.

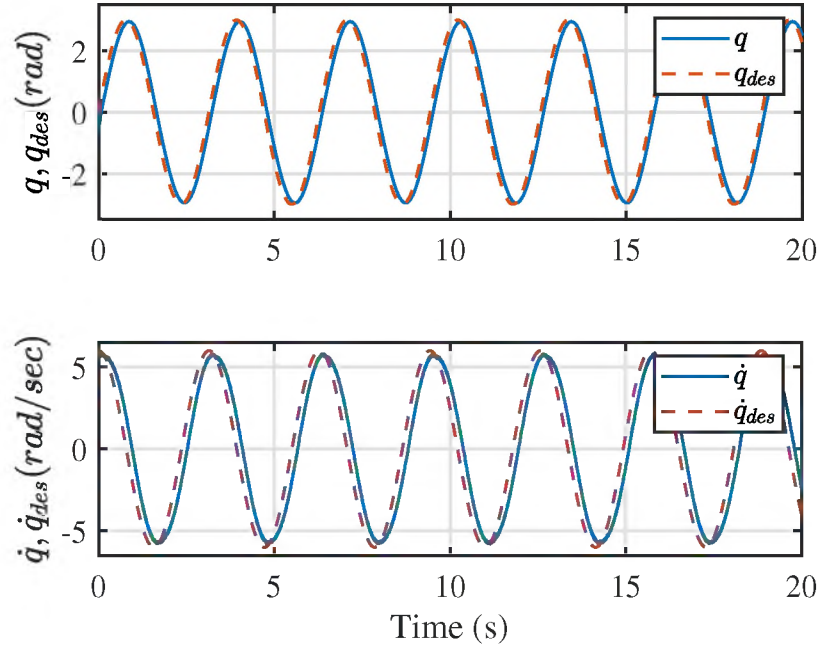


Figure 25: Pendulum angle and angular velocity, tracking desired trajectory ($q_{des} = 3 \sin(2t)$).

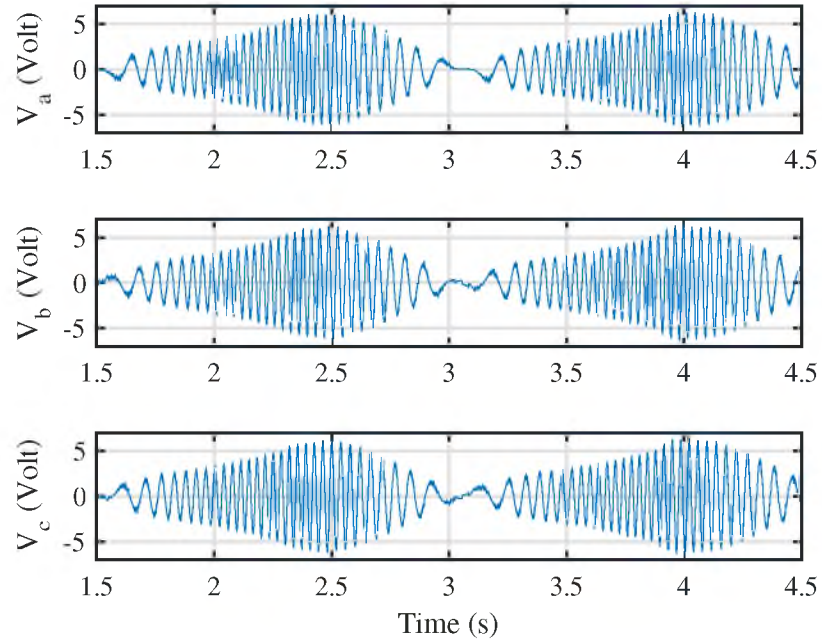


Figure 26: Applied voltage to each phase of the motor.

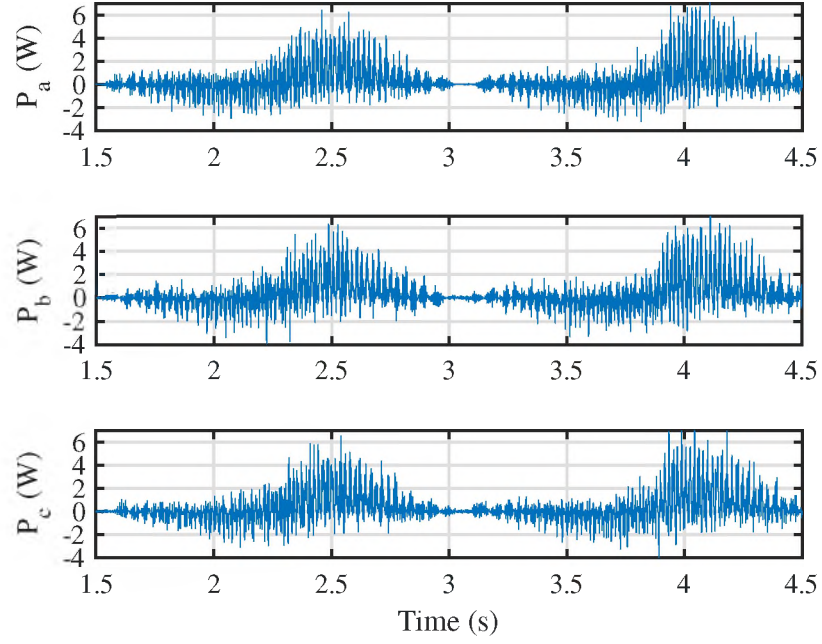


Figure 27: Power flows for each phase of the motor.

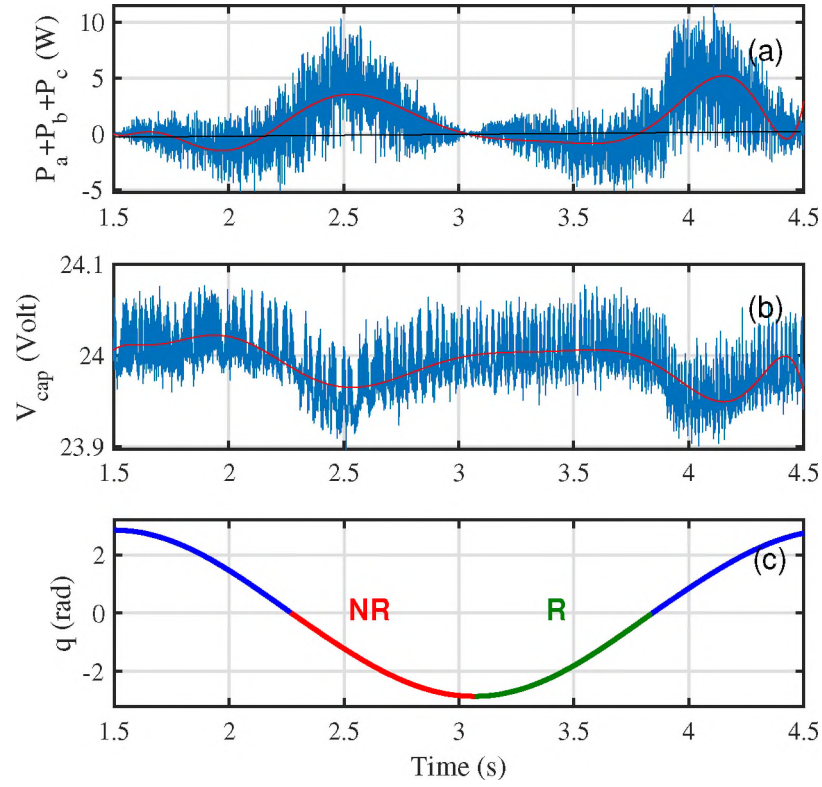


Figure 28: (a) sum of powers in three phases. (b) voltage of ultracapacitor. (c) pendulum angle. The red lines in (a-b) show the fitted polynomial curve to the net power and the voltage. The black line in (a) shows the zero level.

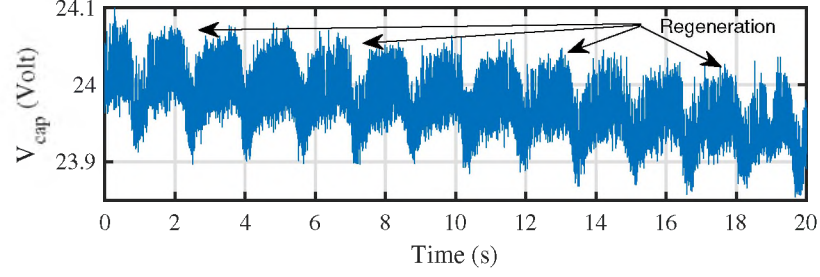


Figure 29: Ultracapacitor voltage. The peaks indicate the times when regeneration happens.

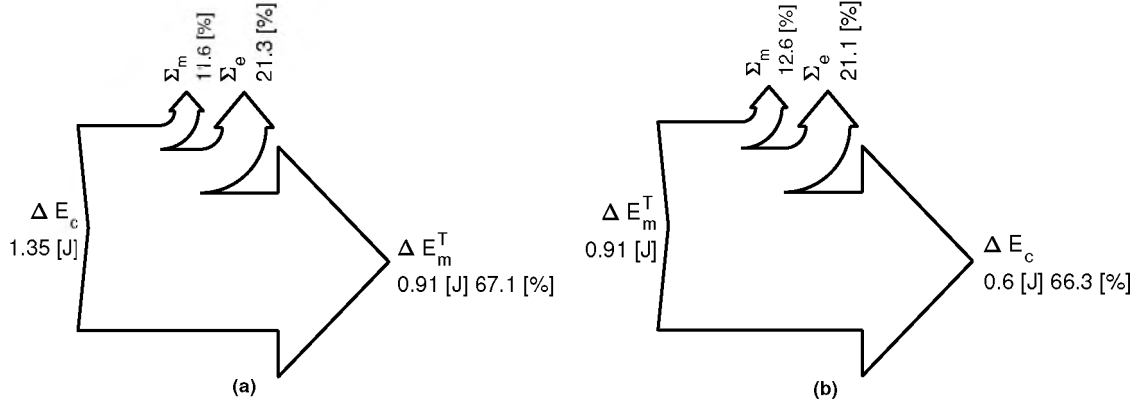


Figure 30: Sankey diagram showing the energy balance for the pendulum when following the desired trajectory. (a) The energy balance during non-regenerative (NR) phase. (b) The energy balance during regenerative (R) phase.

Experimental Setup II

In the second experiment, we used a pendulum with a mass attached at the tip. To study the effectiveness of the RCU in comparison to an off-the-shelf regenerative BLDC motor drive, an experiment on trajectory following was repeated with both drivers. To drive the pendulum, An 92-Watt Anaheim (Anaheim Automation, Inc., USA) BLDC gearmotor was used. The parameters of the pendulum and motor are shown in Table IV.

For the proposed RCU, henceforth named RCUa, each phase of the motor is driven by a four-quadrant, SyRen25 motor driver. These devices play the role of PCEs and provide a good approximation to Eqn. 2.40. The current on the ultracapacitor side was measured with an ACS712 current sensor (Allegro Microsystems, Worcester, Massachussetts). The power supply inputs of the 3 Syren25 drivers are connected in parallel to the ultracapacitor. The motor is equipped with optical encoder and hall-effect sensors. The encoder, connected to the shaft of the motor, measures the rotation angle and the angular velocity is calculated by a differentiator filter transfer function.

For the standard regenerative off-the-shelf motor driver, henceforth named RCUb, a BE12 brushless PWM servo amplifier (Advanced Motion Controls, USA)

Table IV: Pendulum and BLDC motor parameters (Experimental setup II).

Parameter	Value	Unit
<u>Pendulum:</u>		
Length	0.42	m
Mass of the bar	0.32	kg
Mass of the end weight	0.2	kg
<u>BLDC motor:</u>		
Gear ratio	7.5	-
Resistance of each phase	0.32	Ω
Back emf const. of each phase	0.0458	volt/rad/s
Number of poles	4	-

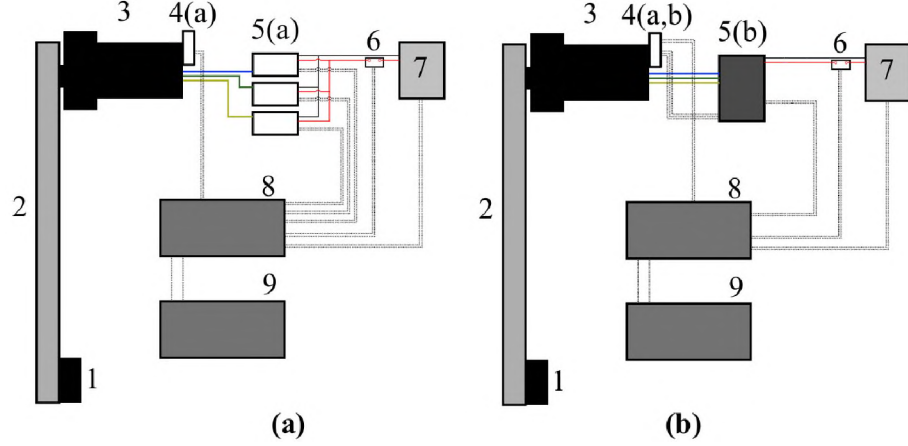


Figure 31: Schematic of laboratory setup. (a) The developed motor driver, (b) The standard off-the-shelf driver. Wires that transfer charge are shown with solid line and wires which transfer data are shown with dotted line. 1: Mass at the tip, 2: The pendulum, 3: The Anaheim BLDC motor and gearbox, 4(a): Optical encoder, 4(b): The hall-effect sensor, 5(a): SyRen motor drives, 5(b): Brushless PWM servo amplifier 6: ACS712 current sensor, 7: The Maxwell ultracapacitor, 8: The MicroLabBox, 9: The computer

was selected. The same ultracapacitor and current sensor are used for the setup. The schematic of laboratory setups, for both motor drivers, are shown in Fig. 31. The lab setup for RCUa is shown in Fig. 32. For RCUa, angle and angular velocity feedback were used for the virtual control law. The objective was to follow a sinusoidal desired trajectory, for which a simple PD law was used as illustration. After finding \mathcal{T}^v , the virtual command is passed to the optimization block together with position, velocity and ultracapacitor voltage feedback. Similar to the first experiment, the quadratic objective function in Eqn. (2.43) is solved by *Matlab*'s `mpcqp solver`.

For RCUb, in order to command the motor driver, we need to find the motor driver and BLDC motor gain, i.e. the relationship between the generated torque of the motor and the command voltage to the motor driver. By running an experiment of measuring the applied command voltage in motor driver versus the generated torque of the motor, it can be shown that the following relation is true:

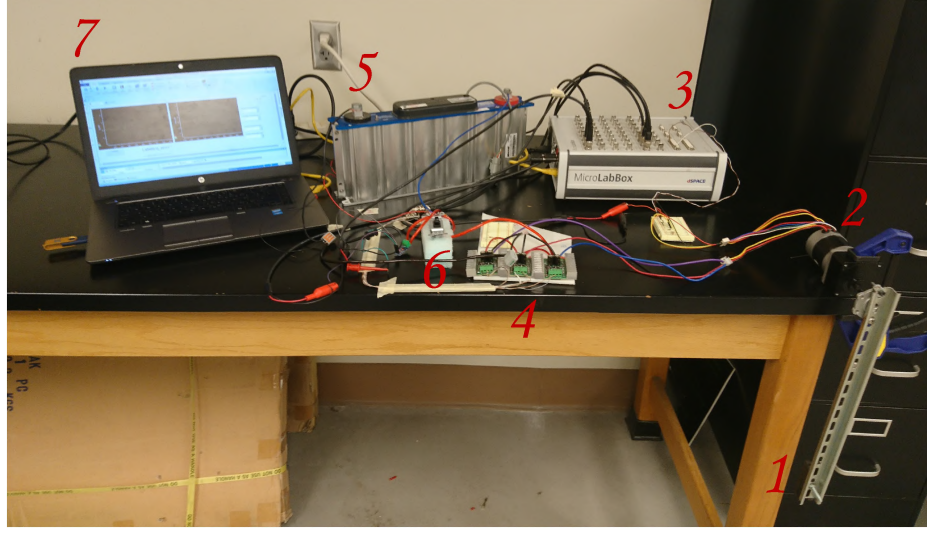


Figure 32: Laboratory experimental setup (1) Pendulum, (2) BLDC motor, gearbox, and optical/hall sensors, (3) MicroLabBox controller, (4) RCUa, (5) ultracapacitor, (6) Current sensor, (7) Data monitoring.

$$\mathcal{T} = KV_{in} \quad (2.45)$$

where \mathcal{T} is the generated motor's torque, K is a constant gain, and V_{in} is the applied command voltage from the dSPACE to the motor driver². Assuming $\mathcal{T} = \mathcal{T}^v$, after using a virtual controller to generate \mathcal{T}^v , the command voltage can be obtained from $V_{in} = \mathcal{T}^v/K$. Note that Eqn. (2.45) is running in closed-loop. \mathcal{T} is obtained and designed using feedback information.

Results for Experiment II

For the trajectory following and comparison between RCUa and RCUb, the motion task for the pendulum is to follow a sinusoidal desired trajectory. Both controllers use a PD control as the virtual controller. The data, plots and analysis presented in this section correspond to the steady oscillation regime achieved by the control systems.

Figure 33 shows the time histories of the reference trajectory and the actual

²The linear relation is obtained based on the specific motor and motor driver that were used in the experiment.

Table V: Tracking accuracy and energy consumption comparison.

Control method	RCUa	RCUb
RMS of tracking error [rad]	0.0676	0.1012
Capacitor voltage-time Slope [V/s]	-7.751e-4	-1.1033e-3
Total withdrawn energy [J]	977.6	1222.1

angles obtained with RCUa and RCUb. The tracking objective is accurately achieved with both controllers. The small tracking error is attributed to the use of PD as virtual control for the sake of demonstration. The RMS values of the tracking error are reported in Table V. It should be noticed that the virtual controllers were tuned such that the best performance in accuracy was achieved in each case. The virtual controls are shown in Fig.34. The range of virtual control effort is directly related to the accuracy of trajectory following. The RCUa method creates a virtual control which is slightly higher in magnitude than virtual control of RCUb.

For energy consumption comparisons, the ultracapacitor voltage is measured while tracking the trajectory for five minutes. The change in ultracapacitor voltage is shown in Fig. 35. This voltage change is indicative of the stored energy change of Eqn. 2.41. To better evaluate compare discharge rates, a linear fit is applied to a segment of the data, and the slopes are reported in Table V. The amount of withdrawn energy from the ultracapacitor is reported in Table V.

To study power flow direction, i.e. energy consumption or regeneration, we compare the sign of the net power and the ultracapacitor voltage change for pendulum movements from $q = 0$ (minimum potential energy) to $q = \pi$ (maximum potential energy). The net power from/to the ultracapacitor, the ultracapacitor voltage, and the pendulum angle are shown in Fig. 36. Polynomials have been fitted to the power and voltage curves to remove noise and observe the relevant trends. It can be concluded from the plots that for $q : 0 \rightarrow \pi$, the power is positive and pendulum consumes energy to reach the highest level of potential. For $q : \pi \rightarrow 0$, power is negative. That

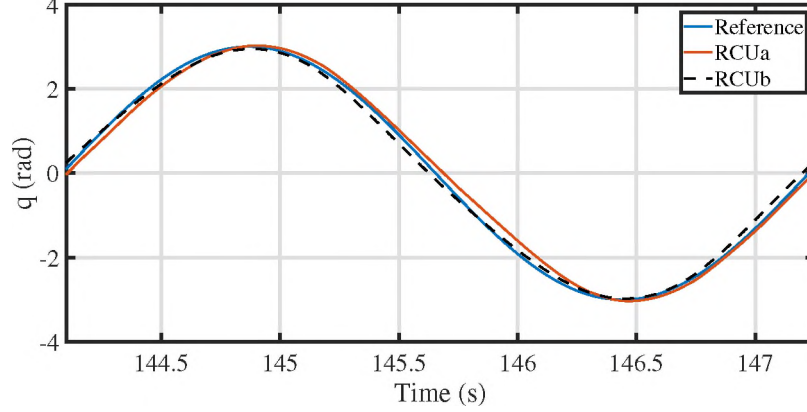


Figure 33: Pendulum angle time history, tracking desired trajectory of $q_{ref} = 3 \sin(2t)$. For clarity, the figure is depicted for a small-time period.

is, energy flows back and is partially stored in the ultracapacitor, showing a voltage increase. The regenerative phase is marked with green in Fig. 36.

The same plot is depicted for RCUb in Fig. 37. Overall, the same trend as in Fig. 36 can be detected. However, the power consumption peak is higher in comparison to RCUa and the voltage increase is negligible. It is shown in Table V that in terms of energy consumption, RCUa has privilege compare to RCUb.

Figure 38 shows the Sankey diagrams for the overall energy balance based on Eqn. (2.42). Energy can be stored in the ultracapacitor only due to changes in mechanical energy. In Fig. 38(a), the Sankey diagram is depicted for Non-regenerative (NR) phase of Fig. 36(c). In this phase, the pendulum gains potential energy and its total mechanical energy (ΔE_m^T) increases. The energy needed for this phase comes from the ultracapacitor. In Fig. 38(b), the Sankey diagram is depicted for Regenerative (R) phase of Fig. 36(c). The total mechanical energy decreases and the lost energy is converted to electric form and either dissipated (Σ_e and Σ_m^T) or stored in ultracapacitor (ΔE_c).

To conclude the results in this part, we recall the measure of energy regeneration effectiveness in Eqn. (2.44). In an experiment of five minutes using RCUa,

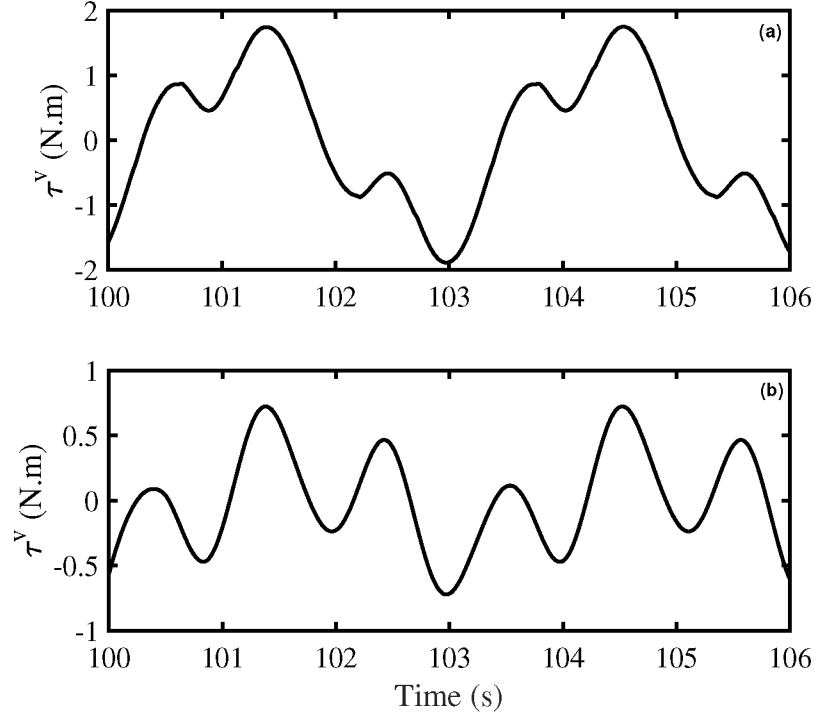


Figure 34: The generated virtual control (a) RCUa, (b) RCUb.

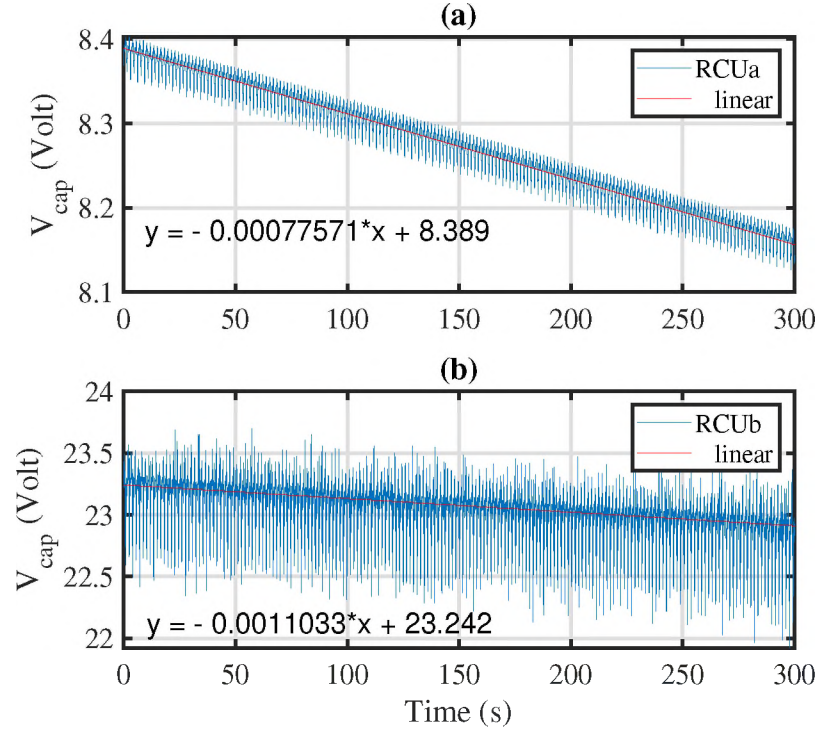


Figure 35: Time history of ultracapacitor voltage. (a) Voltage change for RCUa, (b) Voltage change for RCUb. In both plots, a linear curve is fitted to the data.

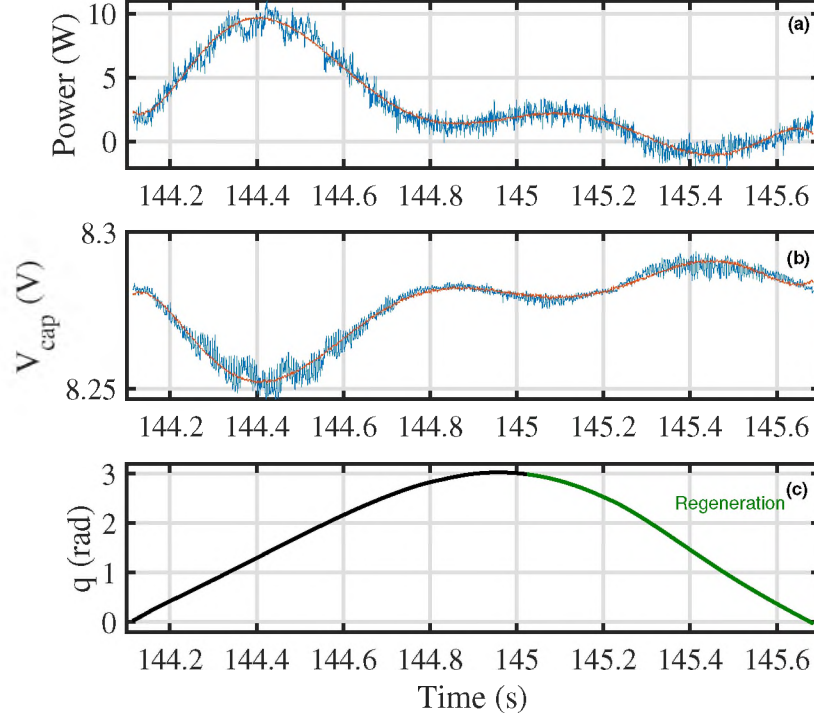


Figure 36: RCUa - (a) Net power in ultracapacitor terminal. (b) voltage of ultracapacitor. (c) pendulum angle. The red lines in (a-b) show the fitted polynomial curve.

$\Delta E_R = 977 \text{ J}$ and $\Delta E_{NR} = 1154 \text{ J}$ results in $\epsilon = 0.15$. This shows approximately 15% reduction in energy consumption due to energy regeneration.

2.4.6 Concluding remarks

In this study, a novel regenerative motor driver was introduced, successfully implemented and tested to drive two different BLDC motors. A comparison between the new motor driver and an off-the-shelf motor driver showed the advantage of the former motor driver in terms of energy regeneration.

The approach to introduce an augmented dynamics model of robot, JMs and the BLDC motors, provides the opportunity to introduce a new control scheme for semi-active joints called virtual control strategy. The proposed motor driver has the potential to be improved as an off-the-shelf controller and utilized where energy

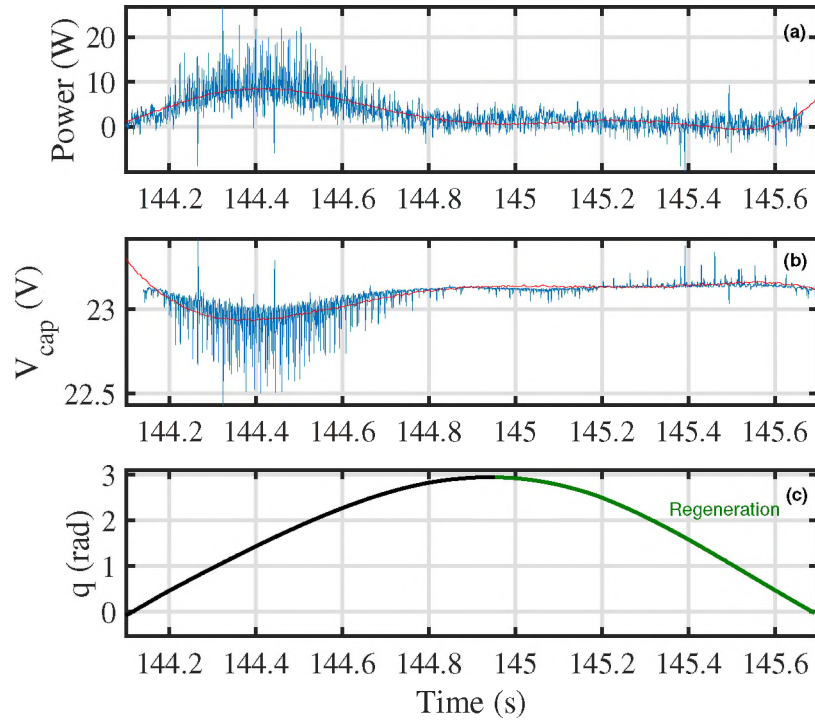


Figure 37: RCUB - (a) Net power in ultracapacitor terminal. (b) voltage of ultracapacitor. (c) pendulum angle. The red lines in (a-b) show the fitted polynomial curve.

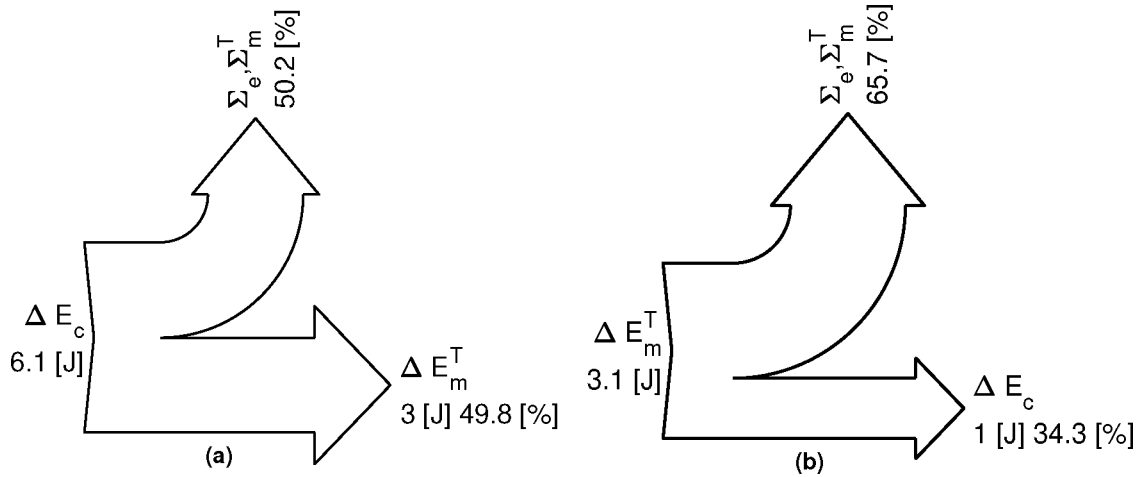


Figure 38: Sankey diagram showing the energy balance for the pendulum when following the desired trajectory. (a) The energy balance during non-regenerative phase. (b) The energy balance during regenerative phase.

saving is a concern. At this stage of research, the proof-of-concept is completed.

Finally, it is important to note that the optimization in Eqn. (2.43) depends on the virtual control, which in turn depends on a pre-designed desired trajectory that may not be the best for energy regeneration. It is possible to extend the optimization problem to search for the optimal trajectories, i.e., $q(t), \dot{q}(t), \ddot{q}(t)$, the optimal virtual control, \mathcal{T}^v , and the optimal voltage ratios, simultaneously. The new optimization problem finds the optimal trajectory of the joint coordinates between arbitrary initial and final points at some specified time. To formulate the new optimization problem, if we substitute equality constraint of Eqn. (3.26) in Eqn. (2.41), with some manipulation and simplification, the following optimization problem can be obtained:

$$\max_{q, \mathcal{T}^v, \mathbf{r}} \Delta E_s = \int_{t_1}^{t_2} (\mathcal{T}^v \dot{q} - \mathbf{r}^T \bar{V}_R \mathbf{r}) dt \quad (2.46a)$$

$$\text{such that: } \begin{cases} M(q)\ddot{q} + C(q, \dot{q})\dot{q} + g(q) = \mathcal{T}^v \\ A\mathbf{r} = B \\ |\mathbf{r}| \leq 1 \\ q_{t=0} = q_0, \dot{q}_{t=0} = \dot{q}_0 \\ q_{t=f} = q_f, \dot{q}_{t=f} = \dot{q}_f \end{cases} \quad (2.46b)$$

where $A = I_{n \times n} \otimes [1, 1, 1] \in \mathbb{R}^{n \times 3n}$ (\otimes is the Kronecker product), $B = [B_1, \dots, B_n]^T \in \mathbb{R}^n$, and $B_j = (\lambda_j \eta_j \dot{q}_j / V_s)(f_{a_j} + f_{b_j} + f_{c_j})$. The optimal trajectory starts from the initial condition, i.e. (q_0, \dot{q}_0) , and reaches the final condition, i.e. (q_f, \dot{q}_f) , and it is being subjected to two equalities; the augmented dynamic equations in Eqn. (2.34), and the equality obtained from Eqn. (2.38).

The optimization problem in Eqn. (2.46) is no longer a quadratic program

and the solution demands more computational effort. Also, it yields an open-loop control solution. A separate controller would be required to track this trajectory, as in [34], or a model predictive control scheme could be implemented.

CHAPTER III

ENERGY-ORIENTED MODELING AND CONTROL OF COOPERATIVE ROBOT MANIPULATORS

3.1 Introduction

So far, most research and development has been concerned with utilizing single manipulators, and much progress has been made in this direction. However, much attention has been devoted to the use of multiple robots for tasks which are impossible for single robot. Here, we define cooperative robot manipulators (CRM) as multiple robots which are employed for the manipulation of a common object in a cooperative manner. Using multiple robots can have a significant advantage over a single robot. Examples are robotic hands [30], multiple-armed devices [81], object assembly in space [120], etc.

In this chapter, we consider theoretical developments and extensions of a framework previously established for a single robot in [4]. Here, a motion task is defined as carrying a payload near a desired trajectory by grasping it using the CRM, limiting grasping forces and reducing energy consumption. The motion task thus demands a controller which meets the following objectives: 1) Maintaining acceptable track accuracy of desired trajectories for the position and orientation of the load, 2) being in compliance with the closed kinematic chain caused by grasping the load,

and 3) minimizing energy consumption through energy regeneration. A novel controller is proposed based on an impedance relation whose parameters are tuned such that maximum energy regeneration is provided. It is assumed that all robots and their corresponding actuators (DC motors) are equipped with regenerative drives (4-quadrant drives), allowing energy to go back from the robots to the storage element. Regenerative drives provide an opportunity to harvest the excess mechanical energy by channeling it back to the source instead of being dissipated [3].

In this work, we use energy consumption criteria to tune the parameters of the control signal. It worth mentioning that the problem of energy-oriented control in CRM has received less attention [30, 70, 57]. In these works, a quadratic function of the control signal is used as the representation of energy consumption. Considering the utilization of an ESE as the power source in our work, it will be shown that the quadratic function of the control signal does not represent the energy consumption.

An important part of developing a controller for dynamical systems is studying the stability of close-loop system. The controller stability is studied using the passivity theorem. Therefore, the first part of our study is devoted to the mathematical preliminaries needed for studying the passivity of the CRM.

3.2 Notation and Mathematical Preliminaries

In this section, we briefly recall some basic properties and classical results of input-output stability and passive systems [121, 122]. Denote \mathbb{R}_+ as the set of non-negative real numbers, and let \mathbb{R}^n be the n -dimensional vector space over \mathbb{R} . Define Π as the set of all measurable, real-valued, n -dimensional functions of time $f(t) : \mathbb{R}_+ \rightarrow \mathbb{R}^n$

and $t \in \mathbb{R}_+$ and define the sets:

$$\mathcal{L}_2^n \triangleq \{x \in \Pi \mid \|f\|_2^2 \triangleq \int_0^\infty \|f(t)\|^2 dt < \infty\} \quad (3.1a)$$

$$\mathcal{L}_\infty^n \triangleq \{x \in \Pi \mid \|f\|_\infty^2 \triangleq \sup_t \|f(t)\|^2 < \infty\} \quad (3.1b)$$

with $\|\cdot\|$ the standard Euclidean norm. Also, extended spaces are defined as:

$$\mathcal{L}_{2e}^n \triangleq \{x \in \Pi \mid \|f\|_{2,T}^2 \triangleq \int_0^T \|f(t)\|^2 dt < \infty, \forall T \in \mathbb{R}_+\} \quad (3.2a)$$

$$\mathcal{L}_{\infty e}^n \triangleq \{x \in \Pi \mid \|f\|_{\infty,T}^2 \triangleq \sup_T \|f(T)\|^2 < \infty, \forall T \in \mathbb{R}_+\} \quad (3.2b)$$

Here, \mathcal{L}_2^n and \mathcal{L}_{2e}^n are inner product spaces. The truncated inner product of two functions $u(t), y(t) \in \mathcal{L}_{2e}^n$ is defined as:

$$\langle y|u \rangle_T \triangleq \int_0^T u^T(t)y(t)dt \quad (3.3)$$

where the two functions can be related by a dynamical operator, H , such that $y = H(u)$. The operator H is called causal if the value of output, y , at time t is a function of the value of input, u , up to time t [122]. In other word, a casual (realizable) system cannot recognize future. That is, we cannot predict the future of a signal and use it for analysis in the system. So, basically a difference (differential) equation which does not have any terms including a future sample makes itself a causal system while the others are non-causal. Non-causal signal processing is possible from recorded data, and it cannot be realized in hardware. Only causal systems can be realized in hardware. For a causal operator, we have the following definitions:

Definition III.1 *Let $H : \mathcal{L}_{2e}^n \rightarrow \mathcal{L}_{2e}^n$ be a causal dynamic operator and $y = H(u)$ is the output. Then for some non-negative constants β, ϵ and δ , and $\forall u \in \mathcal{L}_{2e}^n$, $H(\cdot)$ is*

called *Input-Output Strict Passive (IOSP)* if:

$$\langle y|u \rangle_T \geq \epsilon \|u\|_{2,T}^2 + \delta \|y\|_{2,T}^2 - \beta \quad (3.4)$$

H is called *passive* if $\epsilon = \delta = 0$, *output strictly passive (OSP)* if $\epsilon = 0$, and *input strictly passive (ISP)* if $\delta = 0$ [122].

Definition III.2 The causal dynamical operator $H : \mathcal{L}_{2e}^n \rightarrow \mathcal{L}_{2e}^n$ is said to be *finite-gain \mathcal{L}_2 stable* if there are non-negative constants γ_0 and β_0 such that [123, 122]:

$$\|y\|_{2,T} \leq \gamma_0 \|u\|_{2,T} + \beta_0 \quad \forall T \geq 0 \quad (3.5)$$

3.2.1 Passivity in Feedback Systems

So far, we have defined the concept of input-output stability for a single causal system. The results can be extended for the feedback system as shown in Fig. 39. Here we assume the feedback interconnection is well-defined. That is for $r \triangleq (r_1, r_2)$ and $y \triangleq (y_1, y_2)$, the mapping $y = \tilde{H}(r)$ is causal and $\tilde{H} : \mathcal{L}_{2e}^n \rightarrow \mathcal{L}_{2e}^n$. We elaborate the following result for the feedback interconnection:

Lemma 1 Consider the well-defined feedback interconnection of two IOSP causal operator dynamical systems H_1 and H_2 as shown in Fig. 39. The following inequality is effective:

$$c_1 \|y_1\|_{2,T}^2 + c_2 \|y_2\|_{2,T}^2 \leq c_3 \|r_1\|_{2,T}^2 + c_4 \|r_2\|_{2,T}^2 - \hat{\beta} \quad (3.6)$$

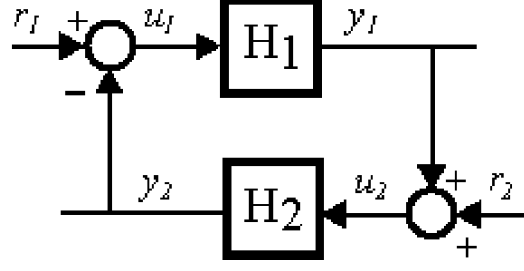


Figure 39: Feedback interconnection with two external inputs.

where:

$$c_1 = \{(\delta_1 + \epsilon_2) - \frac{\gamma_1}{2} - \epsilon_2 \gamma_4\}$$

$$c_2 = \{(\delta_2 + \epsilon_1) - \frac{\gamma_2}{2} - \epsilon_1 \gamma_3\}$$

$$c_3 = \{\frac{1}{2\gamma_1} + \frac{\epsilon_1}{\gamma_3}\}$$

$$c_4 = \{\frac{1}{2\gamma_2} + \frac{\epsilon_2}{\gamma_4}\}$$

for $\gamma_j > 0, j \in \{1, 2, 3, 4\}$ and constant $\hat{\beta} > 0$.

Proof. Since H_1 and H_2 are IOSP, we have:

$$\langle y_i | u_i \rangle_T \geq \epsilon_i \|u_i\|_{2,T}^2 + \delta_i \|y_i\|_{2,T}^2 - \beta_i \quad i \in \{1, 2\} \quad (3.7)$$

From Fig. 39, we have $u_1 = r_1 - y_2$ and $u_2 = r_2 + y_1$, therefore:

$$\langle y_1 | u_1 \rangle_T + \langle y_2 | u_2 \rangle_T = \langle y_1 | r_1 \rangle_T + \langle y_2 | r_2 \rangle_T \quad (3.8)$$

Using the interconnection relations, we can write:

$$\begin{aligned} \|u_1\|_{2,T}^2 &= \|r_1\|_{2,T}^2 + \|y_2\|_{2,T}^2 - 2\langle y_2|r_1\rangle_T \\ &\geq \|y_2\|_{2,T}^2 - 2\langle y_2|r_1\rangle_T \end{aligned} \quad (3.9a)$$

$$\begin{aligned} \|u_2\|_{2,T}^2 &= \|r_2\|_{2,T}^2 + \|y_1\|_{2,T}^2 + 2\langle y_1|r_2\rangle_T \\ &\geq \|y_1\|_{2,T}^2 + 2\langle y_1|r_2\rangle_T \end{aligned} \quad (3.9b)$$

Using equations (3.7), (3.8), and (3.9), we have the following inequality:

$$\begin{aligned} \langle y_1|r_1\rangle_T + \langle y_2|r_2\rangle_T + 2\epsilon_1\langle y_2|r_1\rangle_T - 2\epsilon_2\langle y_1|r_2\rangle_T \geq \\ (\delta_1 + \epsilon_2)\|y_1\|_{2,T}^2 + (\delta_2 + \epsilon_1)\|y_2\|_{2,T}^2 - \beta_1 - \beta_2 \end{aligned} \quad (3.10)$$

Using the Cauchy–Schwarz inequality, for any two arbitrary signals r and y , there is a $\gamma > 0$, such that:

$$\begin{aligned} \langle y|r\rangle_T &\leq \|y\|_{2,T}\|r\|_{2,T} + \frac{1}{2}\left(\frac{1}{\sqrt{\gamma}}\|r\|_{2,T} - \sqrt{\gamma}\|y\|_{2,T}\right)^2 \\ &\leq \frac{1}{2\gamma}\|r\|_{2,T}^2 + \frac{\gamma}{2}\|y\|_{2,T}^2 \end{aligned} \quad (3.11a)$$

$$\begin{aligned} \langle y|r\rangle_T &\geq -\|y\|_{2,T}\|r\|_{2,T} - \frac{1}{2}\left(\frac{1}{\sqrt{\gamma}}\|r\|_{2,T} - \sqrt{\gamma}\|y\|_{2,T}\right)^2 \\ &\geq -\frac{1}{2\gamma}\|r\|_{2,T}^2 - \frac{\gamma}{2}\|y\|_{2,T}^2 \end{aligned} \quad (3.11b)$$

If we assign $\gamma_1, \gamma_2, \gamma_3$ as constants for the pair of signals (r_1, y_1) , (r_2, y_2) , and (r_1, y_2) , respectively, in inequality (3.11a), and γ_4 for (r_2, y_1) in inequality (3.11b), then by substituting the obtained inequalities in inequality (3.10) and with some simplification and manipulation, Eqn. (3.6) can be obtained. ■

Finally, we list two useful standard results:

Lemma 2 *The feedback in Fig. 39 is finite-gain \mathcal{L}_2 stable if $\delta_1 + \epsilon_2 > 0$, $\delta_2 + \epsilon_1 > 0$ [124].*

Theorem 2 *Let $y = H(s)u$, where $H(s) \in \mathbb{R}^{n \times n}$ is an exponentially stable and strictly proper transfer function. If $u \in \mathcal{L}_2$, then $y \in \mathcal{L}_2 \cap \mathcal{L}_\infty$, $\dot{y} \in \mathcal{L}_2$ and $y \rightarrow 0$ as $t \rightarrow \infty$. In addition, if $u \rightarrow 0$ as $t \rightarrow \infty$, then $\dot{y} \rightarrow 0$ [122, 125].*

3.3 Cooperative Robot Manipulators Modeling

In this section, we introduce the dynamical model of N cooperative robots carrying a rigid object by grasping it as shown in Fig. 40. The objective in this section is to model the robots, the object and to establish the coupling between the robots. First we build the augmented model of each robot, its joint mechanisms and the DC motor actuators. Then, based on the augmented model of the individual robots, a comprehensive model of the cooperative robots is introduced. The object is modeled assuming to be a rigid object. Finally, the kinematic and dynamic coupling of the closed chain system is discussed.

To develop the dynamics equations, for the remainder of this paper, unless otherwise told, the following notations are used: any parameter with subscript i indicates the parameter for i th robot, $i \in \{1, \dots, N\}$, and subscript ij indicates the parameter for j th joint of i th robot, $j \in \{1, 2, \dots, n\}$.

3.3.1 Comprehensive Dynamics of Cooperative Robots

We assume there are N non-redundant robots carrying an object by grasping it securely. The dynamics of i th robot, without considering the drive systems, modeled as:

$$D_i^o(q_i)\ddot{q}_i + C_i^o(q_i, \dot{q}_i)\dot{q}_i + g_i(q_i) = \tau_i + J_i^T(q_i)F_i \quad (3.12)$$

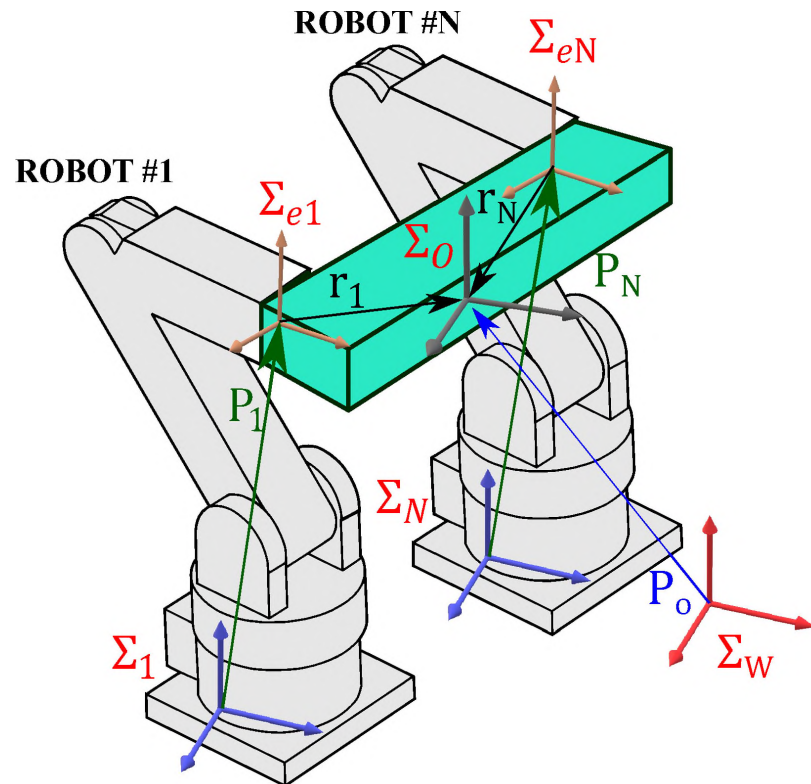


Figure 40: Illustration of N robots grasping an object. The coordinate frames attached to the end-effector, robots' base, load's center of mass, and arbitrary world frame are, respectively, Σ_{ei} , Σ_i , Σ_O , Σ_W .

where $q_i \in \mathbb{R}^n$ is the vector of joint coordinates, $D_i^o(q_i)$ is the inertia matrix, $C_i^o(q_i)$ is the matrix accounting for centripetal and Coriolis effects, $g_i(q_i)$ is the gravity vector, $J_i \in \mathbb{R}^{n \times n}$ is the Jacobian matrix which is assumed to be nonsingular, $F_i = [f_i^T, m_i^T]^T \in \mathbb{R}^n$ is the vector of forces (f_i) and moments (m_i) applied by the object at the end-effector, and $\tau_i = [\tau_{i1}, \tau_{i2}, \dots, \tau_{in}]^T \in \mathbb{R}^n$ is the vector of forces/moments applied at the joints. For ease of notation, we use $J_i^T(q_i)F_i \triangleq \mathcal{T}_{ext}^o$.

All n joints of the robot are considered to be *semi-active*. A semi-active joint mechanism (JM) only exchange mechanical power with the robot, and it is connected to an electric energy storage element source, e.g. an ultracapacitor. We consider that all semi-active joints of all robots are connected to a common storage element, as illustrated in Fig 41, and they are regenerative, allowing the power source to be charged whenever surplus mechanical energy from the robots is available to flow back through DC motors. Also, in each semi-active JM, the interface torque between the JM and the j th robot link can be described by:

$$\tau_{ij} = -J_{ij}\bar{n}_{ij}^2\ddot{q}_{ij} - b_{ij}\bar{n}_{ij}^2\dot{q}_{ij} + \bar{n}_{ij}\tau_{ind_{ij}} \quad (3.13)$$

where J_{ij} , \bar{n}_{ij} , and b_{ij} are the JM moment of inertia, the gear ratio, and friction coefficient, respectively. $\tau_{ind_{ij}} = \alpha_{ij}I_{ij}$ is the induced torque of the motor, where I_{ij} is the current in the motor and α_{ij} is the motor constant.

By combining the dynamics of robot and JMs, the augmented model of robot-JMs can be obtained. This can be done by finding $\tau_{ind_{ij}}$. In each JM, an ideal regenerative four-quadrant power conversion element (motor driver) is used to control the amount and direction of the applied voltage to the DC motor. Fig. 42 shows the model of the JM, where the converter voltage ratio is defined as $u_{ij} = \bar{V}_{ij}/\bar{V}_s$. With

this, the applied voltage to a motor can be written as:

$$V_{ij} = R_{ij}I_{ij} + a_{ij}\dot{q}_{ij} \quad (3.14)$$

where R_{ij} is the resistance of the motor, and $a_{ij} = \alpha_{ij}\bar{n}_{ij}$ [3]. By substituting V_{ij} with u_{ij} in Eqn. (3.14) and obtaining the induced torque of motor as a function of voltage ratio and angular velocity and finally, substituting the induced torque in Eqn. (3.13), the applied torque can be rewritten as:

$$\tau_{ij} = -J_{ij}\bar{n}_{ij}^2\ddot{q}_{ij} - (b_{ij}\bar{n}_{ij}^2 + \frac{a_{ij}^2}{R_{ij}})\dot{q}_{ij} + \frac{a_{ij}u_{ij}}{R_{ij}}V_s \quad (3.15)$$

Replacing τ_{ij} from Eqn. (3.15) into Eqn. (3.12) and moving terms containing \dot{q}_i and \ddot{q}_i from right- to left-hand side, yields the following augmented robot-JM model:

$$D_i(q_i)\ddot{q}_i + C_i(q_i, \dot{q}_i)\dot{q}_i + g_i(q_i) = \mathcal{T}_i + \mathcal{T}_{ext} \quad (3.16)$$

where in the coupled dynamics, D_i^o and D_i are the same in all elements except in diagonal elements such that: $D_i = D_i^o + \text{diag}(J_{ij}\bar{n}_{ij}^2)$, also C_i and C_i^o are only different in diagonal terms such that $C_i = C_i^o + \text{diag}(b_{ij}\bar{n}_{ij}^2 + a_{ij}^2/R_{ij})$, and $\mathcal{T}_i = [U_{i1}, \dots, U_{in}]^T$, where:

$$U_{ij} = \frac{a_{ij}u_{ij}}{R_{ij}}V_s \quad (3.17)$$

Finally, by combining the augmented dynamics of all N robots, the comprehensive dynamics of CRM can be written as:

$$D(q)\ddot{q} + C(q, \dot{q})\dot{q} + G(q) = \mathcal{T} + J^T(q)F \quad (3.18)$$

where $X = [X_1^T, \dots, X_N^T]^T$, $X \in \{q, G, \mathcal{T}, F\}$ and $Y = \text{diag}(Y_1, \dots, Y_N)$, $Y \in \{D, C, J\}$, and $J^T(q)F \triangleq \mathcal{T}_{ext}$.

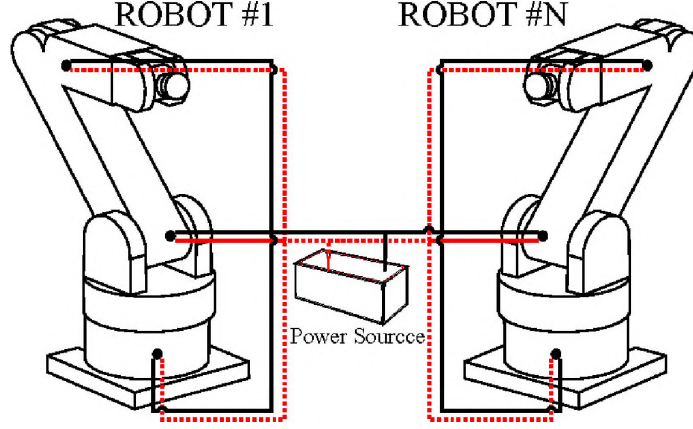


Figure 41: Illustration of semi-active joints connection to a single power source.

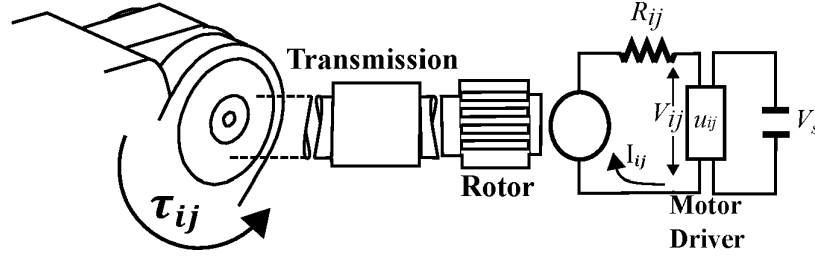


Figure 42: Semi-active joint setup and its connection to motor driver and ultracapacitor.

The following properties of the robot, augmented, and comprehensive dynamics in Eqns. (3.12), (3.16), and (3.18), respectively, are required for the subsequent development [111].

Property 1 *Inertia matrix*: *The inertia matrices $D_i^o(q_i)$, $D_i(q_i)$, and $D(q)$ are uniformly bounded positive definite symmetric matrices.*

Property 2 *Skew-symmetry*: *The following matrices are skew-symmetry:*

$$N_i^o(\dot{q}_i, q_i) = \dot{D}_i^o(q_i) - 2C_i^o(q_i, \dot{q}_i) \quad (3.19a)$$

$$N_i(\dot{q}_i, q_i) = \dot{D}_i(q_i) - 2C_i(q_i, \dot{q}_i) \quad (3.19b)$$

$$N(\dot{q}, q) = \dot{D}(q) - 2C(q, \dot{q}) \quad (3.19c)$$

Property 3 Boundedness of external torque: \mathcal{T}_{ext}^o and \mathcal{T}_{ext} are bounded. Particularly, $||\mathcal{T}_{ext}|| \leq \bar{\mathcal{T}}$

In Property 1, we simply use the physical fact that the inertia matrix, $D_i^o(q_i)$, is inherently positive definite (PD). Adding positive terms to the diagonal elements does not change this property, therefore, $D_i(q_i)$ is PD. Consequently, $D(q)$ is PD. The proof for skew-symmetry property of $N_i^o(\dot{q}_i, q_i)$ can be found in [11]. Because the difference between the terms in $N_i^o(\dot{q}_i, q_i)$ and $N_i(\dot{q}_i, q_i)$ only appears in the diagonal elements, the skew-symmetry property would be preserved. Hence, $N(\dot{q}, q)$ is skew-symmetry. Finally, we assume the external torque in joint space, i.e. \mathcal{T}_{ext}^o , is only a function of forces/moments applied by the payload, and it is bounded.

3.3.2 Dynamics of the Payload

The dynamics and kinematics of manipulators are coupled because the contact forces in all robots are interacting through the load. The dynamic coupling effects can be measured using the dynamics of the load. It is assumed that the mass of object is in its center of mass at Σ_O and the orientation is the orientation of coordinate frame Σ_O as shown in Fig. 40. In the world frame (Σ_W), the translation and rotation dynamics for the object are:

$$\begin{bmatrix} m_o I_{3 \times 3} & 0_{3 \times 3} \\ 0_{3 \times 3} & I_o \end{bmatrix} \begin{bmatrix} \ddot{P}_o \\ \dot{\omega}_o \end{bmatrix} + \begin{bmatrix} -m_o \mathbf{g} \\ \Omega_o I_o \omega_o \end{bmatrix} = J_o^T F \triangleq F_o \quad (3.20)$$

where $[P_o^T, \omega_o^T]^T = [x_o, y_o, z_o, \omega_x, \omega_y, \omega_z]^T$ is the vector of positions and angular velocities of the load. $I_{3 \times 3}$ and $0_{3 \times 3}$ are the identity and the null matrices, respectively, m_o is the mass of the load, and I_o is the moment of inertia about the center of mass. Ω_o is a skew-symmetric matrix, representing the cross product of $\omega_o \times I_o \omega_o$, F_o is the vector of all forces/moments applied at the center of mass of load, and

$J_o^T = [J_{o_1}^T \dots J_{o_N}^T] \in \mathbb{R}^{6 \times 6N}$ is called the grasp matrix and defined as:

$$J_o^T = \begin{bmatrix} I_{3 \times 3} & 0_{3 \times 3} & \dots & I_{3 \times 3} & 0_{3 \times 3} \\ -S(r_1) & I_{3 \times 3} & \dots & -S(r_N) & I_{3 \times 3} \end{bmatrix} \quad (3.21)$$

where r_i is the vector from Σ_{ei} to Σ_o (see Fig. 40) and $S(r_i)$ is a skew-symmetric matrix, representing $r_i \times F_i$. The applied forces/moments by manipulators, F , can be decomposed to motion-inducing and internal parts as:

$$F = F_M + F_I \quad (3.22)$$

where F_M is the motion-inducing part that may balance the object's dynamics and F_I is the internal part consists of compressive, tensile and torsion forces/moments. Since F_I does not contribute to the motion of the object and has no net force, thus it spans the null space of J_o^T . Based on this fact, decomposition as equations (3.23) can be used to find F_M and F_I where $(J_o^T)^+$ is the generalized inverse of J_o^T [27].

$$F_M \triangleq [F_{M_1}^T, \dots, F_{M_N}^T]^T = (J_o^T)^+ J_o^T F \quad (3.23a)$$

$$F_I \triangleq [F_{I_1}^T, \dots, F_{I_N}^T]^T = (I_{6N \times 6N} - (J_o^T)^+ J_o^T) F \quad (3.23b)$$

Using equations (3.23) requires measuring force/moment at the end-effectors. This can be accomplished by installing a force sensor. To avoid direct measurement of force/moment, methods based on load distribution are introduced in [77, 81, 82]

3.3.3 Coupling in Cooperative Robots

The dynamics (payload dynamics) and kinematics coupling cause constraint motion in each robot due to the closed chain configuration of the CRM. The kinematics coupling is defined as a set of equations, relating the translational and the rotational

motions of the end-effectors that hold and move the rigid object securely [29]. The constraints on translational motion are obtained by expressing P_o , in Fig. 40, by the concatenated vectors that connect the origin of Σ_w to the load's center of mass, Σ_o . The orientation of the end-effectors, Σ_{ei} , can be described by the orientation matrix R_{ei} . In the world frame, the translational and rotational constraints are defined as:

$$P_{Oi} + P_i(q_i) + r_i(q_i) = P_{O\hat{o}} + P_{\hat{i}}(q_{\hat{i}}) + r_{\hat{i}}(q_{\hat{i}}) \quad (3.24a)$$

$$\Gamma_i(q_i) - \Gamma_k(q_{\hat{k}}) = \delta R_{i\hat{i}} \quad i, \hat{i} \in \{1, \dots, N\} \quad (3.24b)$$

where P_i and r_i are a function of joints variables and can be determined using robot forward kinematics. P_{Oi} is the vector that connects world frame origin to the origin of the i th robot. Since robots are fixed, P_{Oi} is assumed to be a constant vector. $\Gamma_i(q_i)$ is the vector that expresses the orientation of the i th end-effector, and $\delta R_{i\hat{i}}$ is a constant vector showing the difference between the orientation of the end-effectors at all time of the maneuver. The orientation matrix, R_{ei} , can be specified in terms of either Euler angles or quaternion. For example, if Euler angles are used, then orientation can be defined by three successive rotations about axes of world frame: i.e., $\phi_i(q_i)$ about X_W , followed by $\theta_i(q_i)$ about Y_W and finally $\psi_i(q_i)$ about Z_W which constitute roll, pitch and yaw angles. So the orientation vector is defined as: $\Gamma_i(q_i) = [\phi_i(q_i), \theta_i(q_i), \psi_i(q_i)]^T$.

For N robots, there are $N(N-1)/2$ translational constraint vectors, each constraint contains three independent scalar equations, i.e. constraints in Σ_W frame. Depending on the representation of the orientation, e.g. Euler or quaternion, various number of scalar constraints can be obtained. For instance, using Euler angles, there are $N(N-1)/2$ rotational constraint vectors which can be extracted from the rotation matrix.

It is worth noting that the object does not add any DOF to the CRM system.

In fact, all state variables in Eqn. (3.20) can be determined based on state variables of the robots. The total DOF of the CRM can be determined from:

$$\text{Total DOF} \triangleq \sum_{\kappa=1}^N L_{\kappa} - L_c \quad (3.25)$$

where L_{κ} is the DOF of each robot and L_c is the number of constraints in the system [126]. For example, if two planar RRR robots grasp a load, then $\text{Total DOF} \triangleq \{3+3\} - 3 = 3$ or if the connections to object is pin-joint then $\text{DOF}_t = \{3+3\} - 2 = 4$ since in the latter example, only position is a constraint and not the orientation due to pin joint connection. The CRM can be categorized under over-actuated systems because the number of actuators is more than DOF.

3.4 Control Implementation and Energy Balances

To devise a control scheme for CRM, there are two main consecutive steps. First, we design a controller to achieve the motion control objective of CRM; moving an object along a desired trajectory while grasping it securely without any damage to either object or robots. Second, a relationship is established between the control signal in the first step and the voltage ratios u_{ij} , which are available control inputs. This arises from the incorporation of storage element voltage feedback V_s in the augmented model. The voltage ratios u_{ij} are adjusted in this work using a method called semi-active virtual control (SVC) [4]. Using SVC enables us to describe energy exchange with the storage element and write energy balance equations for the closed system including robots and storage elements.

3.4.1 Semi-active Virtual Control Strategy

Assume that a motion controller, called virtual control law (τ_{ij}^v), for U_{ij} in Eqn. (3.18) has been designed. For τ_{ij}^v to meet the control objectives for the augmented model, a

solution for u_{ij} is sought that enforces:

$$\tau_{ij}^v = \frac{a_{ij}u_{ij}}{R_{ij}}V_s \quad (3.26)$$

To design the virtual control, any feedback law compatible with the desired motion control objectives can be selected. If virtual matching, i.e. $\tau_{ij}^v = U_{ij}$, holds at all times, properties that apply to the virtual design such as stability, tracking performance, robustness, etc. will be propagated to the actual system. Virtual matching is possible as long as the storage element has nonzero voltage and it will hold exactly whenever the power converters are not saturated (e.g., $-1 \leq u_{ij} \leq 1$) and there is accurate knowledge of parameters a_{ij} and R_{ij} . The modulation law for exact virtual matching is obtained by solving for u_{ij} from Eqn. (3.26).

The SVC technique uses V_s as feedback information in the virtual matching of Eqn. (3.26). This approach permits the formulation of control laws and energy balance equations *without the need for a model of the storage element*. Devices such as ultracapacitors and batteries have complex and uncertain models.

3.4.2 Internal and External Energy Balance

The internal energy balance describes the power exchange between the semi-active joints and power storage element. Assuming there is no power lost during power exchange between the power source and DC motors, the input/output energy balance for the motor drives can be written as:

$$V_s I_s = \sum_{i=1}^N \sum_{j=1}^n V_{ij} I_{ij} \quad (3.27)$$

where V_s and I_s are the voltage and current of the power storage, respectively. Dividing both sides by V_s , substituting current from Eqn. (3.14) into Eqn. (3.27), and

taking the integral in the time interval $[0, T]$, the internal energy balance equation can be obtained as follows:

$$\Delta E_s = \int_0^T (\dot{q}^T \mathcal{T}^v - (\mathcal{T}^v)^T R_a \mathcal{T}^v) dt \quad (3.28)$$

where ΔE_s is the electric energy change in the power storage, $\mathcal{T}^v = [(\tau_1^v)^T, \dots, (\tau_N^v)^T]^T$, $\tau_i^v = [\tau_{i1}^v, \dots, \tau_{in}^v]^T$, and $R_a = \text{diag}(R_{ij}/a_{ij}^2) \in \mathbb{R}^{nN \times nN}$. The electric energy, E_s is assumed to be a positive-definite function of the power storage charge y , i.e. $E_s = E_s(y)$. We assume during a maneuver, there is enough charge in the storage element for maneuver execution. An example of a power source is the ultracapacitor. All results obtained in this section can be used interchangeably for virtual control design using an ultracapacitor as power source, i.e. $V_s \triangleq V_{cap}$. Furthermore, for a simple model of the ultracapacitor, the dynamics of charge can be obtained as:

$$\dot{y} = \frac{C}{y} \sum_{i=1}^N \sum_{j=1}^n \tau_{ij}^v \dot{q}_{ij} - \frac{R_{ij}}{a_{ij}^2} (\tau_{ij}^v)^2 \quad (3.29)$$

where C is the capacitance. Using Eqn. (3.29) and taking the integral between any two arbitrary times t_1 and t_2 , the internal energy balance can be obtained as:

$$\Delta E_s = \frac{y^2(t_2) - y^2(t_1)}{2C} \quad (3.30)$$

An external energy balance for CRM can be derived as:

$$W_{ext} = \Delta E_c + \Delta E_m^{Tot} + \Sigma_m^{Tot} + \Sigma_e \quad (3.31)$$

where W_{ext} is the work done by external forces/moments, ΔE_m^{Tot} is the change in the mechanical energy of CRM, Σ_m^{Tot} is the mechanical losses, and Σ_e is the resistance heating (Joule) losses [3]. The derivation and definition of terms in Eqn. (3.31) is

outlined in Appendix C.

The external energy balance is useful to map energy flows and conversions in the CRM, characterizing efficiency and losses. The internal energy balance equation is useful for optimization, as explained in the following sections.

Using the external energy balance, the following so-called passivity properties of the CRM can be obtained. Here, we just present two main results. Note that we do not use the following results in developing the proposed controller in this chapter.

Property 4 *SVC* \mathcal{E} passivity: *SVC preserves the passivity of the system with respect to the virtual control design.*

Proof. The extended dynamics of robots and storage unit in Eqns. (3.18) and (3.29) is:

$$\begin{cases} D(q)\ddot{q} + C(q, \dot{q})\dot{q} + G(q) = \mathcal{T} + \mathcal{T}_{ext} \\ \dot{y} = \frac{C}{y}(\dot{q}^T \mathcal{T}^v - (\mathcal{T}^v)^T R_a \mathcal{T}^v) \end{cases} \quad (3.32)$$

Here we assume the ultracapacitor is fully charged at time t_1 , the beginning of the maneuver, and at time t_2 , end of the maneuver, enough energy left in it. Therefore, the desired torque is equal to applied torque. The external energy balance in Eqn. (3.31) is:

$$W_{ext} = \Delta E_s + \Delta E_m^{Tot} + \Sigma_m^{Tot} + \Sigma_e \quad (3.33)$$

We start by rewriting the resistance heating losses in Eqn. (C.11), using Eqn. (C.2), as:

$$\Sigma_e = \int_0^t \{(\mathcal{T}^v)^T R_a \mathcal{T}^v + \dot{q}^T R_a^{-1} \dot{q} - 2\dot{q}^T \mathcal{T}^v\} dt \quad (3.34)$$

Combining ΔE_c and Σ_e , we have:

$$W_{ext} = \Delta E_m^{Tot} + \Sigma_m^{Tot} + \int_0^t \{\dot{q}^T R_a^{-1} \dot{q} - \dot{q}^T \mathcal{T}^v\} dt \quad (3.35)$$

Taking the last term of integral to the left-hand side, using the fact $\Sigma_m \geq 0$ and assuming $E_m \triangleq \mathcal{H}$, we can write:

$$\Delta \mathcal{H} \triangleq \mathcal{H}(t) - \mathcal{H}(0) \leq \int_0^t \dot{q}^T(\xi) \bar{T}(\xi) d\xi \quad (3.36)$$

where $\bar{T} = \mathcal{T}^v + \mathcal{T}_{ext}$ is the sum of applied forces/moments. It is important to note that if $\mathcal{T}^v \neq \mathcal{T}$, then passivity in Eqn. (3.36) is no longer valid. \mathcal{T}^v is a virtual signal that is not applied to robots. However, if it is equal to the actual applied torque to the robots, Eqn. (3.36) is effective. Also, the proposition is valid when $\mathcal{T}_{ext} = 0$, e.g., a single robot without any interaction with the environment. ■

Furthermore, to keep the safety of robots and the load, it is desired to realize the passivity of robots with respect to the external force/moments.

Property 5 *The external torque \mathcal{E} passivity:* *The extended dynamics in Eqn. (3.32) is input strict passive with respect to the input/output pair $\langle \mathcal{T}_{ext} | \dot{q} \rangle_T$.*

Proof. The external energy balance in Eqn. (3.31) is:

$$W_{ext} = \Delta E_m^{Tot} + \Delta E_s + \Sigma \quad (3.37)$$

In Eqn. (3.37), the total energy change in the system is $\Delta E = \Delta E_m + \Delta E_s$ and the dissipation term, $\Sigma = \Sigma_m^{Tot} + \Sigma_e$, is positive. Therefore, in the view of Eqns. (C.10)

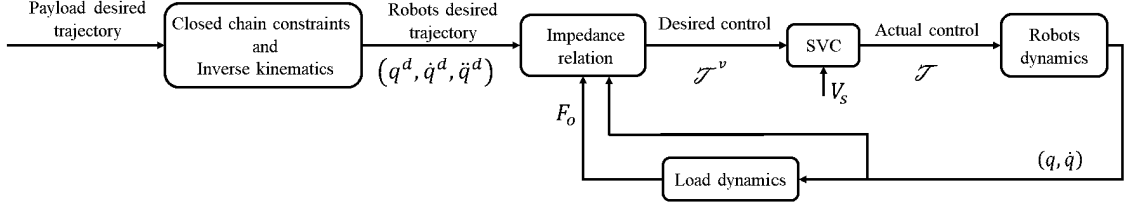


Figure 43: Control scheme to control CRM in joint space, using impedance relation and SVC.

and (C.11), we have:

$$\Delta\mathcal{H} + \delta_0 \int_0^t \|\dot{q}(\xi)\|_{2,t}^2 d\xi \leq W_{ext} \quad (3.38)$$

where δ_0 is a positive value related to generic friction and gear ratio. The above inequality can be written as the following passivity condition:

$$\Delta\mathcal{H} \leq \int_{t_1}^{t_2} \dot{q}^T(\xi) \mathcal{T}_{ext}(\xi) d\xi - \delta_0 \int_0^t \|\dot{q}(\xi)\|_{2,t}^2 d\xi \quad (3.39)$$

■

3.5 Control Scheme

In this study, the motion task is defined as following a desired trajectory closely but allowing deviations from the desired trajectory to limit the interaction forces/moments that could damage the robots or payload. This can be captured by requiring all internal signals in a feedback control loop to be bounded, which is conveniently achieved with the passivity and \mathcal{L}_2 stability tools. Therefore, a control scheme based on impedance relation is developed to accomplish the motion task. Impedance control enforces a compliant behavior to avoid large values of contact force/moment [27, 28]. This technique is particularly useful in CRM since there is interaction between robots and the load.

The proposed control scheme is according to Fig. 43. We assume the load's center of mass is following a pre-designed desired trajectory in world space. That is, the translational and rotational information of center of mass are P_o^d and R_o^d , respectively.

For the i th robot, the end-effector's desired position (P_i^d), orientation (R_{ei}^d), linear velocity (\dot{P}_i^d), angular velocity (ω_{ei}^d), proportional linear acceleration (\ddot{P}_i^d), and angular acceleration ($\dot{\omega}_{ei}^d$) can be calculated using:

$$\begin{aligned}
P_i^d &= P_o^d - R_o^d r_i \\
R_{ei}^d &= R_o^d \\
\dot{P}_i^d &= \dot{P}_o^d + S(R_o^d r_i) \omega_o^d \\
\omega_{ei}^d &= \omega_o^d \\
\ddot{P}_i^d &= \ddot{P}_o^d + S(\omega_o^d) S(R_o^d r_i) \omega_o^d + S(R_o^d r_i) \dot{\omega}_o^d \\
\dot{\omega}_{ei}^d &= \dot{\omega}_o^d
\end{aligned} \tag{3.40}$$

where $S(\cdot)$ is the matrix performing cross-product and R_o^d is a matrix transformation that transfers r_i from object's frame (Σ_o) to the frame attached to the i th end-effector (Σ_{ei}) [28]. Using translational and rotational information of the end-effector, from Equation. (3.40), kinematics of the robot, and any inverse kinematics technique, the desired position (q_i^d), velocity (\dot{q}_i^d) and acceleration (\ddot{q}_i^d) of joints, can be obtained [111, 28]. The desired states in joint space along with the actual states and the interaction force between robots and the payload are used in the impedance relation to calculate the virtual control, \mathcal{T}^v . The SVC uses the power source voltage information to regulate the virtual control and creates the actual control signal.

Note that in the case of non-redundant cooperative robots, obtaining the

desired values is relatively easy. For the non-redundant robots, desired velocities are determined with:

$$\dot{q}_i^d = J_i(q_i^d)^{-1} \dot{X}_{ei}^d \quad (3.41)$$

where $\dot{X}_{ei}^d = [(\dot{P}_i^d)^T, (\omega_{e1}^d)^T]^T$ and $J_i(q_i^d)$ is the Jacobian of the robot. Differentiating Eqn. (3.41) and solving for \ddot{q}_i^d , yields:

$$\ddot{q}_i^d = J_i(q_i^d)^{-1} (\ddot{X}_{ei}^d - \dot{J}_i(q_i^d) \dot{q}_i^d) \quad (3.42)$$

to find the desired acceleration of joints.

3.6 Impedance Control

When there is an interaction between robot and environment and force-position relation is of concern, control based on impedance relation could be the best approach. The idea of designing a controller based on an impedance relation was first introduced by Hogan [127, 128]. Impedance control includes regulation and stabilization of robot motion by establishing a mathematical relationship between the interaction forces and the robot trajectories. The general format of this relationship can be described by a non-homogeneous nonlinear ordinary differential equation (ODE) as:

$$G(t, \tilde{x}, \tilde{x}', \dots, \tilde{x}^m) = F(t) \quad \forall t \geq 0 \quad (3.43)$$

where $\tilde{x} \in \mathbb{R}^n$ is the states vector of error defined in a general coordinate, and it is a function of reference and actual states, $\tilde{x}^m \triangleq d^m \tilde{x} / dt^m$, and $F(t) \in \mathbb{R}^n$ is the interaction force/moment defined in the same reference frame as states vector. It is common to use coordinate transformation to define all variables of Eqn. (3.43) in the same desired reference frame. The states vector is usually defined as the difference between reference and actual states. It is possible that in different orders of derivation,

\tilde{x} may or may not be a function of both reference and actual states. Since the introduction of the impedance control concept, various mathematical relations have been introduced. The most prevalent form is a second-order linear ODE (analogous to a forced spring-mass damper system) as:

$$M\tilde{x}'' + B\tilde{x}' + K\tilde{x} = F(t) \quad (3.44)$$

where M , B , and K are inertia, damping, and stiffness matrices, respectively, here called gain matrices which are positive definite and could be constant, function of time and states or defined accordingly as the dynamics of a robot. Non-diagonal gain matrices introduce coupling in the impedance relation, e.g. between translation and rotation movement [86]. However, they are usually chosen as constant diagonal matrices, which is equivalent to consider linear damper and spring. The linearity of the damper and spring can be replaced by a nonlinear relation. For example, a nonlinear spring can be substituted instead of $K\tilde{x}$ term [84]. It is worth mentioning that an inherent weakness of establishing a simple impedance relation as Eqn. (3.44), is its approach to model the interaction between force and motion which does not account for the transient interval of motion, e.g. from free to constraint motion [129].

3.6.1 Impedance Control as Virtual Controller

The characteristics of an impedance control problem are given as a relationship between a desired trajectory and a desired dynamics. In this sense, the system is forced to establish a mathematical relationship between the interaction forces and the position error. To design the virtual control, we enforce the following relationship introduced in [125]:

$$\lim_{t \rightarrow \infty} M\ddot{\tilde{q}} + B\dot{\tilde{q}} + K\tilde{q} = \mathcal{T}_{ext} \quad (3.45)$$

where $\tilde{q} = q^d - q$ and the inertia (M), damping (K), and stiffness (K) are diagonal positive-definite matrices called gain matrices here, and all parameters are defined for each robot accordingly. Here we defined the limit of desired dynamics as time approaches infinity equals external torque. The advantage of this approach is to account for the transition phase when the actual dynamics needs to match itself to the desired dynamics. Therefore, any sudden movement or increase in the applied torque can be avoided.

To achieve the objective in Eqn. 3.45, we define an auxiliary error as:

$$\zeta = \tilde{q} - [p^2 M + pB + K]^{-1} \mathcal{T}_{ext} \quad (3.46)$$

where $p = d/dt$. It is easy to verify that if ζ converges to zero, the desired impedance in Eqn. (3.45) is achieved. Therefore, we define the following variables:

$$S = -(\dot{\zeta} + \Lambda \zeta) \quad (3.47a)$$

$$\dot{q}_r = \dot{q} - S \quad (3.47b)$$

where Λ is a diagonal positive definite matrix. Finally, the virtual torque can be calculated using:

$$\mathcal{T}^v = D(q)\ddot{q}_r + C(q, \dot{q})\dot{q}_r + G(q) - K_D S - \mathcal{T}_{ext} \quad (3.48)$$

where K_D is a positive definite matrix. From a practical point of view, \dot{q}_r and \ddot{q}_r in equation. (3.48) can be implemented by:

$$\dot{q}_r = \dot{q}^d + \Lambda \tilde{q} - (pI + \Lambda)[p^2 M + pB + K]^{-1} \mathcal{T}_{ext} \quad (3.49a)$$

$$\ddot{q}_r = \ddot{q}^d + \Lambda \dot{\tilde{q}} - p(pI + \Lambda)[p^2 M + pB + K]^{-1} \mathcal{T}_{ext} \quad (3.49b)$$

which shows that the implementation of the controller does not require the measurement of the acceleration.

Practical Implementation of the Controller

To implement the controller, we need to calculate force filter in Eqn. 3.48. Because the impedance gains are diagonal, part of desired torque calculation, i.e. determining \dot{q}_r and \ddot{q}_r , can be done separately for each joint. Here we consider the analysis only for one joint. All the results in this section can be generalized for all joints in the robots. Lets define the following equation:

$$\bar{y} = [p^2 M + pB + K]^{-1} \mathcal{T}_{ext} \quad (3.50)$$

where $\bar{y} = [\bar{y}_1^T, \dots, \bar{y}_N^T]^T \in \mathbb{R}^{nN}$ and $\bar{y}_i = [\bar{y}_{i1}, \dots, \bar{y}_{in}]^T$. The state space representation of Eqn. (3.50) is:

$$\dot{Z} = \bar{A}Z + \bar{B}\mathcal{T}_{ext} \quad (3.51)$$

where $Z = [\bar{y}^T; \dot{\bar{y}}^T]^T = [\bar{y}_{11}, \dots, \bar{y}_{1n}, \dots, \bar{y}_{N1}, \dots, \bar{y}_{Nn}, \dot{\bar{y}}_{11}, \dots, \dot{\bar{y}}_{1n}, \dots, \dot{\bar{y}}_{N1}, \dots, \dot{\bar{y}}_{Nn}]^T \in \mathbb{R}^{2nN}$. The state transition and input matrices are defined as:

$$\bar{A} = \begin{bmatrix} \mathbf{0}_{nN \times nN} & \mathbf{1}_{nN \times nN} \\ -M^{-1}K & -M^{-1}B \end{bmatrix}, \bar{B} = \begin{bmatrix} \mathbf{0}_{nN \times nN} \\ M^{-1} \end{bmatrix}$$

where $\mathbf{0}_{nN \times nN}$ is a null matrix and $\mathbf{1}_{nN \times nN}$ is the identity matrix. Therefore, the response can be calculated as:

$$Z(t) = e^{\bar{A}t} Z(t_0) + \int_0^t e^{\bar{A}(T-t)} \bar{B} \mathcal{T}_{ext} dt \quad (3.52)$$

where $Z(t_0)$ is the initial value of the defined states. The above analytical solution

gives \bar{y} and $\dot{\bar{y}}$. Hence, ζ and $\dot{\zeta}$ in Eqn. (3.46) can be calculated as:

$$\zeta = \tilde{q} - \bar{y}, \quad \dot{\zeta} = \dot{\tilde{q}} - \dot{\bar{y}} \quad (3.53)$$

and S in Eqn.(3.47a) can be determined based on these values. Also, \dot{q}_r and \ddot{q}_r can be calculated by:

$$\dot{q}_r = \dot{q}^d + \Lambda \tilde{q} - (\dot{\bar{y}} + \Lambda \bar{y}) \quad (3.54a)$$

$$\ddot{q}_r = \ddot{q}^d + \Lambda \dot{\tilde{q}} - (\ddot{\bar{y}} + \Lambda \dot{\bar{y}}) \quad (3.54b)$$

Finally, the desired control can be computed accordingly.

Theorem 3 *Consider the auxiliary error in Eqn. (3.46) and S in Eqn. (3.47a). Then the followings hold:*

1. $S \in \mathcal{L}_2$
2. $\zeta \in \mathcal{L}_2 \cap \mathcal{L}_\infty, \dot{\zeta} \in \mathcal{L}_2$
3. $\zeta \rightarrow 0$ as $t \rightarrow \infty$.
4. $q, \dot{q} \in \mathcal{L}_{2e}$ and bounded.

and therefore, the closed-loop system is \mathcal{L}_2 finite gain stable.

Proof. (a) Assuming $\mathcal{T}^v = \mathcal{T}$, by substituting Eqn. (3.48) in Eqn. (3.18), the closed-loop system is obtained as:

$$D(q)\dot{S} + [C(q, \dot{q}) + K_D]S = 0 \quad (3.55)$$

We choose the following Lyapunov function candidate for the closed-loop system:

$$V(t) = \frac{1}{2} S^T D(q) S \quad (3.56)$$

Differentiating Lyapunov function with respect to time and with some manipulation and simplification, it yields:

$$\dot{V}(t) = -S^T K_D S \quad (3.57)$$

Equations (3.56) and (3.57) imply that S is asymptotically stable and therefore $S \in \mathcal{L}_2$.

(b,c) Using the definition of S in Eqn. (3.47a), ζ and its derivative can be written as:

$$\zeta = -(pI + \Lambda)^{-1} S \quad (3.58a)$$

$$\dot{\zeta} = -p(pI + \Lambda)^{-1} S \quad (3.58b)$$

where $(pI + \Lambda)^{-1}$ describes a strictly proper, exponentially stable transfer function [123]. Using Theorem 2 and the fact that $S \in \mathcal{L}_2$, we conclude $\zeta \in \mathcal{L}_2 \cap \mathcal{L}_\infty$, $\dot{\zeta} \in \mathcal{L}_2$, and hence $\zeta \rightarrow 0$ as $t \rightarrow \infty$. The fact that auxiliary error, ζ , converges to zero, shows the objective of achieving the desired impedance relation in Eqn. (3.45).

(d) By taking the derivative of both sides of Eqn. (3.46) and rearranging the terms, we have:

$$\dot{q} = \dot{q}^d - \dot{\zeta} - p[p^2 M + pB + K]^{-1} \mathcal{T}_{ext} \quad (3.59)$$

Using Eqn. (3.58b), Eqn. (3.59) can be represented in a feedback interconnection form as depicted in Fig 44(a). Here we define $\text{ENV}(\dot{q})$ as a passive operator that maps \dot{q} to \mathcal{T}_{ext} . The environment (load) is passive because the object is assumed to be a pure

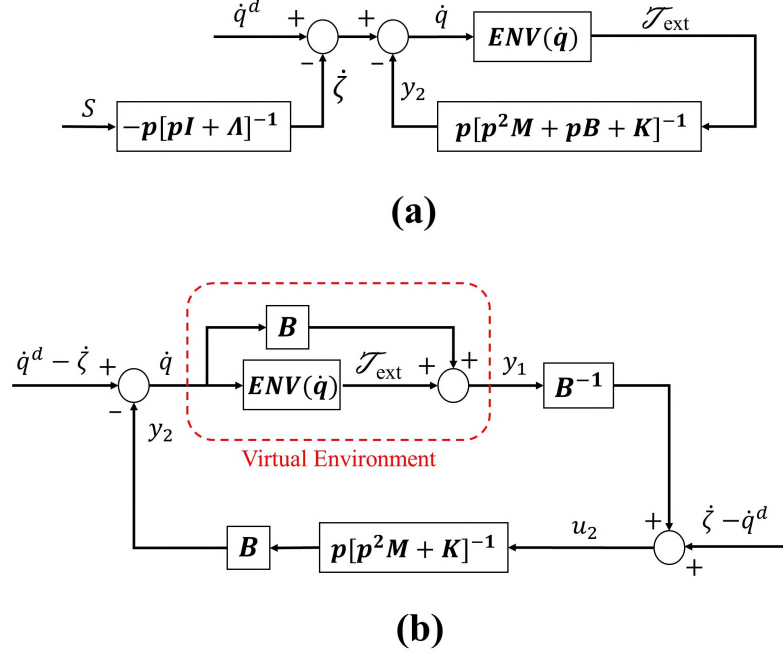


Figure 44: (a) Feedback interconnection with one external input. (b) Transformation of interconnection to two external inputs.

mass that is held by grasping. Since it is passive, we can write:

$$\langle \mathcal{T}_{\text{ext}} | \dot{q} \rangle_T \geq -\tilde{\beta} \quad (3.60)$$

It can be easily shown that the operator $\bar{H}_2 \triangleq p[p^2M + pB + K]^{-1}$ is only passive. Therefore, this feedback loop does not reveal any information about boundedness of signals and it is inconclusive. By performing the loop transformation technique [122, 121], the equivalent interconnection can be presented as Fig 44(b). In this figure, the virtual environment operator (H_1) is composed of passive environment as represented by Eqn. (3.60) and a feed forward term. So it is an ISP system with the following property:

$$\langle y_1 | \dot{q} \rangle_T \geq -\tilde{\beta} + \underline{\lambda}_B \|\dot{q}\|_{2,T}^2 \quad (3.61)$$

where $\underline{\lambda}_B > 0$ is the smallest eigenvalue of the gain matrix B . The operator $H_2 \triangleq$

$pB[p^2M + K]^{-1}$, which maps u_2 to y_2 , is only passive. By comparing Fig 44(b) and Fig 39, and using Eqn. (3.4), we can conclude that $\epsilon_1 = \underline{\lambda}_B$, $\epsilon_2 = \delta_1 = \delta_2 = 0$. Based on Lemma 1, we can write:

$$\bar{c}_2 \|y_2\|_{2,T}^2 \leq \bar{c}_3 \|\dot{q}^d - \dot{\zeta}\|_{2,T}^2 + \bar{c}_4 \|\dot{\zeta} - \dot{q}^d\|_{2,T}^2 - \bar{\beta} \quad (3.62)$$

where \bar{c}_i can be always chosen as positive numbers. It was shown that $\zeta \in \mathcal{L}_2$ and also using the fact that desired trajectory is bounded, we can conclude $\dot{q}^d, \dot{\zeta} \in \mathcal{L}_{2e}^n$. Therefore, the right-hand side of Eqn. (3.62) is in \mathcal{L}_{2e}^n and so is the left-hand side, i.e. $y_2 \in \mathcal{L}_{2e}^n$ and bounded. Consequently, all signals inside the loop are bounded, i.e. $\dot{q}, \mathcal{T}_{ext}, y_1, u_2 \in \mathcal{L}_{2e}^n$.

In particular, $\exists \bar{\mathcal{T}}$ such that $\|\mathcal{T}_{ext}\| \leq \bar{\mathcal{T}}$. The impedance relation as a function of the auxiliary error in Eqn. (3.46), can be rewritten as:

$$M\ddot{\bar{y}} + B\dot{\bar{y}} + K\bar{y} = \mathcal{T}_{ext} \quad (3.63)$$

where $\bar{y} = \tilde{q} - \zeta$. It can be shown that all solutions of Eqn. (3.63) comply with the inequality:

$$\max(\|\dot{\bar{y}}\|_{2,T}, \|\bar{y}\|_{2,T}) \leq C^{-\kappa t} \sqrt{\|\dot{\bar{y}}_0\|^2 + \|\bar{y}_0\|^2} + \frac{C\bar{\mathcal{T}}}{\kappa} \quad (3.64)$$

where C is a constant, $\kappa > 0$, and $\dot{\bar{y}}_0, \bar{y}_0$ are the initial conditions [130]. Because the right-hand side of Eqn. (3.64) is monotonically decreasing and tends to a finite value and $\zeta \in \mathcal{L}_2$, we have $q \in \mathcal{L}_{2e}^n$. ■

3.7 Optimization problem

We aim to find the impedance gains, B and K , that maximize the energy regeneration given the pre-designed references used in the impedance relation of 3.45. Maximizing ΔE_s in Eqn. (3.30) means less amount of energy is drawn from the storage element. A value of $\Delta E_s > 0$ indicates energy regeneration and $\Delta E_s < 0$ indicates energy consumption. Considering constant impedance parameters first, we define the damping and stiffness gains as:

$$\begin{cases} B = B_c + \bar{B} \\ K = K_c + \bar{K} \end{cases} \quad (3.65)$$

where B_c and K_c are fixed and \bar{B} and \bar{K} are limited within an upper- and lower-bounds. The optimization is aimed to find \bar{B} and \bar{K} such that ΔE_s is maximized. Considering Eqn. (3.30) and the constraints in Eqn. (3.24), a static optimization problem is formulated as:

$$\max_{\bar{B}, \bar{K}} \Delta E_s = \int_0^T (\dot{q}^T \mathcal{T}^v - (\mathcal{T}^v)^T R_a \mathcal{T}^v) dt \quad (3.66a)$$

$$\text{subject to: } \begin{cases} \text{I} & : P_i(q_i) + r_i(q_i) = P_i(q_i) + r_i(q_i) \\ \text{II} & : \Gamma_i(q_i) - \Gamma_k(q_i) = \delta R_{i\dot{i}} \quad i, \dot{i} \in \{1, \dots, N\} \\ \text{III} & : -V_s \bar{a}_R \leq \mathcal{T}^v \leq V_s \bar{a}_R \\ \text{IV} & : LB_B \leq \dot{B} \leq UB_B \\ \text{V} & : LB_K \leq \dot{K} \leq UB_K \end{cases} \quad (3.66b)$$

where the conditions I and II are the translational and rotational constraints, condition III is derived from Eqn. (3.26) and the fact that $-1 \leq u_{ij} \leq 1$. $\bar{a}_R = \text{Vec}(a_{ij}/R_{ij}) \in \mathbb{R}^{nN}$ and $\text{Vec}(\cdot)$ represents the vectorization operator which creates a column vector by stacking a_{ij}/R_{ij} for all joints. The lower- and upper-bound for the

damping and stiffness gains are indicated in conditions IV and V, respectively. These bounds determine the search area for the gains. The problem can be solved with a variety of suitable methods, such as the genetic algorithm used in the simulation example.

3.8 Variable Impedance Control

The optimization in Eqn. 3.66 searched for constant values of impedance gain during the motion task. It is possible to look for variable gains, i.e. $B(t)$ and $K(t)$. Variable impedance shows better versatility when there is interaction with environment, and it has been shown to have better performance [92, 30, 93, 91, 101]. Optimal variable gains may result in further reductions in energy consumption.

If the damping and stiffness gains are time-varying matrices constrained to be positive definite, the relation between y_2 and u_2 in Fig. 44(b) can be written in the format of a linear time-varying system as:

$$\dot{\mathcal{X}}(t) = \mathfrak{A}(t)\mathcal{X}(t) + \mathfrak{B}u_2(t) \quad (3.67a)$$

$$y_2(t) = \mathfrak{C}(t)\mathcal{X}(t) \quad (3.67b)$$

where

$$\mathfrak{A}(t) = \begin{bmatrix} \mathbf{0} & \mathbf{1} \\ -M^{-1}K(t) & \mathbf{0} \end{bmatrix}, \mathfrak{B} = \begin{bmatrix} \mathbf{0} \\ M^{-1} \end{bmatrix}, \mathfrak{C}(t) = \begin{bmatrix} \mathbf{0} & B(t) \end{bmatrix}$$

In the above matrices, $\mathbf{0} \in \mathbb{R}^{nN \times nN}$ is a null matrix and $\mathbf{1} = \text{diag}(\mathbf{1}) \in \mathbb{R}^{nN \times nN}$ is a diagonal matrix.

Variable gains may result in the loss of passivity in the desired impedance relation [92]. However, we establish a result providing conditions to preserve passivity in the time-varying case:

Theorem 4 *The states of the system are bounded and passivity is guaranteed if the following condition is satisfied:*

$$\bar{\lambda} < 2\underline{\lambda}_B^2 \quad (3.68)$$

where $\underline{\lambda}_B$ is the smallest eigenvalue of $B(t)$, $\bar{\lambda}$ is the largest eigenvalue of $\dot{P}(t) + P(t)\mathfrak{A}(t) + \mathfrak{A}^T(t)P(t)$, and $P(t) = P^T(t)$ is a positive-definite matrix defined as:

$$P(t) = \begin{bmatrix} K(t) & \mathbf{0} \\ \mathbf{0} & MB(t) \end{bmatrix} \quad (3.69)$$

Proof. We assume $B(t)$ and $K(t)$ are bounded, diagonal, positive definite matrices, therefore $P(t)$ is a continuous and bounded positive-definite matrix. Henceforth, to be concise, we will neglect writing the temporal argument. To study the passivity of the time varying linear system in Eqn. (3.67), the following storage function and its temporal derivative can be considered [131]:

$$\mathcal{V} = \frac{1}{2} \mathcal{X}^T P \mathcal{X} \quad (3.70a)$$

$$\dot{\mathcal{V}} = \frac{1}{2} \mathcal{X}^T \{ \dot{P} + P\mathfrak{A} + \mathfrak{A}^T P \} \mathcal{X} + \mathcal{X}^T P \mathfrak{B} u_2 \quad (3.70b)$$

Integrating $\dot{\mathcal{V}}$ in the time interval $[0, T]$ gives:

$$\int_0^T \dot{\mathcal{V}}(\xi) d\xi = \mathcal{V}(t) - \mathcal{V}(0) \geq -\mathcal{V}(0) \quad (3.71)$$

Substituting Eqn. (3.70b) in the above inequality results in the following inequality:

$$\int_0^T \left[\frac{1}{2} \mathcal{X}^T \{ \dot{P} + P\mathfrak{A} + \mathfrak{A}^T P \} \mathcal{X} + \mathcal{X}^T P \mathfrak{B} u_2 \right] d\xi \geq -\mathcal{V}(0) \quad (3.72)$$

Because $P\mathfrak{B} = \mathfrak{C}^T$, assuming $\bar{P} = \dot{P} + P\mathfrak{A} + \mathfrak{A}^T P$, we have:

$$\int_0^T \frac{1}{2} \mathcal{X}^T \bar{P} \mathcal{X} d\xi + \int_0^T y_2^T(\xi) u_2(\xi) d\xi \geq -\mathcal{V}(0) \quad (3.73)$$

where:

$$\bar{P} = \begin{bmatrix} \dot{K} & K - K^T B^T \\ K^T - BK & M \dot{B} \end{bmatrix} \quad (3.74)$$

To study the passivity of input/output in the above inequality, we study three cases of \bar{P} being negative-definite (ND), positive-definite (PD), and indefinite (ID).

1) In case of ND, the integral including \bar{P} is negative, so inequality (3.73) can be written as:

$$\langle y_2 | u_2 \rangle_T \geq -\mathcal{V}(0) \quad (3.75)$$

which proves the passivity of the system and therefore, Theorem 3 and its results are valid.

2) In the case of PD, because $\bar{P} > 0$, passivity can not be concluded directly from Eqn. (3.73). In this case, we consider the following inequalities:

$$\frac{\underline{\lambda}}{2} \int_0^T \mathcal{X}^T \mathcal{X} d\xi \leq \int_0^T \frac{1}{2} \mathcal{X}^T \bar{P} \mathcal{X} d\xi \leq \frac{\bar{\lambda}}{2} \int_0^T \mathcal{X}^T \mathcal{X} d\xi \quad (3.76)$$

where $\underline{\lambda} > 0$ and $\bar{\lambda}$ are the smallest and biggest eigenvalues of \bar{P} , respectively. Also, in the view of output in Eqn. (3.67b), we can write:

$$\underline{\lambda}_B \int_0^T \mathcal{X}^T \mathcal{X} d\xi \leq \int_0^T \mathcal{X}^T \mathfrak{C}^T \mathfrak{C} \mathcal{X} d\xi \leq \bar{\lambda}_B \int_0^T \mathcal{X}^T \mathcal{X} d\xi \quad (3.77)$$

where $\underline{\lambda}_B > 0$ and $\bar{\lambda}_B$ are the smallest and biggest eigenvalues of \mathfrak{C} , respectively.

From equations (3.76) and (3.77), the following inequality can be resulted:

$$\frac{\bar{\lambda}}{2} \int_0^T \mathcal{X}^T \mathcal{X} d\xi \leq \frac{\bar{\lambda}}{2\lambda_B} \int_0^T y_2^T y_2 d\xi \quad (3.78)$$

Using the above inequality together with inequality (3.73), we have:

$$\langle y_2 | u_2 \rangle_T \geq -\mathcal{V}(0) - \frac{\bar{\lambda}}{2\lambda_B} \|y_2\|_{2,T}^2 \quad (3.79)$$

From Lemma 1 and in the view of closed-loop interconnection in Fig 44, we know the lack of passivity in output of one system can be compensated by passivity in input of the other system. In other word, if $\delta_2 + \epsilon_1 > 0$, then all results in Theorem 3 are valid. Therefore, from equations (3.61) and (3.79), the passivity is guaranteed if:

$$\lambda_B - \frac{\bar{\lambda}}{2\lambda_B} > 0 \Rightarrow \bar{\lambda} < 2\lambda_B^2 \quad (3.80)$$

3) In the case of ID, using the fact that an indefinite matrix has at least one positive eigenvalue and at least one negative eigenvalue, we can assume that $\bar{\lambda} > 0$ and all results for PD case are valid for ID case.

In conclusion, the gain matrices can vary as long as inequality (3.80) is satisfied. If the change, i.e. sign of \bar{K} and \bar{B} , leads to a ND value for \bar{P} , inequality (3.80) is automatically satisfied, and the passivity is preserved. If the change leads to PD value for \bar{P} and inequality (3.80) is effective, system stays passive. If none of above happens and change leads to an ID \bar{P} , having inequality (3.80) would be enough for the passivity. Note that the variation of damping matrix does not affect the passivity of H_1 in the interconnection of Fig. 44(b).

■

3.9 Simulation

To simulate CRM system using the proposed impedance control, two identical RRR planar robots are considered. The robots are grasping a rigid rod as shown in Fig. 45. It is assumed the actuators in the robots are DC motors and all joints are powered using an ultracapacitor as storage element. The robots' and the rod's parameters are given in Table VI.

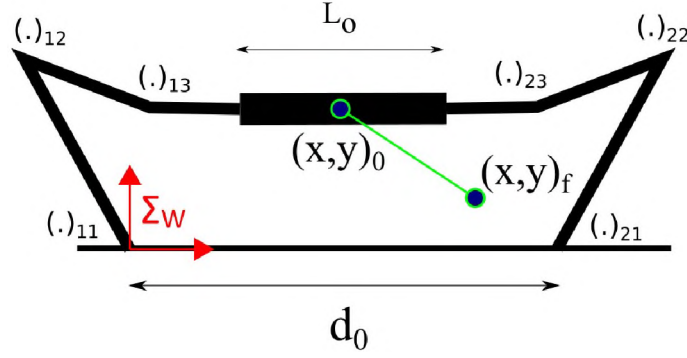


Figure 45: Setup for two identical cooperative robots carrying a load. The world frame is attached to the base of the left robot. The distance between robots is $d_0 = 0.8 \text{ m}$ and robots are placed on the same level. $(.)_{ij}$ represents any parameter for the j th joint of i th robot.

The motion task objective is defined as moving the load's center of mass (CM) from initial position, $(x, y)_0$, to final position, $(x, y)_f$, along a pre-designed desired trajectory. The final condition is relaxed to allow for a search of the optimal

Table VI: The parameters for two identical robots and the object (rod).

Parameter	Value	Unit
Robot:		
1st, 2nd, and 3rd arm lengths	[0.425, 0.39, 0.13]	m
1st, 2nd, and 3rd arm masses	[8.05, 2.84, 1.37]	kg
DC motor resistance	0.4	Ω
DC motor torque constant	0.07	Ω
DC motor gear ratio	50	-
Rod:		
Mass	5	kg
Length (L_0)	0.5	m

Table VII: Parameters of genetic algorithm.

Parameter	Value
Initial population size	50
Max. No. of generation	30
Crossover probability	0.75
Mutation rate	0.02

impedance gains. Accordingly, a set has been defined as:

$$IS = \{p_o(t) | \|p_o(t) - p_o^d(t_f)\| \leq \epsilon_f\} \quad (3.81)$$

where $p_o(t)$ is the position of the load's CM, $p_o^d(t_f)$ is the final desired position, $\|\cdot\|$ is the Euclidean norm, and ϵ_f is a scalar boundary. It is assumed that the motion tasks starts from the initial position, and it is accomplished whenever the final position enters the IS set. After finishing the maneuver, the payload will be detached from the robots.

The desired object trajectory is based on a quintic polynomial and consists of moving the object 0.4 m in the x direction, -0.4 m in the y direction, and a rotation of zero degrees in 1 s. The desired trajectories in joint space is obtained using equations 3.40.

The fixed inertia, damping, and stiffness impedance gains are selected as $M = \text{diag}(18)$, $B_c = \text{diag}(197.5)$, and $K_c = \text{diag}(825)$. Note that the same parameters are selected for both robots. The optimization in Eqn. 3.66 is solved using genetic algorithm (GA). The optimization searches for 12 variables (one damping and one stiffness gain for each joint). The upper- and lower-bounds for the damping and stiffness gains in each joint are $-22 \leq \bar{B}_{ij} \leq 22$ and $-75 \leq \bar{K}_{ij} \leq 75$, respectively. The values and types of GA operators of this study are given in Table VII.

The optimization gives the following impedance gains as optimal values:

$$B_1 = \begin{bmatrix} 176.1 & 0 & 0 \\ 0 & 178.0 & 0 \\ 0 & 0 & 181.0 \end{bmatrix}, B_2 = \begin{bmatrix} 175.6 & 0 & 0 \\ 0 & 176.8 & 0 \\ 0 & 0 & 176.3 \end{bmatrix}$$

$$K_1 = \begin{bmatrix} 752.9 & 0 & 0 \\ 0 & 754.2 & 0 \\ 0 & 0 & 763.6 \end{bmatrix}, K_2 = \begin{bmatrix} 756.4 & 0 & 0 \\ 0 & 761.2 & 0 \\ 0 & 0 & 755.1 \end{bmatrix}$$

where subscripts 1 and 2 denote the matrix for the first and second robot (in Fig. 45, the robot on the left is named robot 1 and the right one is called robot 2). Figures 46 and 47 show the time histories of the reference trajectory and the actual angles for both robots. The reference trajectories are closely tracked due to the relatively high value chosen for K_c . The 2D movement is depicted in Fig. 48 and the virtual controls are shown in Fig. 49.

The power consumption in each joint is shown in Fig. 50. Positive power indicates power consumption by the joint and negative power shows energy regeneration. The energy consumption and regeneration is more pronounced in the first joint of each robot.

Figure 51 shows the Sankey diagrams for the external energy balance of Eqn. 3.31. Most of the energy needed to accomplish the motion task was recovered from the potential energy difference between the initial and final positions. This is a direct consequence of maximizing energy regeneration. To study the effect of energy regeneration, we conclude the results by defining the effectiveness of energy regeneration as [3]:

$$\bar{\epsilon} = 1 - \frac{\Delta E_R}{\Delta E_{NR}} \quad (3.82)$$

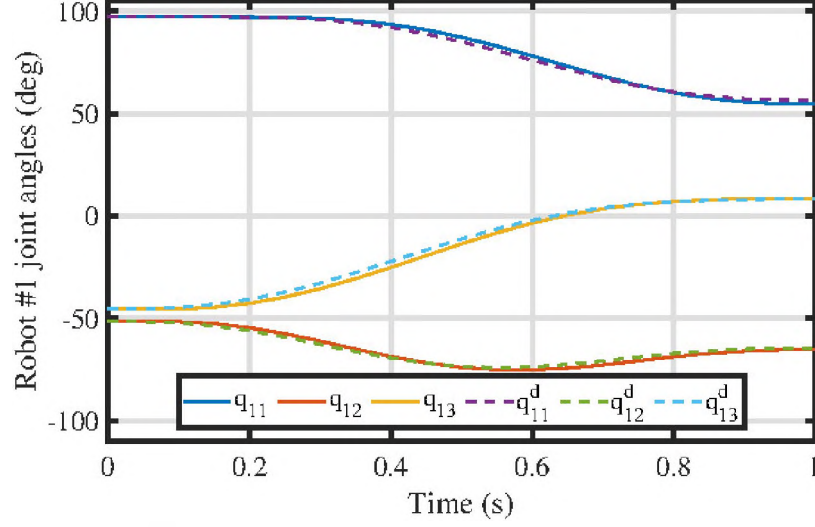


Figure 46: The actual and desired joint angles for Robot #1.

where ΔE_R and ΔE_{NR} are the system energy consumption with and without energy regeneration, respectively. ΔE_{NR} is computed by integrating the power flows in all joints, assuming any negative power is dissipated (i.e. P_{ij} ($P_{ij} \leq 0$) = 0). We have $0 \leq \bar{\epsilon} \leq 1$ where $\bar{\epsilon} = 0$ means energy regeneration has zero effect in reducing the energy consumption and $\bar{\epsilon} = 1$ indicates that energy regeneration completely reduces energy consumption. For the condition of simulation, $\Delta E_R = 9.69 \text{ J}$ and $\Delta E_{NR} = 25.84 \text{ J}$ results in $\bar{\epsilon} = 0.62$. This shows approximately 60% reduction in energy consumption due to energy regeneration.

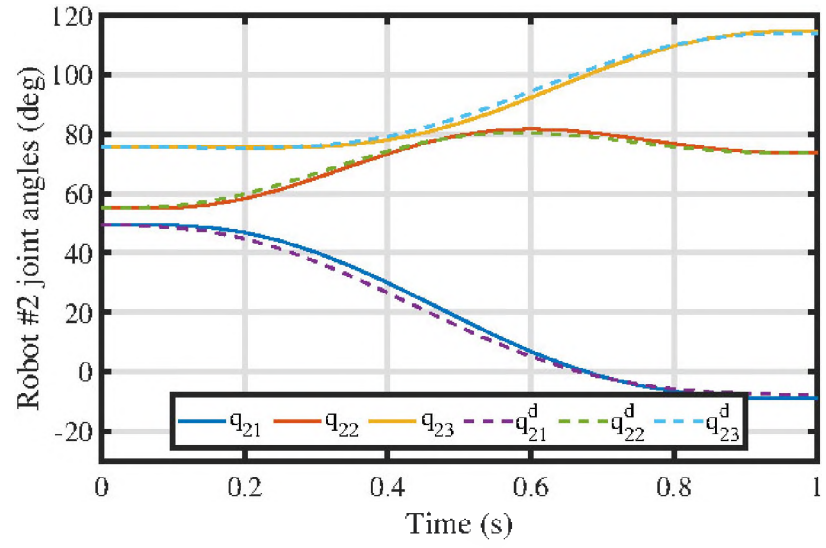


Figure 47: The actual and desired joint angles for Robot #2.

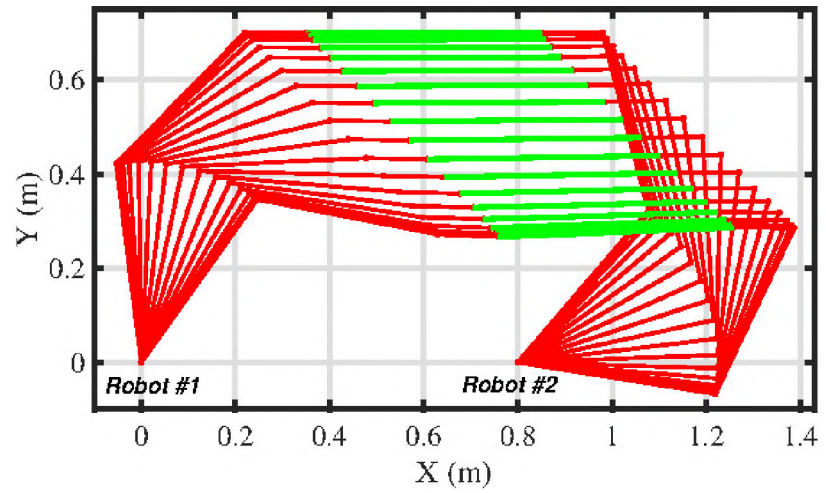


Figure 48: Movement in 2D. Frames are captured in each 0.05 s.

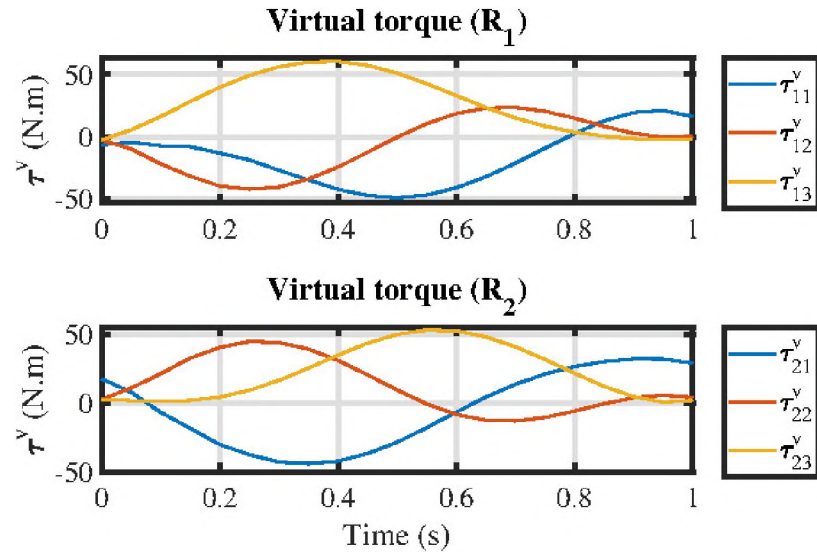


Figure 49: Virtual torques applied to the robots.

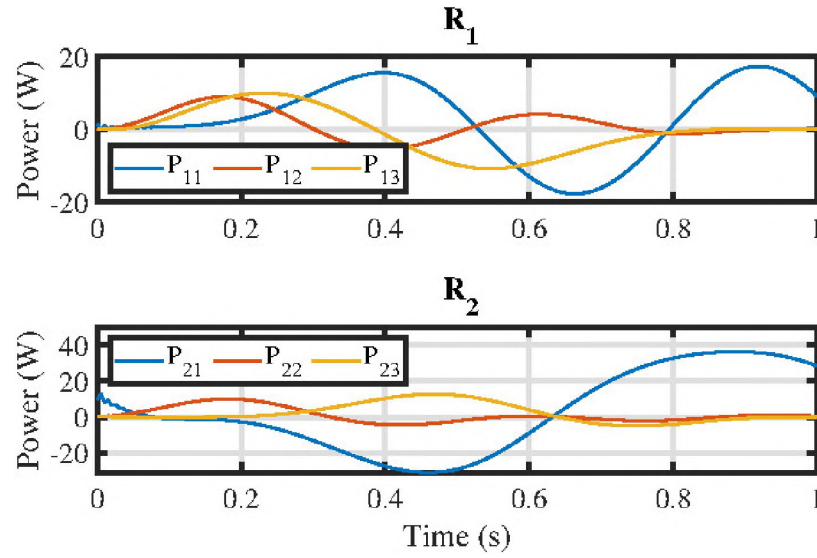


Figure 50: Power in each joint.

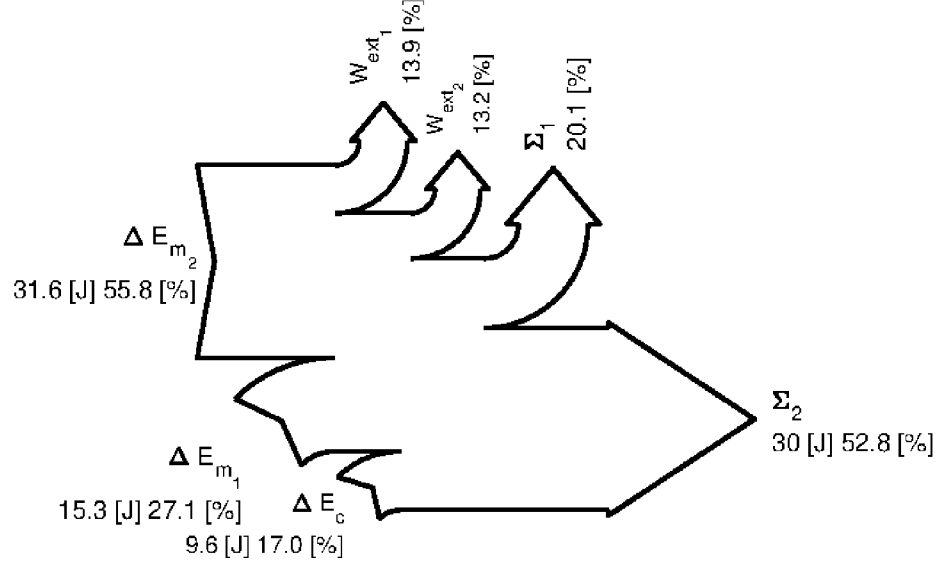


Figure 51: Sankey diagram showing the energy balance for the CRM when following the desired trajectory.

3.10 Concluding Remarks

In this research, a framework is established for controlling cooperative robots and executing the motion task of moving a object along a desired trajectory. A comprehensive model of an augmented dynamics of the robot, JMs and the motors, provides the opportunity to introduce a new control scheme for semi-active joints called virtual control strategy (SVC). Based on SVC, any suitable control approach can be utilized to control the motion task in CRM. Here we used the concept of impedance control to devise the control scheme. The controller was studied and developed for two cases; constant damping and stiffness gains in the impedance relation; and variable gains. For both cases, the input/output passivity tool was used to analysis the stability.

Moreover, an optimization was introduced to obtain an energy-oriented impedance control. The optimization finds the best impedance gains such that the energy extraction from the power source is minimized. Using a simulation example, it was shown that energy regeneration can occur during the motion task, and it has huge effect in terms of energy saving.

The experimental evaluation of this research is left as the future work of this research. Also, another possible future work is to find an energy-optimal path for moving the object from point to point, which requires forming an optimization to find the optimal trajectory.

CHAPTER IV

CONCLUSION

4.1 Statement of Contributions

In this dissertation, we started with the hypothesis of the possibility of energy regeneration in two distinct areas: 1) Robots actuated by BLDC motors, and 2) cooperative robot manipulators. We set three main aims as stated in Section 1.4.

Aim 1: Design a controller based on BLDC motor current regulation.

In chapter II, we extended the framework in [4] to investigate the energy regeneration in BLDC motors. The motion task was defined as following a reference trajectory. First, we obtained the augmented model of the robot-JMs and placed a controller in the control loop to design a desired torque, demanded by the robot, to follow the reference trajectory. Moreover, we introduced the dynamics of the BLDC motor in the d - q frame, which shows the dynamics of the current in each axis of the frame as a function of the input voltage to each axis, using the PWM technique. Furthermore, we assumed an inverter is used to provide the input voltage, and it is connected to an ESE. To model the energy consumption in the ESE, we used the input/output power transmission between the motors and the ESE, assuming the

inverter is ideal. Using the power equality, the energy consumption in the ESE was modeled as a function of the axis currents in the motor and the desired torque. We used an analytical optimization tool, constrained optimization of functional, to find the optimum value of the power consumption with respect to the axis currents. The solution to the optimization was obtained as two quartic polynomials, each containing the solution to the optimal current in each axis. We showed that between the two solutions for each polynomial, only one solution is valid. The proof was introduced in Section 2.3.6. The provided solution could be easily implemented online, using any off-the-shelf inverter.

In this work, we compared the optimal solution with a sub-optimal solution. As we mentioned in Chapter 2, the sub-optimal solution converts the BLDC motor to acts like a DC motor. So, the control objective would be much easier to implement. The answer to the question of if the optimal solution is worth using, depends on the amount of energy that can be saved in comparison to the sub-optimal solution. Theoretically, the optimal solution shows better energy consumption, however, an experiment must be done to verify the theory. Also, in this part, we did not study the stability of the proposed control scheme. The guarantee of stability is an important step in developing new control schemes. It is expected to provide some details regarding the stability.

Publication:

- Ghorbanpour, A., & Richter, H. (2018, September). Control with optimal energy regeneration in robot manipulators driven by brushless dc motors. In Dynamic Systems and Control Conference (Vol. 51890, p. V001T04A003). American Society of Mechanical Engineers.

Aim 2: Design a controller based on BLDC motor voltage regulation.

In chapter II, for the second aim, we investigated the energy regeneration in BLDC motors. The primary objective for this aim was the proof of the concept of designing a motor driver which has superiority compare to an inverter, in terms of energy regeneration. To this end, we used the dynamics of the BLDC motor in the $a-b-c$ frame to establish a relation between the applied voltage to the motor and the current in the motor. Since the induced torque of the motor is a function of the current, hence a function of the applied voltage, we presented the torque as a function of the voltage. By using a motor driver for each phase of the motor, which controls the amount and direction of the applied voltage to the phase, we were able to present the induced torque of the BLDC motor as the function of three motor drivers' command signals, each connected to one phase of the motor. By forming the augmented model of the robot, JMs and, the motors which contain the induced torque of the motor, an SVC methodology was introduced to represent the motor drivers' command signals as the function of virtual control, which seeks the motion objective task. Furthermore, we obtained the energy consumption of the ESE as a function of command signals. Consequently, by optimizing the energy function with respect to the command signals, we could simultaneously optimize the energy and find the commands to the BLDC motors. The concept was tested in the CRML lab and its ability in energy regeneration was compared to an off-the-shelf driver. The introduced motor driver shows better performance in terms of energy regeneration. The results proved our hypothesis that the motor driver can perform better when it comes to energy regeneration. The result of this aim is *the proof of the concept* to design a motor driver.

Even though we presented a method to control BLDC motors, which has the potential to be modified and presented as an off-the-shelf motor drive, there are further investigations that need to be taken to complete the work. First, the method was tested on a simple pendulum. The ability of motor driver should be

tested on more complex dynamical systems, e.g., robot manipulators. Second, the DC motor drives used in this study may not be the best solution to incorporate in the motor driver. The level of inefficiency, accuracy, etc. of the drivers is unknown and their compatibility to support the complex BLDC motor needs more research. We observed phenomenons for which we could not provide a simple explanation. For instance, when the level of voltage in the ultracapacitor is low, energy regeneration occurs more frequently. It was not clear if what we observed was related to the efficiency of the motor driver or the internal structure of the ultracapacitor.

We provided a clear path to introduce a new concept for the BLDC motor driver. There are some questions left for future work which can improve the work. Once the concept is completed and clear details are provided, the proof-of-concept can be converted to a commercialized device.

Publication:

- Ghorbanpour, A., & Richter, H. (2020, October). Energy-Optimal, Direct-Phase Control of Brushless Motors for Robotic Drives. In Dynamic Systems and Control Conference (Vol. 84270, p. V001T05A006). American Society of Mechanical Engineers.
- Ghorbanpour, A., & Richter, H. A Novel Concept for Energy-Optimal, Independent-Phase Control of Brushless Motor Drivers, ASME Letters in Dynamic Systems and Control, (Accepted)

Aim 3: Develop a comprehensive model for CRM and design an impedance-based energy-oriented controller.

In chapter III, we extended the framework previously developed in [4] to study energy regeneration in cooperative robots. We set the motion task objective as moving an object, grasp rigidly by multiple robots, along a desired trajectory. To model the dynamical system, a comprehensive model of the robots' dynamics, all JMs,

and DC actuators was formed. It was assumed that the robots are powered using a single ESE. The SVC control technique was utilized to decouple torque control from actuator control. For torque control and also simultaneously control the motion, an impedance-based controller was chosen. The controller parameters were tuned based on the optimization of ESE energy consumption. The problem demands stability study, which was done using passivity theorem and related theorems for passive systems. In particular, we developed Lemma 1 and Theorem 3 to study the stability of devised controller. Furthermore, we established the theorem for variable impedance control where the damping and stiffness gains of the controller are variable.

The presented work for the third aim in this dissertation is a framework for future development based on the provided materials. Indeed, the system modeling and devising a controller was the hardest part to figure out in our research. It is worth mentioning that, an over actuated dynamical system is usually difficult to model. Also, as we mentioned in the literature review, enormous control methods have been introduced for CRM. Deciding the best control approach, which complies with our main objective of energy minimization, needs more investigation. Even though we provided the fundamental theory, backed by the passivity tool, there are, yet some questions that need to be addressed. For example, the variable impedance gain may not be practical as it is an open-loop solution and vulnerable to uncertainties. This shortcoming can be overcome by providing closed-loop solutions such as Model Predictive Control (MPC).

Publication:

- Ghorbanpour, A., & Richter, H. Energy-Optimal Impedance Control of Cooperative Robot Manipulators, J. Dyn. Sys., Meas., Control., (under review)

4.2 Future Perspectives

In this dissertation, we presented control schemes specifically designed for energy optimization in the robotic systems. We developed an analytical solution for current regulation in BLDC motors, a proof-of-concept study to introduce a motor driver (voltage regulation) for BLDC motors, and a framework for energy-oriented control based on impedance relation in cooperative robots. The research requires further study and evaluation, which we present here.

For the current regulation control of BLDC motor, we assessed the results using MATLAB-SIMULINK. Even though, everything was precisely modeled, e.g., the inverter switches, the study needs further investigations aligned with the presented control scheme. Therefore, the following topics are recommended:

- **Testing the proposed control in the lab.** The next step in verification and validation of the proposed work is applying the controller to an actual robotic system. Because the optimization only requires finding and comparing the roots of polynomials, it can be easily implemented online.
- **Studying the effect of PWM frequency on energy regeneration.** As mentioned before, the PWM sampling time is important as it forms the switching pattern duration, hence affects the parameters in Eqns. (2.5) and (A.2). There is no direct evidence on how the sampling time can change the energy regeneration, so a future topic for studying this problem seems worth investing.

For the voltage regulation, the following topics are recommended:

- **Finding the optimal trajectory.** The solution to the non-quadratic optimization problem in Eqn.(2.46) can be used to find the optimal path in terms of the lowest energy consumption.

- **Modeling the back-emf function.** The back-emf, $f_{ij}(P\theta_{rj}/2)$, in Eqn. (2.30) was modeled as a sinusoidal function in this study. However, studies showed that this function has a shape which is neither sinusoidal nor trapezoidal, as usually utilized in modeling [118]. Since the back-emf is presented in both augmented model and optimization function, therefore an accurate modeling seems to be necessary for achieving better control performance.
- **Improving the internal energy balance equation.** In this study, the internal energy balance was obtained to model the energy change in the ultracapacitor as a function of system states and parameters. The main reason not using any model for the ultracapacitor is the difficulty in the ultracapacitor modeling due to the internal complexity. Therefore, Eqn. (2.41) is an estimation of the energy change in the ultracapacitor. By investing in the modeling of the ultracapacitor, it is possible to obtain more accurate function to optimize. It is also plausible that other criteria, e.g, ultracapacitor impedance, can be used for better energy regeneration. In this regard, studying the conditions when energy regeneration happens, i.e., direction of current is toward the ultracapacitor from the system, seems to be a promising future work.
- **Studying the effect of inverter switching on the ultracapacitor.** As stated in Section 2.3, the inverter applied certain levels of voltage to the motor and the switching causes applying a discontinuous voltage function in time. Therefore, the switching creates a wide bandwidth of ultracapacitor voltage as seen in Fig. 35b. This can be compared with small bandwidth of voltage variation in Fig. 35a. It is not clear how the instantaneous voltage change may affect the capacitor impedance, lifetime, etc. So a study on how switching effect the ultracapacitor seems to be necessary.

- **improving the angular velocity measurement.** In this study, the angular velocity was calculated using a differentiator filter transfer function of the form:

$$T(s) = \frac{s}{1 + \alpha s} \quad (4.1)$$

where $\alpha \ll 1$. This is the simplest and easiest way to calculate the angular velocity from the data of the encoder. Using the filter has the disadvantage of carrying the noises which may cause in motor malfunction since ω_r exist in the optimization and augmented model. It is recommended to use more advance methods such as Kalman filter to eliminate the noise and get the angular velocity as accurate as possible.

Finally, for the cooperative research, the following topics can improve the work and verify the validity of our framework:

- **Experimental verification.** The first and most important future work is implementing the controller in the lab. The developed controller needs force sensor at the end-effectors to measure the applied force/moment by the object to the robots. Also, accurate system identification is required to run the impedance controller.
- **Adaptive control application.** Based on the literature [125], the developed controller has the potential to design an adaptive controller compensating for the uncertainties in the dynamical system.
- **Path planning problem.** A path planning problem to find the optimal path in the sense of minimum energy consumption can be formulated and solved based on the framework introduced in this dissertation. To this end, the work space of cooperative robots needs to be identified. It is possible that cooperation

between robots eliminates singularities in the workspace. However, it needs more investigation.

- **Passivity study.** The passivity theorem can be well-fitted in other researches. The developed Lemma and theorem in chapter 3 are useful tools which can be utilized for studying the stability of other dynamical systems.

BIBLIOGRAPHY

- [1] N. Kularatna and K. Gunawardane, Energy storage devices for electronic systems: rechargeable batteries and supercapacitors. Academic Press, 2021.
- [2] I. Husain, Electric and hybrid vehicles: design fundamentals. CRC press, 2021.
- [3] P. Khalaf and H. Richter, “Trajectory optimization of robots with regenerative drive systems: Numerical and experimental results,” IEEE Transactions on Robotics, vol. 36, no. 2, pp. 501–516, 2019.
- [4] H. Richter, “A framework for control of robots with energy regeneration,” Journal of Dynamic Systems, Measurement, and Control, vol. 137, no. 9, p. 091004, 2015.
- [5] A. Ghorbanpour and H. Richter, “Control with optimal energy regeneration in robot manipulators driven by brushless dc motors,” in ASME 2018 Dynamic Systems and Control Conference, American Society of Mechanical Engineers Digital Collection, 2018.
- [6] P. Khalaf and H. Richter, “Parametric optimization of stored energy in robots with regenerative drive systems,” in Advanced Intelligent Mechatronics (AIM), 2016 IEEE International Conference on, pp. 1424–1429, IEEE, 2016.

- [7] T. Shimizu and C. Underwood, “Super-capacitor energy storage for micro-satellites: Feasibility and potential mission applications,” Acta Astronautica, vol. 85, pp. 138–154, 2013.
- [8] P. Khalaf, H. Warner, E. Hardin, H. Richter, and D. Simon, “Development and experimental validation of an energy regenerative prosthetic knee controller and prototype,” in Dynamic Systems and Control Conference, vol. 51890, p. V001T07A008, American Society of Mechanical Engineers, 2018.
- [9] H. Richter, “Control for optimal energy regeneration from autorotation in uavs,” in 2020 American Control Conference (ACC), pp. 5108–5113, IEEE, 2020.
- [10] X. He, H. Liu, S. He, B. Hu, and G. Xiao, “Research on the energy efficiency of energy regeneration systems for a battery-powered hydrostatic vehicle,” Energy, vol. 178, pp. 400–418, 2019.
- [11] P. Boscaroli and D. Richiedei, “Trajectory design for energy savings in redundant robotic cells,” Robotics, vol. 8, no. 1, p. 15, 2019.
- [12] P. Khalaf and H. Richter, “On global, closed-form solutions to parametric optimization problems for robots with energy regeneration,” Journal of Dynamic Systems, Measurement, and Control, vol. 140, no. 3, 2018.
- [13] H. Richter and D. Selvaraj, “Impedance control with energy regeneration in advanced exercise machines,” in American Control Conference (ACC), 2015, pp. 5890–5895, IEEE, 2015.
- [14] A. Ghorbanpour and H. Richter, “Energy-optimal, direct-phase control of brushless motors for robotic drives,” in Dynamic Systems and Control

- Conference, vol. 84270, p. V001T05A006, American Society of Mechanical Engineers, 2020.
- [15] P. Khalaf and H. Richter, “Trajectory optimization of robots with regenerative drive systems: Numerical and experimental results,” arXiv preprint arXiv:1804.00311, 2018.
 - [16] H. Warner, D. Simon, and H. Richter, “Design optimization and control of a crank-slider actuator for a lower-limb prosthesis with energy regeneration,” in Advanced Intelligent Mechatronics (AIM), 2016 IEEE International Conference on, pp. 1430–1435, IEEE, 2016.
 - [17] G. Khademi, H. Mohammadi, H. Richter, and D. Simon, “Optimal mixed tracking/impedance control with application to transfemoral prostheses with energy regeneration,” IEEE Transactions on Biomedical Engineering, 2017.
 - [18] P. Khalaf, Design, Control, and Optimization of Robots with Advanced Energy Regenerative Drive Systems. PhD thesis, Cleveland State University, 2019.
 - [19] H. Richter, D. Simon, and A. Van Den Bogert, “Semiactive virtual control method for robots with regenerative energy-storing joints,” IFAC Proceedings Volumes, vol. 47, no. 3, pp. 10244–10250, 2014.
 - [20] G. Carabin, E. Wehrle, and R. Vidoni, “A review on energy-saving optimization methods for robotic and automatic systems,” Robotics, vol. 6, no. 4, p. 39, 2017.
 - [21] M. Ehsani, Y. Gao, and A. Emadi, Modern electric, hybrid electric, and fuel cell vehicles: fundamentals, theory, and design. CRC press, 2009.
 - [22] R. Krishnan and S. Lee, “Pm brushless dc motor drive with a new power-converter topology,” IEEE Transactions on Industry applications, vol. 33, no. 4,

pp. 973–982, 1997.

- [23] N. Hemati, J. S. Thorp, and M. C. Leu, “Robust nonlinear control of brushless dc motors for direct-drive robotic applications,” IEEE Transactions on Industrial Electronics, vol. 37, no. 6, pp. 460–468, 1990.
- [24] R. Krishnan, Permanent magnet synchronous and brushless DC motor drives. CRC press, 2017.
- [25] B. Siciliano and O. Khatib, Springer handbook of robotics. Springer, 2016.
- [26] C. Natale, Interaction control of robot manipulators: six degrees-of-freedom tasks, vol. 3. Springer Science & Business Media, 2003.
- [27] R. Bonitz and T. C. Hsia, “Internal force-based impedance control for cooperating manipulators,” IEEE Transactions on Robotics and Automation, vol. 12, no. 1, pp. 78–89, 1996.
- [28] F. Caccavale and L. Villani, “An impedance control strategy for cooperative manipulation,” in Advanced Intelligent Mechatronics, 2001. Proceedings. 2001 IEEE/ASME International Conference on, vol. 1, pp. 343–348, IEEE, 2001.
- [29] A. Koivo and M. Unseren, “Modeling closed chain motion of two manipulators holding a rigid object,” Mechanism and Machine Theory, vol. 25, no. 4, pp. 427–438, 1990.
- [30] J. He, M. Luo, and Q. Zhang, “Dual impedance control with variable object stiffness for the dual-arm cooperative manipulators,” in Intelligent Robot Systems (ACIRS), Asia-Pacific Conference on, pp. 102–108, IEEE, 2016.
- [31] A. Albu-Schaffer, C. Ott, U. Frese, and G. Hirzinger, “Cartesian impedance control of redundant robots: Recent results with the dlr-light-weight-arms,” in

- IEEE International Conference on Robotics and Automation, vol. 3, pp. 3704–3709, IEEE; 1999, 2003.
- [32] A. J. Godfrey and V. Sankaranarayanan, “A new electric braking system with energy regeneration for a bldc motor driven electric vehicle,” Engineering science and technology, an international journal, vol. 21, no. 4, pp. 704–713, 2018.
- [33] J. De Viaene, F. Verbelen, S. Derammelaere, and K. Stockman, “Energy-efficient sensorless load angle control of a bldc motor using sinusoidal currents,” IET Electric Power Applications, vol. 12, no. 9, pp. 1378–1389, 2018.
- [34] P. Khalaf and H. Richter, “Trajectory optimization of robots with regenerative drive systems: Numerical and experimental results,” IEEE Transactions on Robotics, vol. 36, no. 2, pp. 501–516, 2020.
- [35] B. Das, S. Chakrabarti, P. R. Kasari, and A. Chakraborti, “Novel reverse regeneration technique of bldc motor for capacitor charging,” in Proceedings of The 2014 International Conference on Control, Instrumentation, Energy and Communication (CIEC), pp. 246–253, IEEE, 2014.
- [36] P. B. Bobba and K. Rajagopal, “Compact regenerative braking scheme for a pm bldc motor driven electric two-wheeler,” in 2010 Joint International Conference on Power Electronics, Drives and Energy Systems & 2010 Power India, pp. 1–5, IEEE, 2010.
- [37] R. Palanisamy, R. Sahasrabuddhe, M. K. Hiteshkumar, and J. A. Puranik, “A new energy regeneration system for a bldc motor driven electric vehicle,” International Journal of Electrical & Computer Engineering (2088-8708), vol. 11, no. 4, 2021.

- [38] M. Bahrami, H. Mokhtari, and A. Dindar, “Energy regeneration technique for electric vehicles driven by a brushless dc motor,” IET Power Electronics, vol. 12, no. 13, pp. 3397–3402, 2019.
- [39] F. Naseri, E. Farjah, and T. Ghanbari, “An efficient regenerative braking system based on battery/supercapacitor for electric, hybrid, and plug-in hybrid electric vehicles with bldc motor,” IEEE Transactions on Vehicular Technology, vol. 66, no. 5, pp. 3724–3738, 2016.
- [40] Y. Feng, J. Mai, S. K. Agrawal, and Q. Wang, “Energy regeneration from electromagnetic induction by human dynamics for lower extremity robotic prostheses,” IEEE Transactions on Robotics, vol. 36, no. 5, pp. 1442–1451, 2020.
- [41] R. Romeu, “Flight control through vectored propulsion,” in 2018 AIAA Aerospace Sciences Meeting, p. 0765, 2018.
- [42] S. De, M. Rajne, S. Poosapati, C. Patel, and K. Gopakumar, “Low-inductance axial flux bldc motor drive for more electric aircraft,” IET Power Electronics, vol. 5, no. 1, pp. 124–133, 2012.
- [43] R. R. Glasscock, Design, modelling and measurement of hybrid powerplant for unmanned aerial vehicles (UAVs). PhD thesis, Queensland University of Technology, 2012.
- [44] H. Xu and Y. Jani, “Understanding sensorless vector control for brushless dc motors,” in IEEE Embedded Systems Conference Silicon Valley, pp. 3–22, Cite-seer, 2008.
- [45] H. Abu-Rub, A. Iqbal, and J. Guzinski, High performance control of AC drives with MATLAB/Simulink models. John Wiley & Sons, 2012.

- [46] P. Pillay and R. Krishnan, “Modeling, simulation, and analysis of permanent-magnet motor drives. ii. the brushless dc motor drive,” IEEE transactions on Industry applications, vol. 25, no. 2, pp. 274–279, 1989.
- [47] J. Joy and S. Ushakumari, “Regenerative braking mode operation of a three-phase h-bridge inverter fed pmbldc motor generator drive in an electric bike,” Electric Power Components and Systems, pp. 1–19, 2018.
- [48] F. Yacef, N. Rizoug, O. Bouhali, and M. Hamerlain, “Optimization of energy consumption for quadrotor uav,” in Proceedings of the International Micro Air Vehicle Conference and Flight Competition (IMAV), Toulouse, France, pp. 18–21, 2017.
- [49] M. D. Zivanovic and M. Vukobratovic, Multi-arm cooperating robots: dynamics and control, vol. 30. Springer Science & Business Media, 2006.
- [50] A. Koivo and M. Unseren, “Reduced order model and decoupled control architecture for two manipulators holding a rigid object,” Journal of dynamic systems, measurement, and control, vol. 113, no. 4, pp. 646–654, 1991.
- [51] P. Chiacchio, S. Chiaverini, and B. Siciliano, “Cooperative control schemes for multiple robot manipulator systems,” in Proceedings 1992 IEEE International Conference on Robotics and Automation, pp. 2218–2223, IEEE, 1992.
- [52] H. Cheng, Y.-K. Yiu, and Z. Li, “Dynamics and control of redundantly actuated parallel manipulators,” IEEE/ASME Transactions on mechatronics, vol. 8, no. 4, pp. 483–491, 2003.
- [53] M. H. Korayem and S. R. Nekoo, “Nonlinear suboptimal sdre controller for cooperative manipulators to increase dynamic load carrying capacity,” in

- Robotics and Mechatronics (ICROM), 2015 3rd RSI International Conference on, pp. 019–024, IEEE, 2015.
- [54] S. Li, S. Chen, B. Liu, Y. Li, and Y. Liang, “Decentralized kinematic control of a class of collaborative redundant manipulators via recurrent neural networks,” Neurocomputing, vol. 91, pp. 1–10, 2012.
- [55] F. Ficuciello, A. Romano, L. Villani, and B. Siciliano, “Cartesian impedance control of redundant manipulators for human-robot co-manipulation,” in 2014 IEEE/RSJ International Conference on Intelligent Robots and Systems, pp. 2120–2125, IEEE, 2014.
- [56] H. Cheng, G. Liu, Y. Yiu, Z. Xiong, and Z. Li, “Advantages and dynamics of parallel manipulators with redundant actuation,” in Proceedings 2001 IEEE/RSJ International Conference on Intelligent Robots and Systems. Expanding the Societal Role of Robotics in the the Next Millennium (Cat. No. 01CH37180), vol. 1, pp. 171–176, IEEE, 2001.
- [57] S. B. Moon and S. Ahmad, “Time scaling of cooperative multirobot trajectories,” IEEE transactions on systems, man, and cybernetics, vol. 21, no. 4, pp. 900–908, 1991.
- [58] Y. Zhou, “Dynamic model and force control for two manipulators handling a pin-jointed object,” in [1991] Proceedings of the 30th IEEE Conference on Decision and Control, pp. 2763–2768, IEEE, 1991.
- [59] S.-S. You and S.-K. Jeong, “Kinematics and dynamic modeling for holonomic constrained multiple robot systems through principle of workspace orthogonalization,” KSME International Journal, vol. 12, no. 2, pp. 170–180, 1998.

- [60] W. Gueaieb, F. Karray, and S. Al-Sharhan, “Computational intelligence based approach for the joint trajectory generation of cooperative robotic systems,” Systems Analysis Modelling Simulation, vol. 42, no. 10, pp. 1499–1520, 2002.
- [61] T. Tarn, A. Bejczy, and X. Yun, “Design of dynamic control of two cooperating robot arms: Closed chain formulation,” in Robotics and Automation. Proceedings. 1987 IEEE International Conference on, vol. 4, pp. 7–13, IEEE, 1987.
- [62] R. G. Bonitz and T. C. Hsia, “Force decomposition in cooperating manipulators using the theory of metric spaces and generalized inverses,” in Proceedings of the 1994 IEEE International Conference on Robotics and Automation, pp. 1521–1527, IEEE, 1994.
- [63] Y. Ren, Y. Zhou, Y. Liu, M. Jin, and H. Liu, “Adaptive object impedance control of dual-arm cooperative humanoid manipulators,” in Proceeding of the 11th World Congress on Intelligent Control and Automation, pp. 3333–3339, IEEE, 2014.
- [64] D. Heck, D. Kostić, A. Denasi, and H. Nijmeijer, “Internal and external force-based impedance control for cooperative manipulation,” in 2013 European Control Conference (ECC), pp. 2299–2304, IEEE, 2013.
- [65] H. Kawasaki, S. Ito, and R. B. Ramli, “Adaptive decentralized coordinated control of multiple robot arms,” IFAC Proceedings Volumes, vol. 36, no. 17, pp. 387–392, 2003.
- [66] F. Xu, J. Wang, and G.-d. Lu, “Adaptive robust neural control of a two-manipulator system holding a rigid object with inaccurate base frame param-

- eters,” Frontiers of Information Technology & Electronic Engineering, vol. 19, no. 11, pp. 1316–1327, 2018.
- [67] P. Esmaili and H. Haron, “Adaptive synchronous artificial neural network based pi-type sliding mode control on two robot manipulators,” in Computer, Communications, and Control Technology (I4CT), 2015 International Conference on, pp. 515–519, IEEE, 2015.
- [68] J. Pliego-Jimenez and M. Arteaga-Perez, “On the adaptive control of cooperative robots with time-variant holonomic constraints,” International Journal of Adaptive Control and Signal Processing, vol. 31, no. 8, pp. 1217–1231, 2017.
- [69] Y. Jiang, Z. Liu, C. Chen, and Y. Zhang, “Adaptive robust fuzzy control for dual arm robot with unknown input deadzone nonlinearity,” Nonlinear Dynamics, vol. 81, no. 3, pp. 1301–1314, 2015.
- [70] J.-F. Liu and K. Abdel-Malek, “Robust control of planar dual-arm cooperative manipulators,” Robotics and Computer-Integrated Manufacturing, vol. 16, no. 2, pp. 109–119, 2000.
- [71] M. Li, K. Li, P. Wang, Y. Liu, F. Zha, and W. Guo, “Indirect adaptive impedance control for dual-arm cooperative manipulation,” in 2017 2nd International Conference on Advanced Robotics and Mechatronics (ICARM), pp. 650–655, IEEE, 2017.
- [72] A. Rodríguez-Angeles, R. Portillo-Vélez, and C. Cruz-Villar, “An optimal admittance reactive force control for cooperative robot grasping tasks,” in Proceedings of the 8th International Conference on Informatics in Control Automation and Robotics (ICINCO’11), pp. 50–58, 2011.

- [73] S. A. Schneider and R. H. Cannon, “Object impedance control for cooperative manipulation: Theory and experimental results,” IEEE Transactions on Robotics and Automation, vol. 8, no. 3, pp. 383–394, 1992.
- [74] R. Monfaredi, S. M. Rezaei, and A. Talebi, “A new observer-based adaptive controller for cooperative handling of an unknown object,” Robotica, vol. 34, no. 7, pp. 1437–1463, 2016.
- [75] E. Mehrabi, H. A. Talebi, M. Zareinejad, and I. Sharifi, “Cooperative control of manipulator robotic systems with unknown dynamics,” in Advanced Robotics (ICAR), 2015 International Conference on, pp. 401–406, IEEE, 2015.
- [76] R. Mohajerpoor, M. Rezaei, A. Talebi, M. Noorhosseini, and R. Monfaredi, “A robust adaptive hybrid force/position control scheme of two planar manipulators handling an unknown object interacting with an environment,” Proceedings of the Institution of Mechanical Engineers, Part I: Journal of Systems and Control Engineering, vol. 226, no. 4, pp. 509–522, 2012.
- [77] S. Erhart and S. Hirche, “Internal force analysis and load distribution for cooperative multi-robot manipulation,” IEEE Transactions on Robotics, vol. 31, no. 5, pp. 1238–1243, 2015.
- [78] Y. Nakamura, K. Nagai, and T. Yoshikawa, “Mechanics of coordinative manipulation by multiple robotic mechanisms,” Journal of the Robotics Society of Japan, vol. 4, no. 5, pp. 489–498, 1986.
- [79] M. A. Unseren, “Determination of contact forces for two manipulators mutually lifting a rigid object using a technique of dynamic load distribution,” Intelligent Automation & Soft Computing, vol. 2, no. 1, pp. 49–63, 1996.

- [80] I. D. Walker, S. I. Marcus, and R. A. Freeman, “Distribution of dynamic loads for multiple cooperating robot manipulators,” Journal of Robotic Systems, vol. 6, no. 1, pp. 35–47, 1989.
- [81] I. D. Walker, R. A. Freeman, and S. I. Marcus, “Analysis of motion and internal loading of objects grasped by multiple cooperating manipulators,” The International journal of robotics research, vol. 10, no. 4, pp. 396–409, 1991.
- [82] H. Kawasaki, S. Ueki, and S. Ito, “Decentralized adaptive coordinated control of multiple robot arms without using a force sensor,” Automatica, vol. 42, no. 3, pp. 481–488, 2006.
- [83] N. Hogan, “Impedance control: An approach to manipulation,” in American Control Conference, 1984, pp. 304–313, IEEE, 1984.
- [84] M. Shimizu, “Nonlinear impedance control to maintain robot position within specified ranges,” in 2012 Proceedings of SICE Annual Conference (SICE), pp. 1287–1292, IEEE, 2012.
- [85] H. F. Al-Shuka, S. Leonhardt, W.-H. Zhu, R. Song, C. Ding, and Y. Li, “Active impedance control of bioinspired motion robotic manipulators: An overview,” Applied bionics and biomechanics, vol. 2018, 2018.
- [86] F. Caccavale, P. Chiacchio, A. Marino, and L. Villani, “Six-dof impedance control of dual-arm cooperative manipulators,” IEEE/ASME Transactions On Mechatronics, vol. 13, no. 5, pp. 576–586, 2008.
- [87] J. Szewczyk, F. Plumet, and P. Bidaud, “Planning and controlling cooperating robots through distributed impedance,” Journal of Robotic Systems, vol. 19, no. 6, pp. 283–297, 2002.

- [88] S. Erhart, D. Sieber, and S. Hirche, “An impedance-based control architecture for multi-robot cooperative dual-arm mobile manipulation,” in Intelligent Robots and Systems (IROS), 2013 IEEE/RSJ International Conference on, pp. 315–322, IEEE, 2013.
- [89] A. Stolfi, P. Gasbarri, and M. Sabatini, “A combined impedance-pd approach for controlling a dual-arm space manipulator in the capture of a non-cooperative target,” Acta Astronautica, vol. 139, pp. 243–253, 2017.
- [90] S. Schneider and R. H. Cannon, “Object impedance control for cooperative manipulation: Theory and experimental results,” in 1989 IEEE International Conference on Robotics and Automation, pp. 1076–1077, IEEE Computer Society, 1989.
- [91] Y. Kishi, Z. W. Luo, F. Asano, and S. Hosoe, “Passive impedance control with time-varying impedance center,” in Proceedings 2003 IEEE International Symposium on Computational Intelligence in Robotics and Automation. Computational Intelligence in Robotics and Automation for the New Millennium (Cat. No. 03EX694), vol. 3, pp. 1207–1212, IEEE, 2003.
- [92] F. Ferraguti, C. Secchi, and C. Fantuzzi, “A tank-based approach to impedance control with variable stiffness,” in 2013 IEEE International Conference on Robotics and Automation, pp. 4948–4953, IEEE, 2013.
- [93] M. Zheng, T. Yuan, and T. Huang, “Time-varying impedance control of port hamiltonian system with a new energy-storing tank,” Complexity, vol. 2018, 2018.
- [94] C. Li, Z. Zhang, G. Xia, X. Xie, and Q. Zhu, “Efficient force control learning system for industrial robots based on variable impedance control,” Sensors,

vol. 18, no. 8, p. 2539, 2018.

- [95] J. Buchli, F. Stulp, E. Theodorou, and S. Schaal, “Learning variable impedance control,” The International Journal of Robotics Research, vol. 30, no. 7, pp. 820–833, 2011.
- [96] J. Duan, Y. Gan, M. Chen, and X. Dai, “Adaptive variable impedance control for dynamic contact force tracking in uncertain environment,” Robotics and Autonomous Systems, vol. 102, pp. 54–65, 2018.
- [97] Y. Dong and B. Ren, “Ude-based variable impedance control of uncertain robot systems,” IEEE Transactions on Systems, Man, and Cybernetics: Systems, 2017.
- [98] L. Rozo, D. Bruno, S. Calinon, and D. G. Caldwell, “Learning optimal controllers in human-robot cooperative transportation tasks with position and force constraints,” in 2015 IEEE/RSJ international conference on intelligent robots and systems (IROS), pp. 1024–1030, IEEE, 2015.
- [99] R. Wang, J. Zhang, and Z. Qiu, “Optimal impedance control for an elbow rehabilitation robot,” in 2017 14th International Conference on Ubiquitous Robots and Ambient Intelligence (URAI), pp. 388–392, IEEE, 2017.
- [100] R. Ikeura, T. Moriguchi, and K. Mizutani, “Optimal variable impedance control for a robot and its application to lifting an object with a human,” in Proceedings. 11th IEEE International Workshop on Robot and Human Interactive Communication, pp. 500–505, IEEE, 2002.
- [101] K. Kronander and A. Billard, “Stability considerations for variable impedance control,” IEEE Transactions on Robotics, vol. 32, no. 5, pp. 1298–1305, 2016.

- [102] J.-H. Jean and L.-C. Fu, “An adaptive control scheme for coordinated multi-manipulator systems,” IEEE Transactions on Robotics and Automation, vol. 9, no. 2, pp. 226–231, 1993.
- [103] S. Erhart and S. Hirche, “Adaptive force/velocity control for multi-robot cooperative manipulation under uncertain kinematic parameters,” in Intelligent Robots and Systems (IROS), 2013 IEEE/RSJ International Conference on, pp. 307–314, IEEE, 2013.
- [104] Y. Wang, Z. Liu, and Y. Zhang, “Adaptive jacobian coordinated manipulation for multiple robot manipulators,” in Control and Decision Conference (CCDC), 2016 Chinese, pp. 1342–1347, IEEE, 2016.
- [105] B. Esakki and S. R. Ahmed, “Dynamics and control of collaborative robot manipulators,” in Smart Technologies and Management for Computing, Communication, Controls, Energy and Materials (ICSTM), 2015 International Conference on, pp. 590–595, IEEE, 2015.
- [106] M. Farahmandrad, S. Ganjefar, H. A. Talebi, and M. Bayati, “Fuzzy sliding mode controller design for a cooperative robotic system with uncertainty for handling an object,” Journal of Dynamic Systems, Measurement, and Control, vol. 141, no. 6, p. 061010, 2019.
- [107] B. Baigzadehnoe, Z. Rahmani, A. Khosravi, and B. Rezaie, “On position/force tracking control problem of cooperative robot manipulators using adaptive fuzzy backstepping approach,” ISA transactions, vol. 70, pp. 432–446, 2017.
- [108] S. Li, J. He, Y. Li, and M. U. Rafique, “Distributed recurrent neural networks for cooperative control of manipulators: A game-theoretic perspective,” IEEE

- transactions on neural networks and learning systems, vol. 28, no. 2, pp. 415–426, 2017.
- [109] M. H. Korayem and S. R. Nekoo, “Controller design of cooperative manipulators using state-dependent riccati equation,” Robotica, vol. 36, no. 4, pp. 484–515, 2018.
- [110] Y. Zheng and J. Luh, “Joint torques for control of two coordinated moving robots,” in Proceedings. 1986 IEEE International Conference on Robotics and Automation, vol. 3, pp. 1375–1380, IEEE, 1986.
- [111] M. W. Spong, S. Hutchinson, and M. Vidyasagar, Robot modeling and control, vol. 3. Wiley New York, 2006.
- [112] A. B. Plunkett, “Field orientation control of a permanent magnet motor,” Mar. 21 1989. US Patent 4,814,677.
- [113] P. Khalaf and H. Richter, “On global, closed-form solutions to parametric optimization problems for robots with energy regeneration,” Journal of Dynamic Systems, Measurement, and Control, 2017.
- [114] D. E. Kirk, Optimal control theory: an introduction. Courier Corporation, 2012.
- [115] E. Rees, “Graphical discussion of the roots of a quartic equation,” The American Mathematical Monthly, vol. 29, no. 2, pp. 51–55, 1922.
- [116] V. M. Hernández-Guzmán and J. Orrante-Sakanassi, “Pid control of robot manipulators actuated by bldc motors,” International Journal of Control, pp. 1–10, 2019.

- [117] M. P. Belov, T. D. Khoa, and D. D. Truong, “Blde of robotic manipulators with neural torque compensator based optimal robust control,” in 2019 IEEE Conference of Russian Young Researchers in Electrical and Electronic Engineering (EIconRus), pp. 437–441, IEEE, 2019.
- [118] M. Johansson, “Evaluation of sensor solutions & motor speed control methods for bldcm/pmsm in aerospace applications,” 2017.
- [119] Y. Kim, N. Chang, Y. Wang, and M. Pedram, “Maximum power transfer tracking for a photovoltaic-supercapacitor energy system,” in Proceedings of the 16th ACM/IEEE international symposium on Low power electronics and design, pp. 307–312, 2010.
- [120] J. Krüger, G. Schreck, and D. Surdilovic, “Dual arm robot for flexible and cooperative assembly,” CIRP annals, vol. 60, no. 1, pp. 5–8, 2011.
- [121] A. J. Van der Schaft and A. Van Der Schaft, L2-gain and passivity techniques in nonlinear control, vol. 2. Springer, 2000.
- [122] M. Vidyasagar, Nonlinear systems analysis. SIAM, 2002.
- [123] R. Ortega, J. A. L. Perez, P. J. Nicklasson, and H. J. Sira-Ramirez, Passivity-based control of Euler-Lagrange systems: mechanical, electrical and electromechanical applications. Springer Science & Business Media, 2013.
- [124] B. Brogliato, R. Lozano, B. Maschke, O. Egeland, et al., “Dissipative systems analysis and control,” Theory and Applications, vol. 2, 2007.
- [125] R. Kelly, R. Carelli, and R. Ortega, “Adaptive motion control design of robot manipulators: An input-output approach,” International Journal of Control, vol. 50, no. 6, pp. 2563–2581, 1989.

- [126] S. Briot, W. Khalil, et al., “Dynamics of parallel robots,” From rigid bodies to flexible elements. Springer, 2015.
- [127] N. Hogan, “Impedance Control: An Approach to Manipulation: Part I—Theory,” Journal of Dynamic Systems, Measurement, and Control, vol. 107, pp. 1–7, 03 1985.
- [128] N. Hogan, “Impedance Control: An Approach to Manipulation: Part II—Implementation,” Journal of Dynamic Systems, Measurement, and Control, vol. 107, pp. 8–16, 03 1985.
- [129] R. Johansson and M. W. Spong, “Quadratic optimization of impedance control,” in Proceedings of the 1994 IEEE International Conference on Robotics and Automation, pp. 616–621, IEEE, 1994.
- [130] M. Vukobratović, “How to control robots interacting with dynamic environment,” Journal of Intelligent and Robotic Systems, vol. 19, no. 2, pp. 119–152, 1997.
- [131] J. R. Forbes and C. J. Damaren, “Passive linear time-varying systems: State-space realizations, stability in feedback, and controller synthesis,” in Proceedings of the 2010 American Control Conference, pp. 1097–1104, IEEE, 2010.

APPENDIX A

OUTLINE OF SPACE VECTOR PULSE WIDTH MODULATION

Note that the space vector pulse width modulation (SVPWM) is done in $\alpha\beta$ frame. Given a set of desired voltages, the SVPWM technique calculates the optimum switching pattern to ensure that the desired voltages are obtained at the output of the inverter. The state of each switch, i.e. on/off position, and the time period for each position are to be determined [45]. Note that it suffices to calculate the on/off states of only three switches, since they are paired. To implement SVPWM, the first step is to use Park's transformation, Eqn.2.8, where the desired abc frame voltages, i.e. v_A^*, v_B^* and v_C^* , can be transformed to dq frame to obtain V_q^* and V_d^* . In the dq frame, the magnitude, $|V^*|$, and angle, $\angle V^*$, relative to the d-axis of a desired voltage vector, V^* , can be obtained using:

$$|V^*| = \sqrt{V_q^{*2} + V_d^{*2}} \quad , \quad \angle V^* = \text{atan}(V_q^*/V_d^*) \quad (\text{A.1})$$

The vector of V^* is defined in dq space and SVPWM can generate it based on its location. The dq space is divided into six equal regions shown in Fig. 52. In this figure, vectors $V_k, k \in \{0, 1, \dots, 7\}$, are obtained from combinations of switches. There are eight different combinations, shown in Table VIII where each combination is represented with a vector. For example V_0 can be achieved if switches 4,6 and 2 are ON and 1,3 and 6 are OFF which makes A,B and C parameters equal to zero. Space vectors $V_k, k \in \{1, \dots, 6\}$ are called active state vectors and V_0, V_7 are called zero state vectors. Since zero state vectors represent zero output voltage, they are located in the origin but active vectors each produce some level of V_{dc} that can be calculated from Eqn. 2.5.

As an example, assume that V^* is located in section I as shown in Fig. 52.

Table VIII: Switching States

Switching state (ABC)	ON switches	Voltage space vector
000	4-6-2	V_0
100	1-6-2	V_1
110	1-3-2	V_2
010	4-3-2	V_3
011	4-3-5	V_4
001	4-6-5	V_5
101	1-6-5	V_6
111	1-3-5	V_7

This vector can be synthesized by using the nearest two neighboring active vectors and zero vectors. For this case, V^* can be synthesized by V_1 , V_2 , V_0 and V_7 . It should be noted that to minimize the switching frequency, both zero state vectors should be used [45]. Having the desired voltage vector and its location, and from the fact that it can be produced with these four vectors, the next step is to assign an appropriate time period for each state vector. This can be done using the *equal volt-second principle* [2]. Based on this principle, the product of the desired voltage and switching time, T_s , must be equal to the product of the applied voltage vectors and their application time, assuming that the desired voltage remains fixed during the switching interval T_s [45]. If the desired voltage vector is located in sector k , then V_k , V_{k+1} , V_0 and V_7 are the assigned output voltage states for a period of T_s . Note that for section VI assigned output voltage states are V_6 , V_1 , V_0 and V_7 . It can be shown that the sequence of assigned voltage state vectors for each sector is made according to Fig. 53 [2]. Based on this figure, synthesis always starts with V_0 for $T_0/2$ of time, then V_k is active for $T_k/2$ of time and then V_{k+1} for $T_{k+1}/2$ time. The value of V_k and V_{k+1} can be found from Table VIII. After these two active vectors, V_7 is active for T_7 seconds. The sequence continues with V_{k+1} , V_k and V_0 , forming a symmetric shape shown in Fig. 53.

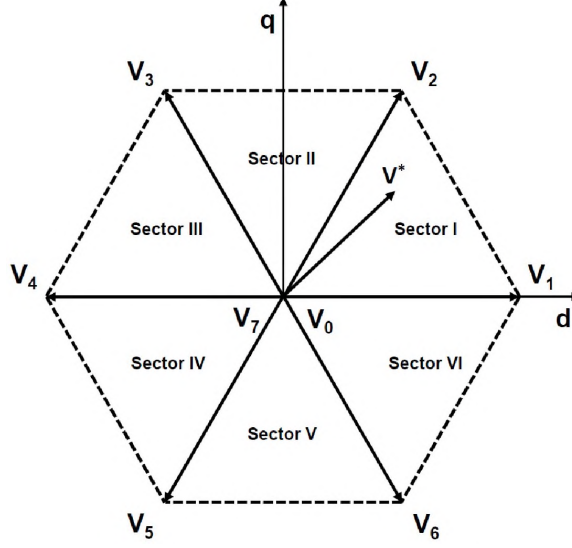


Figure 52: Voltage space vector locations corresponding to different switching states.

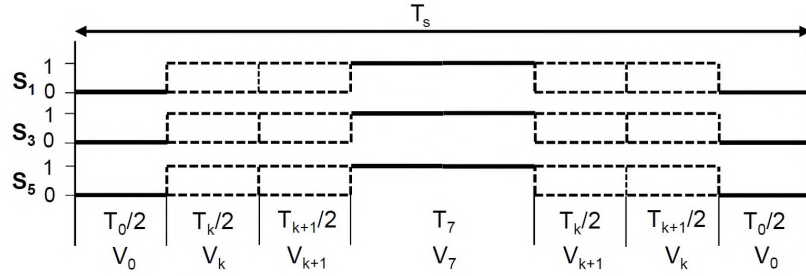


Figure 53: Diagram of switching pattern for SVPWM [2].

$$\begin{bmatrix} T_k \\ T_{k+1} \end{bmatrix} = \frac{\sqrt{3}T_s}{V_s} \begin{bmatrix} \sin(\frac{k\pi}{3}) & -\cos(\frac{k\pi}{3}) \\ -\sin(\frac{(k-1)\pi}{3}) & \cos(\frac{(k-1)\pi}{3}) \end{bmatrix} \begin{bmatrix} V_d^* \\ V_q^* \end{bmatrix} \quad (\text{A.2})$$

$$\begin{bmatrix} T_0 \\ T_7 \end{bmatrix} = \frac{1}{2} \begin{bmatrix} T_s - T_k - T_{k+1} \\ T_s - T_k - T_{k+1} \end{bmatrix}$$

The effective times of each space vector can be calculated from Eqn. A.2, where k is the sector number. Having the active time of each vector and assigning a suitable sampling period, an output voltage is generated that follows the reference input.

APPENDIX B

EXTERNAL ENERGY BALANCE IN ROBOT ACTUATED BY BRUSHLESS DC MOTORS

We start by obtaining Joule losses in terms of the virtual control. The Joule losses due to resistance in the BLDC motor of j th semi-active joint (L_{R_j}) can be obtained from:

$$L_{R_j} = R_j \mathbf{I}_j^T \mathbf{I}_j \quad (\text{B.1})$$

By substituting the current with voltage and back-emf from Eqns. (2.29) and using Eqns. (2.30), (2.32), and (3.26) to present the Joule loss as a function of the virtual control, after some manipulation and simplification, we get:

$$L_{R_j} = \frac{V_s^2}{R_j} \mathbf{r}_j^T \mathbf{r}_j + \frac{\lambda_j^2 \eta_j^2 \dot{q}_j^2}{R_j} \mathbf{f}_j^T \mathbf{f}_j - 2\mathcal{T}_j^v \dot{q}_j \quad (\text{B.2})$$

By taking the integral of both sides for the time interval $[t_1, t_2]$, the following equation can be obtained directly:

$$\int_{t_1}^{t_2} \left\{ -L_{R_j} + \frac{\lambda_j^2 \eta_j^2 \dot{q}_j^2}{R_j} \mathbf{f}_j^T \mathbf{f}_j - \mathcal{T}_j^v \dot{q}_j \right\} dt = \int_{t_1}^{t_2} \left\{ \mathcal{T}_j^v \dot{q}_j - \frac{V_s^2}{R_j} \mathbf{r}_j^T \mathbf{r}_j \right\} dt \quad (\text{B.3})$$

In the view of Eqns. (2.41) and (3.26), we can write:

$$\Delta E_s = \sum_{j=1}^n \Delta E_{s_j} \quad (\text{B.4})$$

where

$$\Delta E_{s_j} = \int_{t_1}^{t_2} \left\{ \mathcal{T}_j^v \dot{q}_j - \frac{V_s^2}{R_j} \mathbf{r}_j^T \mathbf{r}_j \right\} dt \quad (\text{B.5})$$

Equation (B.5) can be obtained by substituting Eqns. (2.30, 3.26) in Eqn. (2.41).

From Eqn. (B.3) and Eqn. (B.5) the following equation can be resulted:

$$\Delta E_{s_j} = \int_{t_1}^{t_2} \{-L_{R_j} + \frac{\lambda_j^2 \eta_j^2 \dot{q}_j^2}{R_j} \mathbf{f}_j^T \mathbf{f}_j - \mathcal{T}_j^v \dot{q}_j\} dt \quad (\text{B.6})$$

Also, from Eqns. (3.13, 3.26), the relationship between τ_j and \mathcal{T}_j^v can be expressed as¹:

$$\tau_j = -m_j \eta_j^2 \ddot{q}_j - (b_j \eta_j^2 + \frac{\lambda_j^2 \eta_j^2}{R_j} \mathbf{f}_j^T \mathbf{f}_j) \dot{q}_j + \mathcal{T}_j^v \quad (\text{B.7})$$

Multiplying both sides of this equation by \dot{q}_j yields:

$$\tau_j \dot{q}_j = -m_j \eta_j^2 \ddot{q}_j \dot{q}_j - (b_j \eta_j^2 + \frac{\lambda_j^2 \eta_j^2}{R_j} \mathbf{f}_j^T \mathbf{f}_j) \dot{q}_j^2 + \mathcal{T}_j^v \dot{q}_j \quad (\text{B.8})$$

The kinetic energy of the actuator is expressed as $K_j = \frac{1}{2} m_j \eta_j^2 \dot{q}_j^2$. So by taking the integral of both sides of Eqn. (B.8), below equation is obtained:

$$\int_{t_1}^{t_2} \{\tau_j \dot{q}_j\} dt = \int_{t_1}^{t_2} \{-\frac{dK_j}{dt} - (b_j \eta_j^2 + \frac{\lambda_j^2 \eta_j^2}{R_j} \mathbf{f}_j^T \mathbf{f}_j) \dot{q}_j^2 + \mathcal{T}_j^v \dot{q}_j\} dt \quad (\text{B.9})$$

Finally, using Eqn. (B.9, B.6) we can conclude:

$$\int_{t_1}^{t_2} \tau_j \dot{q}_j dt = -\Delta E_{s_j} - \int_{t_1}^{t_2} L_{R_j} dt - \int_{t_1}^{t_2} \{\frac{dK_j}{dt} + b_j \eta_j^2 \dot{q}_j^2\} dt \quad (\text{B.10})$$

To derive Eqn. (2.42), we start by writing the overall energy balance for the robotic manipulator:

$$\int_{t_1}^{t_2} (\sum_{j=1}^n \tau_j \dot{q}_j) dt = \Delta E_m^\circ + \Sigma_m^\circ \quad (\text{B.11})$$

where the term on the left hand side is the work done by the semi-active joints, ΔE_m° is the change in mechanical energy, and Σ_m° is the dissipated mechanical energy in

¹Note that $\tau = [\tau_1, \dots, \tau_n]^T$

the system. Replacing semi-active joints work by Eqn. (B.10), results:

$$\Delta E_m^T + \Sigma_m^T + \Sigma_e + \Delta E_s = 0 \quad (\text{B.12})$$

where

$$\begin{aligned} \Delta E_m^T &= \Delta E_m^\circ + \sum_{j=1}^n \Delta K_j \\ \Sigma_m^T &= \Sigma_m^\circ + \sum_{j=1}^n \int_{t_1}^{t_2} b_j \eta_j^2 \dot{q}_j^2 dt \\ \Sigma_e &= \sum_{j=1}^n \int_{t_1}^{t_2} L_{R_j} dt \end{aligned} \quad (\text{B.13})$$

The total mechanical energy change and the mechanical losses of the robot can be determined based on the system's states and parameters. The change in the charge of the supercapacitor can be easily measured using the voltage value at its terminal. Finally, the Joule loss is a function of resistance and current. The resistance is an available parameter and current can be measured using current sensor.

APPENDIX C

EXTERNAL ENERGY BALANCE IN COOPERATIVE ROBOT
MANIPULATORS

We start by obtaining Joule losses in terms of the desired control. The Joule losses due to resistance in motor of ij th semi-active joint is:

$$L_{R_{ij}} = R_{ij} I_{ij}^2 \quad (\text{C.1})$$

Substituting current and u_{ij} from Eqns. (3.14) and (3.26), respectively, and after some manipulation and simplification, we get:

$$L_{R_{ij}} = \frac{R_{ij}}{a_{ij}^2} (\tau_{ij}^v)^2 + \frac{a_{ij}^2 \dot{q}_{ij}^2}{R_{ij}} - 2\tau_{ij}^v \dot{q}_{ij} \quad (\text{C.2})$$

Eqn. (3.15) expresses the relation between τ_{ij} and τ_{ij}^v . Multiplying both sides of this equation by \dot{q}_{ij} yields:

$$\tau_{ij} \dot{q}_{ij} = -m_{ij} \bar{n}_{ij}^2 \ddot{q}_{ij} \dot{q}_{ij} - (b_{ij} \bar{n}_{ij}^2 + \frac{a_{ij}^2}{R_{ij}}) \dot{q}_{ij}^2 + \tau_{ij}^v \dot{q}_{ij} \quad (\text{C.3})$$

The kinetic energy of the actuator is expressed as $K_{ij} = \frac{1}{2} I_{ij} \bar{n}_{ij}^2 \dot{q}_{ij}^2$. So Eqn. (C.3) can be simplified as:

$$\tau_{ij} \dot{q}_{ij} = -\frac{dK_{ij}}{dt} - (b_{ij} \bar{n}_{ij}^2 + \frac{a_{ij}^2}{R_{ij}}) \dot{q}_{ij}^2 + \tau_{ij}^v \dot{q}_{ij} \quad (\text{C.4})$$

Replacing $a_{ij}^2 \dot{q}_{ij} / R_{ij}$ from Eqn. (C.3) and rearranging the result and taking

the integral from t_1 to t_2 of both sides of obtained equation gives:

$$\begin{aligned} \int_{t_1}^{t_2} (\tau_{ij}^v \dot{q}_{ij} - \frac{R_{ij}}{a_{ij}^2} (\tau_{ij}^v)^2) dt = \\ \int_{t_1}^{t_2} (-\frac{dK_{ij}}{dt} - \tau_{ij} \dot{q}_{ij} - L_{R_{ij}} - b_{ij} \bar{n}_{ij}^2 \dot{q}_{ij}^2) dt \end{aligned} \quad (C.5)$$

On the other hand, using ΔE_c from Eqn. (3.30), we can write:

$$\Delta E_s = \sum_{i=1}^N \sum_{j=1}^n \Delta E_{s_{ij}} \quad (C.6)$$

where:

$$\Delta E_{s_{ij}} = \int_{t_1}^{t_2} (\tau_{ij}^v \dot{q}_{ij} - \frac{R_{ij}}{a_{ij}^2} (\tau_{ij}^v)^2) dt \quad (C.7)$$

Using Eqns. (C.5) and (C.7), it can be concluded:

$$\Delta E_{s_{ij}} = \int_{t_1}^{t_2} (-\frac{dK_{ij}}{dt} - \tau_{ij} \dot{q}_{ij} - L_{R_{ij}} - b_{ij} \bar{n}_{ij}^2 \dot{q}_{ij}^2) dt \quad (C.8)$$

To derive Eqn. (3.31), we start by writing the overall energy balance for CRM:

$$\int_{t_1}^{t_2} \dot{q}^T \mathcal{T} dt + \int_{t_1}^{t_2} \dot{q}^T \mathcal{T}_{ext} dt = \Delta E_m^\circ + \Sigma_m^\circ \quad (C.9)$$

where the first term on the left-hand side is the work done by the semi-active joints, the second term is the work done by the external forces and moments (W_{ext}), ΔE_m° is the total change in mechanical energy, and Σ_m° is the dissipated mechanical energy in the system. Also \mathcal{T} is defined as the vector of all applied forces/moments and $\mathcal{T}_{ext} = J^T(q)F$ is the vector of external forces/moments, i.e. the forces/moments applied by the load.

If we write Eqn. (C.5) for all joints in CRM and substitute in Eqn. (C.9),

results:

$$W_{ext} = \Delta E_s + \Delta \tilde{E}_m + \tilde{\Sigma}_m + \Sigma_e \quad (\text{C.10})$$

where

$$\begin{aligned} \Delta \tilde{E}_m &= \Delta E_m^\circ + \sum_{i=1}^N \sum_{j=1}^n \Delta K_{ij} \\ \tilde{\Sigma}_m &= \Sigma_m^\circ + \sum_{i=1}^N \sum_{j=1}^n \int_{t_1}^{t_2} b_{ij} \bar{n}_{ij}^2 \dot{q}_{ij}^2 dt \\ \Sigma_e &= \sum_{i=1}^N \sum_{j=1}^n \int_{t_1}^{t_2} L_{R_{ij}} dt \end{aligned} \quad (\text{C.11})$$